



## A seismic reference model for the crust and uppermost mantle beneath China from surface wave dispersion

Journal:	<i>Geophysical Journal International</i>
Manuscript ID:	Draft
Manuscript Type:	Research Paper
Date Submitted by the Author:	n/a
Complete List of Authors:	Shen, Weisen; University of Colorado at Boulder, Department of Physics Ritzwoller, Michael; University of Colorado at Boulder, Department of Physics Kang, Dou; Peking University, Institute of Theoretical and Applied Geophysics, School of Earth and Space Sciences Kim, YoungHee; Seoul National University, School of Earth and Environmental Sciences Ning, Jie-yuan; Institute of Theoretical and Applied Geophysics, School of Earth and Space Science Lin, Fan-Chi; University of Utah, Wang, Weitao; Chinese Earthquake Administration, Institution of Geophysics Zheng, Yong; Institute of Geodesy and Geophysics, CAS, Zhou, Longquan; China Earthquake Network Center,
Keywords:	Surface waves and free oscillations < SEISMOLOGY, Seismic tomography < SEISMOLOGY, Crustal structure < TECTONOPHYSICS, Asia < GEOGRAPHIC LOCATION

# A seismic reference model for the crust and uppermost mantle beneath China from surface wave dispersion

Weisen Shen<sup>1</sup>, Michael H. Ritzwoller<sup>1</sup>, Dou Kang<sup>2</sup>, Younghee Kim<sup>3</sup>, Fan-Chi Lin<sup>4</sup>,  
Jieyuan Ning<sup>2</sup>, Weitao Wang<sup>5</sup>, Yong Zheng<sup>6</sup>, and Longquan Zhou<sup>7</sup>

1- Department of Physics, University of Colorado at Boulder, Boulder, CO 80309, USA  
weisen.shen@colorado.edu

2 - Institute of Theoretical and Applied Geophysics, School of Earth and Space Sciences, Peking  
University, Beijing, 100871 China

3 - School of Earth and Environmental Sciences, Seoul National University, Seoul, South Korea

4 - Department of Geology and Geophysics, University of Utah, Salt Lake City, UT 84112-0102

5 - Institute of Geophysics, Chinese Earthquake Administration, Beijing 100045 China

6- State Key Laboratory of Geodesy and Earth's Dynamics, Institute of Geodesy and Geophysics,  
Chinese Academy of Science, Wuhan 43077, China

7 - Chinese Earthquake Network Center, Chinese Earthquake Administration, Beijing 100045  
China

## Abstract:

Using data from more than 2000 seismic stations from multiple networks arrayed through  
China (CEArray, China Array, NECESS, PASSCAL, GSN) and surrounding regions  
(Korean Seismic Network, F-Net, KNET) we perform ambient noise Rayleigh wave  
tomography across the entire region and earthquake tomography across parts of South  
China and Northeast China. We produce isotropic Rayleigh wave group and phase speed  
maps with uncertainty estimates from 8 to 50 sec period across the entire region of study,  
extending them to 70 sec period where earthquake tomography is performed. Maps of  
azimuthal anisotropy are estimated simultaneously to minimize anisotropic bias in the  
isotropic maps, but are not discussed here. The 3D model is produced using a Bayesian  
Monte Carlo formalism covering all of China, extending eastward through the Korean  
Peninsula, into the marginal seas, to Japan. We define the final model as the mean and  
standard deviation of the posterior distribution at each location on a 0.5°x0.5° grid from  
the surface to 150 km depth. Surface wave dispersion data do not strongly constrain  
internal interfaces, but shear wave speeds between the discontinuities in the crystalline  
crust and uppermost mantle are well determined. We design the resulting model as a  
reference model, which is intended to be useful to other researchers as a starting model,  
to predict seismic wave fields and observables, and to predict other types of data (e.g.,  
topography, gravity). The model and the data on which it is based are available for  
download. In addition, the model displays a great variety and considerable richness of  
geological and tectonic features in the crust and in the uppermost mantle deserving of  
further focus and continued interpretation.

1  
2  
3  
4 **Keywords:** Surface waves and free oscillations; Seismic tomography; Crustal structure;  
5  
6  
7 Mantle structure; Asia

## 9 **1. Introduction**

10  
11  
12 The purpose of this study is to present a reference seismic model of the crust and  
13  
14 uppermost mantle to a depth of about 150 km beneath China and surrounding areas,  
15  
16 notably Tibet, and also the Korean Peninsula, the Sea of Japan, and the Yellow Sea. The  
17  
18 model is based predominantly on Rayleigh wave group and phase speed curves derived  
19  
20 from ambient noise at periods from 8 to 50 sec, but the data set is augmented with  
21  
22 Rayleigh wave phase speeds up to 70 sec period in South China and parts of Northeast  
23  
24 China. It is generated by a Bayesian Monte Carlo inversion so that model uncertainties  
25  
26 are determined in all variables. Ultimately, the model is designed to be used as a starting  
27  
28 point for regional scale studies and future inversions that assimilate different kinds of  
29  
30 data, as a basis for source location and characterization, and to predict other types of  
31  
32 geophysical data (body wave travel times, surface wave propagation characteristics,  
33  
34 gravity, temperatures, etc.).  
35  
36  
37  
38  
39  
40  
41  
42  
43

44  
45 This paper is a continuation and culmination of three earlier studies performed,  
46  
47 respectively, in Tibet (Yang et al., 2010, 2012), South China (Zhou et al., 2012), and  
48  
49 North and Northeast China (Zheng et al., 2011). The Rayleigh wave phase and group  
50  
51 velocity data sets developed in these studies derived principally from the China  
52  
53 Earthquake Array (CEArray) and PASSCAL installations in Tibet, but also included data  
54  
55  
56  
57  
58  
59  
60

1  
2  
3  
4 from F-Net stations in Japan. They were based primarily on ambient noise measurements  
5  
6 although Zhou et al. also developed an earthquake-derived data set for South China. The  
7  
8 regions of these studies overlapped somewhat near their boundaries and there was some  
9  
10 redundancy between the data sets. The data sets produced in these studies are assimilated  
11  
12 here. Because these data sets are confined to particular sub-regions of China, the  
13  
14 tomographic maps and models derived from them degrade near the boundary of each  
15  
16 region. Therefore, here we augment them by introducing new data from the NECESS  
17  
18 (Northeast China Extended Seismic Network) array, the Korean Seismic Network, the  
19  
20 China Array centered on Yunnan Province near the southeastern Tibetan Plateau and  
21  
22 south of the Sichuan Basin, and, importantly, new measurements between the three  
23  
24 regions based on CEArray stations, which effectively knits together these separate  
25  
26 regions. The stations used in this study are shown in [Figure 1](#) along with principal  
27  
28 geological/tectonic features identified in [Table 1](#). In total there are approximately 2073  
29  
30 stations used in this study. We measure Rayleigh wave group and phase speeds between  
31  
32 all pairs of simultaneously operating stations based on ambient noise and also perform  
33  
34 earthquake surface wave tomography beneath the NECESS array in Northeast China. The  
35  
36 disparate components of this extensive data set require unified systematic data quality  
37  
38 control (as discussed by Niu and Li, 2011) and error estimation procedures, which we  
39  
40 apply to all measurements including those from the earlier studies.  
41  
42  
43  
44  
45  
46  
47  
48  
49  
50  
51  
52  
53

54  
55 There is a long and rapidly growing list of studies of surface waves that have generated  
56  
57  
58  
59  
60

1  
2  
3  
4 dispersion maps and derived 3D models in various regions across China. Some are based  
5  
6 on ambient noise (e.g., Zheng et al., 2010b; Guo et al., 2009; Li et al., 2009; Huang et al.,  
7  
8 2010; Yang et al., 2010, 2012; Zheng et al., 2011; Guo et al., 2012; Luo et al., 2012;  
9  
10 Karplus, 2013; Sun et al., 2013; Xie et al., 2013), on earthquakes (e.g., Ritzwoller and  
11  
12 Levshin, 1998; Ritzwoller et al., 1998; Villasenor et al., 2001; Shapiro et al., 2004; Huang  
13  
14 et al., 2003, 2009; Acton et al., 2010; Jiang et al., 2011; Li et al., 2013a,b; Legendre et al.,  
15  
16 2014; Zhang et al., 2014), on both ambient noise and earthquakes (e.g., Yao et al., 2006,  
17  
18 2008, 2010; Zhou et al., 2012; Bao et al., 2013, 2015; Tang et al., 2013), and some from  
19  
20 joint inversions of surface waves and other types of data (e.g., Li et al., 2008; Obrebski et  
21  
22 al., 2012; Wang et al., 2014; Deng et al., 2014; Guo et al., 2015). What is unique about  
23  
24 the current study is that it is based on the largest set of surface wave information yet  
25  
26 compiled across China and surroundings, it produces isotropic and azimuthally  
27  
28 anisotropic dispersion maps with a uniform process of error estimation, and it generates a  
29  
30 3D isotropic model that includes uncertainties in all variables. We believe that these  
31  
32 characteristics and others qualify it as a reference model.  
33  
34  
35  
36  
37  
38  
39  
40  
41  
42  
43  
44

45 The structure of the paper is as follows. In section 2, we discuss the extensive data set on  
46  
47 which the model produced in this study is based. This includes its ambient noise and  
48  
49 earthquake components and uncertainty estimates at all periods and locations across the  
50  
51 study region. Sections 3 and 4 discuss the tomographic maps and the 3D model. Finally,  
52  
53 in section 5, we discuss the content of the 3D model.  
54  
55  
56  
57  
58  
59  
60

## 2. Data, Quality Control, Tomography Methods, and Uncertainties

### 2.1 Data processing

Ambient noise data processing is accomplished using the method described by Bensen et al. (2007) and Lin et al. (2008) with the primary caveat that pains are taken to minimize the impact of the Kyushu persistent microseismic source at Aso volcano in the center of Kyushi (e.g., Kawakatsu et al., 2011; Zeng and Ni, 2010, 2011), as described by Zheng et al. (2011). From the symmetric component of ambient noise vertical component cross-correlations, we measure Rayleigh wave group and phase speeds between 8 sec and 50 sec period across the entire region of study. As described further below, however, the long period measurements, in particular, degrade in some regions, but in a way that is captured by the uncertainty measurements, and reduce in number.

Although ambient noise data and constraints exist across the entire study region, we have only compiled earthquake data in South China from Zhou et al. (2012) and parts of Northeast China beneath the NECESS array as described further below and in greater detail by Kang et al. (2015). The measurements from the NECESS array are new to this study. Earthquake data are processed via eikonal tomography (Lin et al., 2009) in Northeast China or Helmholtz (Lin et al., 2011) tomography in South China, which differ based on whether a finite frequency correction is applied (e.g., Ritzwoller et al., 2011).

### 2.2 Core data set

The core of our data set is composed of cross-correlations of ambient noise between

1  
2  
3  
4 CEArray stations across China. Most of these cross-correlations were computed using  
5  
6 data from 2007 through 2009 and formed the basis for the papers of Zheng et al. (2011)  
7  
8 in North China and Northeast China and Yang et al. (2010, 2012) in Tibet. In addition,  
9  
10 there are cross-correlations of ambient noise using CEArray stations in South China  
11  
12 observed in 2009 through 2010 (Zhou et al., 2011). Cross-correlations between CEArray  
13  
14 stations in North/Northeast China were also computed with 69 F-Net stations in Japan.  
15  
16 Finally, Yang et al. (2010, 2012) also computed cross-correlations between CEArray and  
17  
18 PASSCAL installations in Tibet for data recorded between 2007 and 2009 and between  
19  
20 PASSCAL stations that were recorded earlier. A total of 481 PASSCAL stations were  
21  
22 used. We start the compilation of our data set with these measurements, which we refer to  
23  
24 here as the “Core” measurements. **Table 1** summarizes the number of unique paths in the  
25  
26 Core data set. The numbers of unique paths range from about 50,000 at the longest  
27  
28 periods up to about 160,000 paths near 20 sec period. At some periods the numbers are  
29  
30 lower (e.g., 22, 24, 26, 28, 32 sec) because Yang et al. did not compile measurements at  
31  
32 these periods.  
33  
34  
35  
36  
37  
38  
39  
40  
41  
42  
43  
44

### 45 **2.3 Augmented data set**

46  
47 We add to the Core measurements the “Augmented” measurements, which derive from  
48  
49 three sources. First, in preparing the studies of Yang et al. (2010, 2012) and Zheng et al.  
50  
51 (2011), cross-correlations of ambient noise were actually computed across the entire  
52  
53 CEArray (960 stations) using data from 2007 through 2009. These studies extracted and  
54  
55  
56  
57  
58  
59  
60

1  
2  
3  
4 used only the measurements within Tibet and North/Northeast China, respectively.  
5  
6  
7 Therefore, as the first part of the Augmented data set we have the many paths between  
8  
9 stations in separate regions (e.g., Tibet to North/Northeast China) and also paths that  
10  
11 include South China that were not part of the Core data set. In addition, we have added  
12  
13 measurements between stations in Tibet at periods not measured by Yang et al. The  
14  
15 number of new measurements from this source is identified in [Table 1](#) as “Augmented  
16  
17 CEArray”. Generally speaking there are about the same number of unique paths in the  
18  
19 Augmented CEArray data set as in the Core data set, but that ratio reduces appreciably  
20  
21 upon quality control because the Core data set already had quality control procedures  
22  
23 applied to them in the original studies. Second, we have added measurements using 120  
24  
25 stations from the NECESS array and 30 stations from the Korean Seismic Network  
26  
27 (KSN), computing cross-correlations of ambient noise both within each network and  
28  
29 between them using data from Sep 2009 and Aug 2011. The number of stations is reduced  
30  
31 relative to the entire station set from these two networks because we lack instrument  
32  
33 responses for seven NECESS stations and do not have access to 16 KSN stations. No  
34  
35 cross-correlations are made between the stations from these two networks with stations of  
36  
37 other networks (e.g., CEArray, China Array, F-Net, PASSCAL, etc.). Third, we have  
38  
39 combined 350 China Array stations in Yunan and Sichuan Provinces with 88 nearby  
40  
41 CEArray stations to form a 438 station array and compute cross-correlation exclusively  
42  
43 between these stations. We refer to these stations as “China Array”. In summary, the  
44  
45 Augmented data set increases the number of unique paths in the Core data set prior to  
46  
47  
48  
49  
50  
51  
52  
53  
54  
55  
56  
57  
58  
59  
60

1  
2  
3  
4 quality control by a multiplier of 2-3.  
5  
6

## 7 **2.4 Quality control of ambient noise data**

8  
9

10 One of the principal characteristics of the data set compiled in this study is that a single,  
11 uniform quality control procedure is applied to every dispersion measurement from  
12 ambient noise. This procedure consists of three key stages, which we call QC1, QC2, and  
13 QC3.  
14  
15  
16  
17  
18  
19

20  
21 QC1 consists of two parts. First, we identify redundant paths, i.e., measurements that  
22 exist between the same pairs of stations. This occurs in part because Zheng et al. (2011)  
23 and Zhou et al. (2012) make some measurements between the same pairs of stations but  
24 from different years. We resolve the ambiguity by choosing the measurement with the  
25 higher signal-to-noise ratio. The second part of QC1, which applies a procedure described  
26 by Zhou et al. (2011), is the identification of bad station information in which we  
27 measure the consistency between the Rayleigh wave phase travel-times observed between  
28 nearby stations using ambient noise. We use this information to identify station location  
29 errors, polarity reversals, and unknown factors that may be related to time varying  
30 instrument responses. Out of the 2073 stations in this study, about 5%, or more accurately  
31 107 stations, are identified as presenting erroneous information. Their locations and error  
32 types are presented in [Figure 2](#). Of these 107 stations, 57 stations are mis-located, 24  
33 have a polarity error, and 26 have unknown (perhaps time variable) phase errors.  
34  
35  
36  
37  
38  
39  
40  
41  
42  
43  
44  
45  
46  
47  
48  
49  
50  
51  
52  
53  
54  
55

56 Additionally, there are 11 stations for which we have  
57  
58  
59  
60

1  
2  
3  
4 ) from different data sources. In all cases, the stations are removed from our data set.  
5  
6

7 In principle, some of these errors could be corrected, but in this data rich study we choose  
8  
9 the more conservative option.  
10

11  
12 In QC2, we accept a group or phase speed measurement at a given period only if the  
13  
14 signal-to-noise ratio (SNR) of the symmetric component of the cross-correlation at that  
15  
16 period is greater than 15, where SNR is defined as in Bensen et al. (2007). This is a very  
17  
18 conservative acceptance criterion. In addition, we accept a measurement at a given period  
19  
20 only if the interstation spacing is greater than two wavelengths to ensure that the  
21  
22 measurement is in the far-field and that the observed wavepacket is sufficiently removed  
23  
24 from zero correlation lag to obtain a meaningful dispersion measurement.  
25  
26  
27  
28  
29

30  
31 Finally, in QC3, we require our measurements to cohere with one another. We do this  
32  
33 iteratively by constructing phase and group speed maps at each period, identifying and  
34  
35 rejecting 1%-2% of the outliers in each of three iterations. Examples of distributions of  
36  
37 misfits to measurements from the final estimated Rayleigh wave phase and group speed  
38  
39 maps are presented in [Figure 3](#), illustrating that outliers have been rejected. The standard  
40  
41 deviations of these distributions are listed in [Table 3](#). Phase travel time misfits are less  
42  
43 than 1 sec, on average, at periods below 28 sec and grow to about 1.5 sec near 50 sec  
44  
45 period. Part of this increase is due to the reduction of SNR as periods increase, which  
46  
47 increases random errors in phase speed measurements, but part is also due to the fact that  
48  
49 interstation distances grow with period.  
50  
51  
52  
53  
54  
55  
56  
57  
58  
59  
60

1  
2  
3  
4 Group travel time misfits are considerably larger than for phase travel times because  
5  
6 group times are a harder measurement to obtain reliably, as they depend on the amplitude  
7  
8 of the wave packet envelope rather than the phase of the surface wave arrival. Group and  
9  
10 phase travel time misfits grow with period at approximately the same rate, but the  
11  
12 standard deviation of group misfits is 2.5-3.5 times larger than phase misfits.  
13  
14  
15  
16

17  
18 **Table 2** shows how the number of measurements reduces at each stage of Quality Control.  
19

20  
21 The largest reduction occurs in QC2 due to the SNR criterion. The final data set that  
22  
23 emerges after the final Quality Control stage contains up to about 225,000 unique paths  
24  
25 with numbers reducing below 100,00 only at periods longer than 40 sec. At some periods  
26  
27 the final number of measurements is actually lower than the number in the Core data set  
28  
29 due to our more stringent quality control procedures. The more stringent standards, again,  
30  
31 are justified by the data rich setting of this study.  
32  
33  
34  
35  
36

## 37 **2.5 Earthquake data**

38  
39  
40 We assimilate data from Zhou et al. (2012) who computed Rayleigh wave phase speed  
41  
42 maps from 30 sec to 70 sec period across South China using earthquake-based eikonal  
43  
44 tomography (Lin et al, 2009.) In addition, we have also computed Rayleigh wave phase  
45  
46 speed maps from 30 sec to 70 sec period using data from the NECESS array, which are  
47  
48 described further by Kang et al. (2015). These new measurements are based on  
49  
50 Helmholtz tomography (Lin et al., 2011), which applies a finite frequency correction to  
51  
52 the eikonal tomography method. The differences between the two methods applied to  
53  
54  
55  
56  
57  
58  
59  
60

1  
2  
3  
4 data from the NECESS array are small. Because long period data ( $> 50$  sec period) only  
5  
6 exist in South China and parts of Northeast China, the long period Rayleigh wave phase  
7  
8 speed maps only exist in these two regions. In addition, we have no group speed  
9  
10 measurements based on earthquake data so group speed curves terminate at 50 sec period  
11  
12 everywhere across the region of study.  
13  
14  
15  
16

17  
18 The quality control procedure for earthquake data is described by Zhou et al. (2012) and  
19  
20 Kang et al. (2015). We discard a Rayleigh wave measurement at a given period and for a  
21  
22 given earthquake if its SNR is less than 8. Following Lin and Ritzwoller (2011), the  $2\pi$   
23  
24 phase ambiguity is resolved and phase measurements from particular earthquakes are  
25  
26 discarded following criteria based on the curvature of the phase travel time and amplitude  
27  
28 surfaces across the array.  
29  
30  
31  
32

## 33 34 **2.6 Tomographic methods**

35  
36 By “tomography” we mean the transformation of phase and group speed (or time)  
37  
38 measurements to phase or group speed maps at each period. The preferred tomographic  
39  
40 method for ambient noise data is eikonal tomography (Lin et al., 2009) because it yields  
41  
42 local uncertainty estimates both for isotropic and azimuthally anisotropic phase speeds.  
43  
44 Eikonal tomography is based on geometrical ray theory which models the sensitivity to  
45  
46 structure ray theoretically including the effect of lateral refraction of the wave paths.  
47  
48 However, eikonal tomography works only for phase speeds and requires regular station  
49  
50 spacing for optimal performance. Because we seek group velocity maps in addition to  
51  
52  
53  
54  
55  
56  
57  
58  
59  
60

1  
2  
3  
4 phase velocity maps and station spacing is irregular across much of the study region, we  
5  
6  
7 apply the traditional ray theoretic method of Barmin et al. (2001) to all ambient noise  
8  
9  
10 data in this study and results are presented on a  $0.5^\circ \times 0.5^\circ$  grid. This method produces  
11  
12 isotropic phase and group speed maps with resolution estimates as well as azimuthal  
13  
14 anisotropy maps, but does not estimate data uncertainties and models rays only along  
15  
16  
17 great-circle paths.  
18  
19

20  
21 Station spacing across parts of East China is sufficiently regular to apply eikonal  
22  
23 tomography to estimate phase speed maps, an example of which for the 20 sec Rayleigh  
24  
25 wave is presented in [Figure 4a](#). Previous studies have shown that finite frequency  
26  
27 corrections (produced, for example, by the Helmholtz tomography method) are not  
28  
29 required below 40-50 sec period for on-continent ambient noise derived measurements  
30  
31 (e.g., Lin et al., 2011) and they will not be applied here. The 20 sec Rayleigh wave phase  
32  
33 speed map using Barmin's traditional ray theoretic method is presented in [Figure 4b](#) for  
34  
35 comparison with [Figure 4a](#). The choice of damping and regularization in Barmin's  
36  
37 method are guided to optimize agreement between the maps. The maps are generally  
38  
39 quite similar, with differences scattered throughout the maps at small length scales ([Fig.](#)  
40  
41  
42  
43  
44  
45  
46  
47  
48  
49  
50  
51  
52  
53  
54  
55  
56  
57  
58  
59  
60  
61  
62  
63  
64  
65  
66  
67  
68  
69  
70  
71  
72  
73  
74  
75  
76  
77  
78  
79  
80  
81  
82  
83  
84  
85  
86  
87  
88  
89  
90  
91  
92  
93  
94  
95  
96  
97  
98  
99  
100  
101  
102  
103  
104  
105  
106  
107  
108  
109  
110  
111  
112  
113  
114  
115  
116  
117  
118  
119  
120  
121  
122  
123  
124  
125  
126  
127  
128  
129  
130  
131  
132  
133  
134  
135  
136  
137  
138  
139  
140  
141  
142  
143  
144  
145  
146  
147  
148  
149  
150  
151  
152  
153  
154  
155  
156  
157  
158  
159  
160  
161  
162  
163  
164  
165  
166  
167  
168  
169  
170  
171  
172  
173  
174  
175  
176  
177  
178  
179  
180  
181  
182  
183  
184  
185  
186  
187  
188  
189  
190  
191  
192  
193  
194  
195  
196  
197  
198  
199  
200  
201  
202  
203  
204  
205  
206  
207  
208  
209  
210  
211  
212  
213  
214  
215  
216  
217  
218  
219  
220  
221  
222  
223  
224  
225  
226  
227  
228  
229  
230  
231  
232  
233  
234  
235  
236  
237  
238  
239  
240  
241  
242  
243  
244  
245  
246  
247  
248  
249  
250  
251  
252  
253  
254  
255  
256  
257  
258  
259  
260  
261  
262  
263  
264  
265  
266  
267  
268  
269  
270  
271  
272  
273  
274  
275  
276  
277  
278  
279  
280  
281  
282  
283  
284  
285  
286  
287  
288  
289  
290  
291  
292  
293  
294  
295  
296  
297  
298  
299  
300  
301  
302  
303  
304  
305  
306  
307  
308  
309  
310  
311  
312  
313  
314  
315  
316  
317  
318  
319  
320  
321  
322  
323  
324  
325  
326  
327  
328  
329  
330  
331  
332  
333  
334  
335  
336  
337  
338  
339  
340  
341  
342  
343  
344  
345  
346  
347  
348  
349  
350  
351  
352  
353  
354  
355  
356  
357  
358  
359  
360  
361  
362  
363  
364  
365  
366  
367  
368  
369  
370  
371  
372  
373  
374  
375  
376  
377  
378  
379  
380  
381  
382  
383  
384  
385  
386  
387  
388  
389  
390  
391  
392  
393  
394  
395  
396  
397  
398  
399  
400  
401  
402  
403  
404  
405  
406  
407  
408  
409  
410  
411  
412  
413  
414  
415  
416  
417  
418  
419  
420  
421  
422  
423  
424  
425  
426  
427  
428  
429  
430  
431  
432  
433  
434  
435  
436  
437  
438  
439  
440  
441  
442  
443  
444  
445  
446  
447  
448  
449  
450  
451  
452  
453  
454  
455  
456  
457  
458  
459  
460  
461  
462  
463  
464  
465  
466  
467  
468  
469  
470  
471  
472  
473  
474  
475  
476  
477  
478  
479  
480  
481  
482  
483  
484  
485  
486  
487  
488  
489  
490  
491  
492  
493  
494  
495  
496  
497  
498  
499  
500  
501  
502  
503  
504  
505  
506  
507  
508  
509  
510  
511  
512  
513  
514  
515  
516  
517  
518  
519  
520  
521  
522  
523  
524  
525  
526  
527  
528  
529  
530  
531  
532  
533  
534  
535  
536  
537  
538  
539  
540  
541  
542  
543  
544  
545  
546  
547  
548  
549  
550  
551  
552  
553  
554  
555  
556  
557  
558  
559  
560  
561  
562  
563  
564  
565  
566  
567  
568  
569  
570  
571  
572  
573  
574  
575  
576  
577  
578  
579  
580  
581  
582  
583  
584  
585  
586  
587  
588  
589  
590  
591  
592  
593  
594  
595  
596  
597  
598  
599  
600  
601  
602  
603  
604  
605  
606  
607  
608  
609  
610  
611  
612  
613  
614  
615  
616  
617  
618  
619  
620  
621  
622  
623  
624  
625  
626  
627  
628  
629  
630  
631  
632  
633  
634  
635  
636  
637  
638  
639  
640  
641  
642  
643  
644  
645  
646  
647  
648  
649  
650  
651  
652  
653  
654  
655  
656  
657  
658  
659  
660  
661  
662  
663  
664  
665  
666  
667  
668  
669  
670  
671  
672  
673  
674  
675  
676  
677  
678  
679  
680  
681  
682  
683  
684  
685  
686  
687  
688  
689  
690  
691  
692  
693  
694  
695  
696  
697  
698  
699  
700  
701  
702  
703  
704  
705  
706  
707  
708  
709  
710  
711  
712  
713  
714  
715  
716  
717  
718  
719  
720  
721  
722  
723  
724  
725  
726  
727  
728  
729  
730  
731  
732  
733  
734  
735  
736  
737  
738  
739  
740  
741  
742  
743  
744  
745  
746  
747  
748  
749  
750  
751  
752  
753  
754  
755  
756  
757  
758  
759  
760  
761  
762  
763  
764  
765  
766  
767  
768  
769  
770  
771  
772  
773  
774  
775  
776  
777  
778  
779  
780  
781  
782  
783  
784  
785  
786  
787  
788  
789  
790  
791  
792  
793  
794  
795  
796  
797  
798  
799  
800  
801  
802  
803  
804  
805  
806  
807  
808  
809  
810  
811  
812  
813  
814  
815  
816  
817  
818  
819  
820  
821  
822  
823  
824  
825  
826  
827  
828  
829  
830  
831  
832  
833  
834  
835  
836  
837  
838  
839  
840  
841  
842  
843  
844  
845  
846  
847  
848  
849  
850  
851  
852  
853  
854  
855  
856  
857  
858  
859  
860  
861  
862  
863  
864  
865  
866  
867  
868  
869  
870  
871  
872  
873  
874  
875  
876  
877  
878  
879  
880  
881  
882  
883  
884  
885  
886  
887  
888  
889  
890  
891  
892  
893  
894  
895  
896  
897  
898  
899  
900  
901  
902  
903  
904  
905  
906  
907  
908  
909  
910  
911  
912  
913  
914  
915  
916  
917  
918  
919  
920  
921  
922  
923  
924  
925  
926  
927  
928  
929  
930  
931  
932  
933  
934  
935  
936  
937  
938  
939  
940  
941  
942  
943  
944  
945  
946  
947  
948  
949  
950  
951  
952  
953  
954  
955  
956  
957  
958  
959  
960  
961  
962  
963  
964  
965  
966  
967  
968  
969  
970  
971  
972  
973  
974  
975  
976  
977  
978  
979  
980  
981  
982  
983  
984  
985  
986  
987  
988  
989  
990  
991  
992  
993  
994  
995  
996  
997  
998  
999  
1000

of the difference is 17.5 m/s or 0.5%, as the histogram in [Figure 4d](#) illustrates. As  
reported in section 2.8, these differences to lie within data uncertainties, when the  
uncertainties are properly defined. The difference of the mean may be due to the effect of

1  
2  
3  
4 off great-circle propagation, but it is below what we consider to be a significant bias. On  
5  
6  
7 this basis, we apply the traditional ray theoretic method of Barmin to produce all ambient  
8  
9  
10 noise maps presented here but take pains to estimate uncertainties in the maps, as  
11  
12 discussed in section 2.8. Tomographic maps for both isotropic and azimuthally  
13  
14 anisotropic wave speeds are presented in section 3.

15  
16  
17  
18 A similar comparison of estimates of azimuthal anisotropy for Rayleigh wave phase  
19  
20 speed at 20 sec period between eikonal tomography and Barmin's method is presented in  
21  
22 **Figure 5** in a region where eikonal tomography performs well. The average of the  
23  
24 absolute value of the difference in the observed fast axis directions of azimuthal  
25  
26 anisotropy between the two methods is  $11.8^\circ$  and the average of the difference in the  
27  
28 amplitudes between the methods is about 0.3%. Lin et al. (2011) present results from  
29  
30 random simulations of noisy realizations of azimuthal anisotropy and argue that  
31  
32 differences at this level are expected given the size of uncertainties in estimates of the  
33  
34 amplitude and fast axis direction of azimuthal anisotropy. Therefore, we conclude that the  
35  
36 traditional tomographic method of Barmin et al. presents sufficiently accurate and precise  
37  
38 results to act as the basis for the model presented here.

39  
40  
41  
42 Using Helmholtz tomography we produce new Rayleigh wave phase speed maps from 30  
43  
44 sec to 70 sec period based on earthquake data beneath the NECESS array in Northeast  
45  
46  
47 China, also on a  $0.5^\circ \times 0.5^\circ$  grid. We also assimilate the previous earthquake-derived phase  
48  
49  
50 speed maps produced by Zhou et al. (2012) in South China based on eikonal tomography  
51  
52  
53  
54  
55  
56  
57  
58  
59  
60

1  
2  
3  
4 from 30 sec to 70 sec period. Therefore, spatial coverage at periods greater than 50 sec is  
5  
6 patchy across East China, as the tomographic maps presented in section 3 illustrate. An  
7  
8 example of an earthquake-derived Rayleigh wave phase speed map at 40 sec period is  
9  
10 shown in [Figure 6a](#) and compared with the ambient noise derived map in [Figure 6b](#). The  
11  
12 earthquake-derived map only exists beneath the NECESS array whose outline is drawn in  
13  
14 [Figures 6a and 6b](#). Differences between the maps are shown in map and histogram forms  
15  
16 in [Figures 6c and 6d](#), respectively. As discussed in section 2.8, these differences are  
17  
18 within differences expected given data uncertainties, which we interpret to indicate  
19  
20 agreement between the earthquake and ambient noise based tomography methods.  
21  
22  
23  
24  
25  
26  
27

## 28 **2.7 Resulting local dispersion curves**

29  
30  
31 Examples of final group and phase speed maps for both isotropic and azimuthally  
32  
33 anisotropic Rayleigh waves are presented in section 3. The data used in the inversion for  
34  
35 the 3D model are local Rayleigh wave phase and group speed curves with uncertainties;  
36  
37 examples from three locations across China are presented in [Figure 7](#), which illustrate the  
38  
39 variability of the curves. The dispersion curves across Tibet (e.g., [Fig. 7a](#)) are  
40  
41 distinguished by the effect of the anomalously thick crust there so that the Airy phase  
42  
43 (group velocity minimum) appears at much longer periods than elsewhere across the  
44  
45 study region. The Northeast China curves in [Figure 7c](#) come from the Songliao  
46  
47 sedimentary basin, which reduces phase and group speeds at short periods at this location.  
48  
49 The structure beneath South China is simpler, which is reflected in simple dispersion  
50  
51  
52  
53  
54  
55  
56  
57  
58  
59  
60

1  
2  
3  
4 curves (e.g., Fig. 7b). The estimation of the uncertainties is discussed in section 2.8.  
5  
6

7 At 30 sec period and below local Rayleigh wave speeds and uncertainties derive entirely  
8 from ambient noise data everywhere and at 50 sec and above they derive entirely from  
9 earthquake data where such information exists. For intervening periods ( $30 < \tau < 50$ ),  
10 wave speeds and uncertainties are averaged from both data sets. Across most of the  
11 region of study, earthquake results do not exist, but where they do exist we compute a  
12 weighted average of both velocity estimates and uncertainties where the weights applied  
13 to ambient noise and earthquake derived values change linearly with period. For example,  
14 at 30 sec period the ambient noise weight is 1 and the earthquake weight is 0, at 40 sec  
15 period both the ambient noise and earthquake weights are 0.5, and at 50 sec period the  
16 ambient noise weight is 0 and the earthquake weight is 1. The fact that ambient noise and  
17 earthquake contributions to the resulting dispersion curves vary spatially and with period  
18 is an unfortunate complication in this study, but reflects the large spatial extent of this  
19 study, the long time frame of the observations, and the highly variable nature of the  
20 instrumentation and the data sources.  
21  
22  
23  
24  
25  
26  
27  
28  
29  
30  
31  
32  
33  
34  
35  
36  
37  
38  
39  
40  
41  
42  
43  
44

## 45 **2.8 Uncertainty estimates**

46  
47

48 For earthquake data, we use uncertainties estimated from the eikonal and Helmholtz  
49 tomography methods directly in Northeast China and South China, respectively. For  
50 ambient noise, the situation is unfortunately more complicated; we do not have  
51 uncertainty estimates everywhere because eikonal tomography only performs well across  
52  
53  
54  
55  
56  
57  
58  
59  
60

1  
2  
3  
4 a subset of the study region. Therefore, we start with the uncertainties estimated from  
5  
6 eikonal tomography wherever it can be applied and, following Lin et al. (2009), scale up  
7  
8 the raw uncertainties by a factor of 2 to account for the fact that individual measurements  
9  
10 of phase travel times at particular locations are not independent. Because eikonal  
11  
12 tomography cannot be applied everywhere across the study region, we extrapolate the  
13  
14 uncertainty estimates where we have them to locations where we do not. To do this, we  
15  
16 are guided by local estimates of resolution,  $R(\mathbf{r})$ , which we do have everywhere using  
17  
18 Barmin's method.  
19

20  
21 We find that uncertainties estimated with eikonal tomography are approximately constant  
22  
23 as a function of location wherever data coverage is high. In an unpublished result based  
24  
25 on USArray data we find that uncertainties scale approximately with local path density or  
26  
27 resolution. Therefore, where eikonal tomography cannot be applied we scale up the  
28  
29 uncertainties based on local data coverage. **Figure 8a** shows that path density across the  
30  
31 study area is quite variable, with the best coverage occurring where we are able to apply  
32  
33 eikonal tomography. Eikonal tomography does not provide an estimate of resolution, but  
34  
35 the method of Barmin et al. (2001) generates a resolution map for each target location to  
36  
37 which a 2D Gaussian is fit. Twice the standard deviation of the fit Gaussian is interpreted  
38  
39 as the local resolution,  $R(\mathbf{r})$ , at position  $\mathbf{r}$ . Local resolution defined in this way is a  
40  
41 complicated function of path density, local station spacing, and the chosen grid spacing.  
42  
43  
44  
45  
46  
47  
48  
49  
50  
51  
52  
53  
54  
55  
56  
57  
58  
59  
60 In the data rich regions of our study, local resolution is approximately the grid spacing,

1  
2  
3  
4 which averages  $\sim 50$  km. An example at 20 sec period is shown in [Figure 8b](#), where the  
5  
6  
7 best resolution is about 50 km, which is found across much of East China. We refer to  
8  
9  
10 this best resolution across a tomographic map as the optimal resolution at a given period,  
11  
12  $R_{\text{optimal}}$ .

13  
14  
15 To estimate local uncertainties we take the following two step procedure. (1) In regions  
16  
17 of nearly optimal resolution where local resolution  $R(\mathbf{r})$  is within about 10% of  $R_{\text{optimal}}$  at  
18  
19 each period, we average the uncertainties from eikonal tomography across the region and  
20  
21 assign the same value everywhere at that period. This procedure yields a set of period ( $\tau$ )  
22  
23 dependent uncertainties  $\sigma_{\text{optimal}}(\tau)$  for all points in the region of nearly optimal resolution.  
24  
25  
26 (2) Outside the region of nearly optimal resolution, eikonal tomography typically does  
27  
28 not perform well. We find that we capture reasonable uncertainties if we increase  $\sigma_{\text{optimal}}$   
29  
30 via local resolution at a given period in the following way:  
31  
32  
33  
34  
35

$$36 \quad \sigma(\mathbf{r}) = \sigma_{\text{optimal}} \sqrt{R(\mathbf{r}) / R_{\text{optimal}}} \quad (1)$$

37  
38 where  $\sigma(\mathbf{r})$  is the position dependent uncertainty that we seek. This procedure is followed  
39  
40 for phase speeds at each period separately.  
41  
42  
43  
44

45  
46 Example maps of phase speed uncertainties computed in this way are shown at periods of  
47  
48 10 sec and 30 sec in [Figure 9a,b](#), where at these periods the uncertainties are based on  
49  
50 ambient noise data alone. Note that uncertainties are constant across large regions of  
51  
52 these maps, which are near optimal resolution, and then increase toward the periphery of  
53  
54 the maps. At 40 sec period ([Fig. 9c](#)) the uncertainties are based on ambient noise results  
55  
56  
57  
58  
59  
60

1  
2  
3  
4 where earthquake derived results do not exist, but are the average of uncertainties from  
5  
6 ambient noise and earthquakes data where both types of measurements exist.  
7

8  
9 Uncertainties are approximately the same using earthquake data or ambient noise data  
10  
11 and, at least in South China and Northeast China where the earthquake data exist. In the  
12  
13 peripheral parts of the maps uncertainties from ambient noise data increase strongly. Note  
14  
15 that in this intermediate period range between 30 sec and 50 sec period, where we have  
16  
17 uncertainty estimates from both types of data, we apply the same linear weighting scheme  
18  
19 to compute a weighted average uncertainty that we apply to the phase speeds, described  
20  
21 in section 2.6. At 60 sec period uncertainties are from earthquake data alone. The  
22  
23 uncertainty map in [Figure 9d](#), therefore, demarcates the locations of earthquake results.  
24  
25 The area of higher uncertainty (dark blues) in the middle of South China results from a  
26  
27 station gap at that location, as can be seen in [Figure 1a](#).  
28  
29  
30  
31  
32  
33  
34  
35

36  
37 Uncertainties estimated for group speed maps from ambient noise are scaled from the  
38  
39 local uncertainties  $\sigma(\mathbf{r})$  in phase speed. The scaling factor is 2.5 because misfits to group  
40  
41 velocities tend to be 2.5 – 3.5 times larger than for phase velocities across most regions  
42  
43 we have studied ([Fig. 3](#) here, and similar results in earlier studies; e.g., Moschetti et al.,  
44  
45 2010). The procedure is a little more subtle than this because phase and group resolutions  
46  
47 differ somewhat and we use the group resolution to guide this process. Examples are  
48  
49 shown in [Figure 10a,b](#).  
50  
51  
52  
53  
54

55  
56 Uncertainties averaged across the study region are summarized in [Fig. 10c](#). Group speed  
57  
58  
59  
60

1  
2  
3  
4 uncertainties are for ambient noise results alone and minimize near 20 sec period, but  
5  
6 increase sharply at periods above about 30 sec. Phase speed uncertainties also minimize  
7  
8 around 20 sec period and increase with period, but not as strongly as for group speeds.  
9  
10 Phase speed uncertainties based on earthquake data are flatter still with period and, on  
11  
12 average, somewhat lower than uncertainties based on ambient noise data in the period  
13  
14 band of overlap. However, this is because ambient noise results extend into regions with  
15  
16 poor data coverage where uncertainties are higher and the average uncertainty reflects  
17  
18 these regions. Uncertainties based on ambient noise in regions where there are earthquake  
19  
20 data are similar to earthquake based uncertainties.  
21  
22  
23  
24  
25  
26  
27

28  
29 The Rayleigh wave phase speed uncertainties presented in [Figure 9](#) capture differences in  
30  
31 the phase speed maps that result from the application of different tomographic methods to  
32  
33 ambient noise data or from different data sets (ambient noise versus earthquake data). For  
34  
35 example, at 20 sec period the average Rayleigh wave phase speed uncertainty is ~12 m/s  
36  
37 ([Fig. 10c](#)) and the standard deviation of the difference between the maps derived from  
38  
39 eikonal and traditional tomography is 17.5 m/s, as seen in [Figure 4d](#). Assuming that the  
40  
41 maps from eikonal and traditional ambient noise tomography have independent Gaussian  
42  
43 error processes with a standard deviation of 12 m/s, the standard deviation of their  
44  
45 difference is expected to be about  $\sqrt{2} \times 12 \text{ m/s} \sim 17 \text{ m/s}$ . Thus, with a standard deviation of  
46  
47 their difference of 17.5 m/s, the 20 sec period maps differ approximately as expected  
48  
49 given the estimated uncertainties. Similarly, at 40 sec period beneath the NECESS array  
50  
51  
52  
53  
54  
55  
56  
57  
58  
59  
60

1  
2  
3  
4 the average Rayleigh wave phase speed uncertainty is  $\sim 22$  m/s (Fig. 9c) for both ambient  
5  
6 noise and earthquake derived results; thus the maps are expected to differ with a standard  
7  
8 deviation of about  $\sqrt{2}$  larger than this value, or about 31 m/s. The standard deviation of  
9  
10 the difference between the maps derived using ambient noise and earthquake data is 27  
11  
12 m/s, as seen in Figure 6d, which is slightly better agreement than expected given our  
13  
14 uncertainty estimates. This may mean that uncertainties at this period in this region are  
15  
16 slightly over estimated.  
17  
18  
19  
20  
21

22  
23 One standard deviation uncertainty estimates are presented as error bars in the Rayleigh  
24  
25 wave phase and group speed curves presented for three locations in Figure 7. Error bars  
26  
27 for group speeds are seen to be larger than for phase speeds and they are larger at longer  
28  
29 periods. We show later in section 4 that on average the data are fit at about the  $0.9\sigma$  level,  
30  
31 which we will argue provides evidence that the error bars realistically capture uncertainty  
32  
33 in the measurements.  
34  
35  
36  
37  
38

### 39 **3. Tomographic Maps**

40  
41  
42 As discussed and justified in section 2, we construct Rayleigh wave phase and group  
43  
44 speed maps using the straight ray theoretic method of Barmin et al. (2001). The maps are  
45  
46 constructed iteratively while discarding outliers. Examples of the fit to the observations  
47  
48 by the tomographic maps are presented in Figure 3. The damping and regularization  
49  
50 imposed in the tomographic inversions are guided by comparisons such as those in Figure  
51  
52  
53  
54  
55  
56  
57  
58  
59  
60  
4 with maps constructed using eikonal tomography, a method that is free from damping

1  
2  
3  
4 and also models off-great circle propagation. We find that with the right choice of  
5  
6  
7 damping and smoothing the maps derived using the traditional tomographic method of  
8  
9  
10 Barmin et al. (2001) match results from eikonal tomography where they exist with high  
11  
12 fidelity and within estimated uncertainties.

13  
14  
15 Examples of Rayleigh wave phase speed maps at a variety of periods are presented in  
16  
17 **Figure 11**. Ambient noise derived results exist everywhere across the maps at periods of  
18  
19 50 sec and below and earthquake based results exist between 30 sec and 70 sec period  
20  
21 only in parts of South and Northeast China. Therefore, the maps shown in **Figure 11** at 30  
22  
23 sec and below derive exclusively from ambient noise data, the map at 40 sec derives from  
24  
25 both ambient noise and earthquake data weighted equally where both types of data exist  
26  
27 and from ambient noise elsewhere, the map at 50 sec derives from earthquake data where  
28  
29 it exists and ambient noise elsewhere, and the map at 70 sec period derives from  
30  
31 earthquake data alone. Maps are presented at each period wherever local resolution is  
32  
33 estimated to be better than 160 km, where resolution is defined as twice the standard  
34  
35 deviation of the 2D Gaussian fit to the resolution surface for each target point (Barmin et  
36  
37 al., 2001).  
38  
39  
40  
41  
42  
43  
44  
45  
46  
47

48 At 10 sec period (**Fig. 11a**), Rayleigh wave phase speed is highly sensitive to the  
49  
50 existence and character (thickness, lithology) of sedimentary basins with the Junggar,  
51  
52 Tarmin, Sichuan, Jiangnan, North China (Bohaiwan, Taikang Hefei), and Songliao basins  
53  
54 appearing prominently onshore along with basins offshore (East China Sea, Subei Yellow  
55  
56  
57  
58  
59  
60

1  
2  
3  
4 Sea, Tsushima). Phase speeds from 20 to 40 sec period (Fig. 11b-d) reflect crustal shear  
5  
6 wave speeds and notably crustal thickness, where lower phase speeds indicate thicker  
7  
8 crust. At 50 sec and higher (Fig. 11e,f), the maps are mostly sensitive to upper mantle  
9  
10 shear wave speeds. At periods of 20 sec and higher, phase speed maps are dominated by  
11  
12 an East-West dichotomy across the study region, which reflects the much thicker crust  
13  
14 beneath Tibet. Smaller scale anomalies with smaller amplitudes are apparent within the  
15  
16 eastern and western parts of the study region, characteristic of variations between and  
17  
18 within tectonic units. For example, at 50 sec period the highest Rayleigh wave speeds  
19  
20 appear in the western Yangtze craton beneath the Sichuan basin, presumably representing  
21  
22 the core of the craton. A similar high velocity anomaly exists at 50 sec period beneath the  
23  
24 Ordos block. The 70 sec period phase speed map is derived exclusively from earthquake  
25  
26 data and is confined to parts of South and Northeast China.  
27  
28  
29  
30  
31  
32  
33  
34  
35

36 The Rayleigh wave group speed maps presented in Figure 12 derive exclusively from  
37  
38 ambient noise data. They are similar to the phase speed maps except group speed at a  
39  
40 given period is sensitive to shallower structure than phase speed at the same period. Thus,  
41  
42 the 20 sec group speed map presented in Figure 12b retains significant sensitivity to  
43  
44 sedimentary structure unlike the 20 sec phase speed map and is less dominated by the  
45  
46 East-West dichotomy. The 10 sec group speed map (Fig. 12a) displays sedimentary basins  
47  
48 even more clearly than the 10 sec phase speed map (Fig. 11a). The shallower sensitivity  
49  
50 of group speed measurements makes them particularly useful to constrain sedimentary  
51  
52  
53  
54  
55  
56  
57  
58  
59  
60

1  
2  
3  
4 structure. The East-West dichotomy across the study region asserts itself strongly on  
5  
6  
7 group speed maps at periods above 30 sec (e.g., Fig. 12c,d).  
8

9  
10 A significant technical aspect in the construction of the isotropic group and phase speed  
11  
12 maps is the simultaneous estimation of azimuthal anisotropy. In some areas where  
13  
14 azimuthal coverage is not optimal, particularly in parts of Tibet, whether azimuthal  
15  
16 anisotropy is estimated simultaneously with the isotropic maps strongly affects the  
17  
18 characteristics of the isotropic maps. Here, where our focus is the development of an  
19  
20 isotropic reference model, we estimate azimuthal anisotropy to ensure that the isotropic  
21  
22 maps and resulting model are not biased by anisotropy. However, the maps of azimuthal  
23  
24 anisotropy are interesting intrinsically and are produced for potential later use. Figure  
25  
26  
27  
28  
29  
30  
31  
32  
33  
34  
35  
36  
37  
38  
39  
40  
41  
42  
43  
44  
45  
46  
47  
48  
49  
50  
51  
52  
53  
54  
55  
56  
57  
58  
59  
60  
61  
62  
63  
64  
65  
66  
67  
68  
69  
70  
71  
72  
73  
74  
75  
76  
77  
78  
79  
80  
81  
82  
83  
84  
85  
86  
87  
88  
89  
90  
91  
92  
93  
94  
95  
96  
97  
98  
99  
100  
101  
102  
103  
104  
105  
106  
107  
108  
109  
110  
111  
112  
113  
114  
115  
116  
117  
118  
119  
120  
121  
122  
123  
124  
125  
126  
127  
128  
129  
130  
131  
132  
133  
134  
135  
136  
137  
138  
139  
140  
141  
142  
143  
144  
145  
146  
147  
148  
149  
150  
151  
152  
153  
154  
155  
156  
157  
158  
159  
160  
161  
162  
163  
164  
165  
166  
167  
168  
169  
170  
171  
172  
173  
174  
175  
176  
177  
178  
179  
180  
181  
182  
183  
184  
185  
186  
187  
188  
189  
190  
191  
192  
193  
194  
195  
196  
197  
198  
199  
200  
201  
202  
203  
204  
205  
206  
207  
208  
209  
210  
211  
212  
213  
214  
215  
216  
217  
218  
219  
220  
221  
222  
223  
224  
225  
226  
227  
228  
229  
230  
231  
232  
233  
234  
235  
236  
237  
238  
239  
240  
241  
242  
243  
244  
245  
246  
247  
248  
249  
250  
251  
252  
253  
254  
255  
256  
257  
258  
259  
260  
261  
262  
263  
264  
265  
266  
267  
268  
269  
270  
271  
272  
273  
274  
275  
276  
277  
278  
279  
280  
281  
282  
283  
284  
285  
286  
287  
288  
289  
290  
291  
292  
293  
294  
295  
296  
297  
298  
299  
300  
301  
302  
303  
304  
305  
306  
307  
308  
309  
310  
311  
312  
313  
314  
315  
316  
317  
318  
319  
320  
321  
322  
323  
324  
325  
326  
327  
328  
329  
330  
331  
332  
333  
334  
335  
336  
337  
338  
339  
340  
341  
342  
343  
344  
345  
346  
347  
348  
349  
350  
351  
352  
353  
354  
355  
356  
357  
358  
359  
360  
361  
362  
363  
364  
365  
366  
367  
368  
369  
370  
371  
372  
373  
374  
375  
376  
377  
378  
379  
380  
381  
382  
383  
384  
385  
386  
387  
388  
389  
390  
391  
392  
393  
394  
395  
396  
397  
398  
399  
400  
401  
402  
403  
404  
405  
406  
407  
408  
409  
410  
411  
412  
413  
414  
415  
416  
417  
418  
419  
420  
421  
422  
423  
424  
425  
426  
427  
428  
429  
430  
431  
432  
433  
434  
435  
436  
437  
438  
439  
440  
441  
442  
443  
444  
445  
446  
447  
448  
449  
450  
451  
452  
453  
454  
455  
456  
457  
458  
459  
460  
461  
462  
463  
464  
465  
466  
467  
468  
469  
470  
471  
472  
473  
474  
475  
476  
477  
478  
479  
480  
481  
482  
483  
484  
485  
486  
487  
488  
489  
490  
491  
492  
493  
494  
495  
496  
497  
498  
499  
500  
501  
502  
503  
504  
505  
506  
507  
508  
509  
510  
511  
512  
513  
514  
515  
516  
517  
518  
519  
520  
521  
522  
523  
524  
525  
526  
527  
528  
529  
530  
531  
532  
533  
534  
535  
536  
537  
538  
539  
540  
541  
542  
543  
544  
545  
546  
547  
548  
549  
550  
551  
552  
553  
554  
555  
556  
557  
558  
559  
560  
561  
562  
563  
564  
565  
566  
567  
568  
569  
570  
571  
572  
573  
574  
575  
576  
577  
578  
579  
580  
581  
582  
583  
584  
585  
586  
587  
588  
589  
590  
591  
592  
593  
594  
595  
596  
597  
598  
599  
600  
601  
602  
603  
604  
605  
606  
607  
608  
609  
610  
611  
612  
613  
614  
615  
616  
617  
618  
619  
620  
621  
622  
623  
624  
625  
626  
627  
628  
629  
630  
631  
632  
633  
634  
635  
636  
637  
638  
639  
640  
641  
642  
643  
644  
645  
646  
647  
648  
649  
650  
651  
652  
653  
654  
655  
656  
657  
658  
659  
660  
661  
662  
663  
664  
665  
666  
667  
668  
669  
670  
671  
672  
673  
674  
675  
676  
677  
678  
679  
680  
681  
682  
683  
684  
685  
686  
687  
688  
689  
690  
691  
692  
693  
694  
695  
696  
697  
698  
699  
700  
701  
702  
703  
704  
705  
706  
707  
708  
709  
710  
711  
712  
713  
714  
715  
716  
717  
718  
719  
720  
721  
722  
723  
724  
725  
726  
727  
728  
729  
730  
731  
732  
733  
734  
735  
736  
737  
738  
739  
740  
741  
742  
743  
744  
745  
746  
747  
748  
749  
750  
751  
752  
753  
754  
755  
756  
757  
758  
759  
760  
761  
762  
763  
764  
765  
766  
767  
768  
769  
770  
771  
772  
773  
774  
775  
776  
777  
778  
779  
780  
781  
782  
783  
784  
785  
786  
787  
788  
789  
790  
791  
792  
793  
794  
795  
796  
797  
798  
799  
800  
801  
802  
803  
804  
805  
806  
807  
808  
809  
810  
811  
812  
813  
814  
815  
816  
817  
818  
819  
820  
821  
822  
823  
824  
825  
826  
827  
828  
829  
830  
831  
832  
833  
834  
835  
836  
837  
838  
839  
840  
841  
842  
843  
844  
845  
846  
847  
848  
849  
850  
851  
852  
853  
854  
855  
856  
857  
858  
859  
860  
861  
862  
863  
864  
865  
866  
867  
868  
869  
870  
871  
872  
873  
874  
875  
876  
877  
878  
879  
880  
881  
882  
883  
884  
885  
886  
887  
888  
889  
890  
891  
892  
893  
894  
895  
896  
897  
898  
899  
900  
901  
902  
903  
904  
905  
906  
907  
908  
909  
910  
911  
912  
913  
914  
915  
916  
917  
918  
919  
920  
921  
922  
923  
924  
925  
926  
927  
928  
929  
930  
931  
932  
933  
934  
935  
936  
937  
938  
939  
940  
941  
942  
943  
944  
945  
946  
947  
948  
949  
950  
951  
952  
953  
954  
955  
956  
957  
958  
959  
960  
961  
962  
963  
964  
965  
966  
967  
968  
969  
970  
971  
972  
973  
974  
975  
976  
977  
978  
979  
980  
981  
982  
983  
984  
985  
986  
987  
988  
989  
990  
991  
992  
993  
994  
995  
996  
997  
998  
999  
1000

142  
143  
144  
145  
146  
147  
148  
149  
150  
151  
152  
153  
154  
155  
156  
157  
158  
159  
160  
161  
162  
163  
164  
165  
166  
167  
168  
169  
170  
171  
172  
173  
174  
175  
176  
177  
178  
179  
180  
181  
182  
183  
184  
185  
186  
187  
188  
189  
190  
191  
192  
193  
194  
195  
196  
197  
198  
199  
200  
201  
202  
203  
204  
205  
206  
207  
208  
209  
210  
211  
212  
213  
214  
215  
216  
217  
218  
219  
220  
221  
222  
223  
224  
225  
226  
227  
228  
229  
230  
231  
232  
233  
234  
235  
236  
237  
238  
239  
240  
241  
242  
243  
244  
245  
246  
247  
248  
249  
250  
251  
252  
253  
254  
255  
256  
257  
258  
259  
260  
261  
262  
263  
264  
265  
266  
267  
268  
269  
270  
271  
272  
273  
274  
275  
276  
277  
278  
279  
280  
281  
282  
283  
284  
285  
286  
287  
288  
289  
290  
291  
292  
293  
294  
295  
296  
297  
298  
299  
300  
301  
302  
303  
304  
305  
306  
307  
308  
309  
310  
311  
312  
313  
314  
315  
316  
317  
318  
319  
320  
321  
322  
323  
324  
325  
326  
327  
328  
329  
330  
331  
332  
333  
334  
335  
336  
337  
338  
339  
340  
341  
342  
343  
344  
345  
346  
347  
348  
349  
350  
351  
352  
353  
354  
355  
356  
357  
358  
359  
360  
361  
362  
363  
364  
365  
366  
367  
368  
369  
370  
371  
372  
373  
374  
375  
376  
377  
378  
379  
380  
381  
382  
383  
384  
385  
386  
387  
388  
389  
390  
391  
392  
393  
394  
395  
396  
397  
398  
399  
400  
401  
402  
403  
404  
405  
406  
407  
408  
409  
410  
411  
412  
413  
414  
415  
416  
417  
418  
419  
420  
421  
422  
423  
424  
425  
426  
427  
428  
429  
430  
431  
432  
433  
434  
435  
436  
437  
438  
439  
440  
441  
442  
443  
444  
445  
446  
447  
448  
449  
450  
451  
452  
453  
454  
455  
456  
457  
458  
459  
460  
461  
462  
463  
464  
465  
466  
467  
468  
469  
470  
471  
472  
473  
474  
475  
476  
477  
478  
479  
480  
481  
482  
483  
484  
485  
486  
487  
488  
489  
490  
491  
492  
493  
494  
495  
496  
497  
498  
499  
500  
501  
502  
503  
504  
505  
506  
507  
508  
509  
510  
511  
512  
513  
514  
515  
516  
517  
518  
519  
520  
521  
522  
523  
524  
525  
526  
527  
528  
529  
530  
531  
532  
533  
534  
535  
536  
537  
538  
539  
540  
541  
542  
543  
544  
545  
546  
547  
548  
549  
550  
551  
552  
553  
554  
555  
556  
557  
558  
559  
560  
561  
562  
563  
564  
565  
566  
567  
568  
569  
570  
571  
572  
573  
574  
575  
576  
577  
578  
579  
580  
581  
582  
583  
584  
585  
586  
587  
588  
589  
590  
591  
592  
593  
594  
595  
596  
597  
598  
599  
600  
601  
602  
603  
604  
605  
606  
607  
608  
609  
610  
611  
612  
613  
614  
615  
616  
617  
618  
619  
620  
621  
622  
623  
624  
625  
626  
627  
628  
629  
630  
631  
632  
633  
634  
635  
636  
637  
638  
639  
640  
641  
642  
643  
644  
645  
646  
647  
648  
649  
650  
651  
652  
653  
654  
655  
656  
657  
658  
659  
660  
661  
662  
663  
664  
665  
666  
667  
668  
669  
670  
671  
672  
673  
674  
675  
676  
677  
678  
679  
680  
681  
682  
683  
684  
685  
686  
687  
688  
689  
690  
691  
692  
693  
694  
695  
696  
697  
698  
699  
700  
701  
702  
703  
704  
705  
706  
707  
708  
709  
710  
711  
712  
713  
714  
715  
716  
717  
718  
719  
720  
721  
722  
723  
724  
725  
726  
727  
728  
729  
730  
731  
732  
733  
734  
735  
736  
737  
738  
739  
740  
741  
742  
743  
744  
745  
746  
747  
748  
749  
750  
751  
752  
753  
754  
755  
756  
757  
758  
759  
760  
761  
762  
763  
764  
765  
766  
767  
768  
769  
770  
771  
772  
773  
774  
775  
776  
777  
778  
779  
780  
781  
782  
783  
784  
785  
786  
787  
788  
789  
790  
791  
792  
793  
794  
795  
796  
797  
798  
799  
800  
801  
802  
803  
804  
805  
806  
807  
808  
809  
810  
811  
812  
813  
814  
815  
816  
817  
818  
819  
820  
821  
822  
823  
824  
825  
826  
827  
828  
829  
830  
831  
832  
833  
834  
835  
836  
837  
838  
839  
840  
841  
842  
843  
844  
845  
846  
847  
848  
849  
850  
851  
852  
853  
854  
855  
856  
857  
858  
859  
860  
861  
862  
863  
864  
865  
866  
867  
868  
869  
870  
871  
872  
873  
874  
875  
876  
877  
878  
879  
880  
881  
882  
883  
884  
885  
886  
887  
888  
889  
890  
891  
892  
893  
894  
895  
896  
897  
898  
899  
900  
901  
902  
903  
904  
905  
906  
907  
908  
909  
910  
911  
912  
913  
914  
915  
916  
917  
918  
919  
920  
921  
922  
923  
924  
925  
926  
927  
928  
929  
930  
931  
932  
933  
934  
935  
936  
937  
938  
939  
940  
941  
942  
943  
944  
945  
946  
947  
948  
949  
950  
951  
952  
953  
954  
955  
956  
957  
958  
959  
960  
961  
962  
963  
964  
965  
966  
967  
968  
969  
970  
971  
972  
973  
974  
975  
976  
977  
978  
979  
980  
981  
982  
983  
984  
985  
986  
987  
988  
989  
990  
991  
992  
993  
994  
995  
996  
997  
998  
999  
1000

142  
143  
144  
145  
146  
147  
148  
149  
150  
151  
152  
153  
154  
155  
156  
157  
158  
159  
160  
161  
162  
163  
164  
165  
166  
167  
168  
169  
170  
171  
172  
173  
174  
175  
176  
177  
178  
179  
180  
181  
182  
183  
184  
185  
186  
187  
188  
189  
190  
191  
192  
193  
194  
195  
196  
197  
198  
199  
200  
201  
202  
203  
204  
205  
206  
207  
208  
209  
210  
211  
212  
213  
214  
215  
216  
217  
218  
219  
220  
221  
222  
223  
224  
225  
226  
227  
228  
229  
230  
231  
232  
233  
234  
235  
236  
237  
238  
239  
240  
241  
242  
243  
244  
245  
246  
247  
248  
249  
250  
251  
252  
253  
254  
255  
256  
257  
258  
259  
260  
261  
262  
263  
264  
265  
266  
267  
268  
269  
270  
271  
272  
273  
274  
275  
276  
277  
278  
279  
280  
281  
282  
283  
284  
285  
286  
287  
288  
289  
290  
291  
292  
293  
294  
295  
296  
297  
298  
299  
300  
301  
302  
303  
304  
305  
306  
307  
308  
309  
310  
311  
312  
313  
314  
315  
316  
317  
318  
319  
320  
321  
322  
323  
324  
325  
326  
327  
328  
329  
330  
331  
332  
333  
334  
335  
336  
337  
338  
339  
340  
341  
342  
343  
344  
345  
346  
347  
348  
349  
350  
351  
352  
353  
354  
355  
356  
357  
358  
359  
360  
361  
362  
363  
364  
365  
366  
367  
368  
369  
370  
371  
372  
373  
374  
375  
376  
377  
378  
379  
380  
381  
382  
383  
384  
385  
386  
387  
388  
389  
390  
391  
392  
393  
394  
395  
396  
397  
398  
399  
400  
401  
402  
403  
404  
405  
406  
407  
408  
409  
410  
411  
412  
413  
414  
415  
416  
417  
418  
419  
420  
421  
422  
423  
424  
425  
426  
427  
428  
429  
430  
431  
432  
433  
434  
435  
436  
437  
438  
439  
440  
441  
442  
443  
444  
445  
446  
447  
448  
449  
450  
451  
452  
453  
454  
455  
456  
457  
458  
459  
460  
461  
462  
463  
464  
465  
466  
467  
468  
469  
470  
471  
472  
473  
474  
475  
476  
477  
478  
479  
480  
481  
482  
483  
484  
485  
486  
487  
488  
489  
490  
491  
492  
493  
494  
495  
496  
497  
498  
499  
500  
501  
502  
503  
504  
505  
506  
507  
508  
509  
510  
511  
512  
513  
514  
515  
516  
517  
518  
519  
520  
521  
522  
523  
524  
525  
526  
527  
528  
529  
530  
531  
532  
533  
534  
535  
536  
537  
538  
539  
540  
541  
542  
543  
544  
545  
546  
547  
548  
549  
550  
551  
552  
553  
554  
555  
556  
557  
558  
559  
560  
561  
562  
563  
564  
565  
566  
567  
568  
569  
570  
571  
572  
573  
574  
575  
576  
577  
578  
579  
580  
581  
582  
583  
584  
585  
586  
587  
588  
589  
590  
591  
592  
593  
594  
595  
596  
597  
598  
599  
600  
601  
602  
603  
604  
605  
606  
607  
608  
609  
610  
611  
612  
613  
614  
615  
616  
617  
618  
619  
620  
621  
622  
623  
624  
625  
626  
627  
628  
629  
630  
631  
632  
633  
634  
635  
636  
637  
638  
639  
640  
641  
642  
643  
644  
645  
646  
647  
648  
649  
650  
651  
652  
653  
654  
655  
656  
657  
658  
659  
660  
661  
662  
663  
664  
665  
666  
667  
668  
669  
670  
671  
672  
673  
674  
675  
676  
677  
678  
679  
680  
681  
682  
683  
684  
685  
686  
687  
688  
689  
690  
691  
692  
693  
694  
695  
696  
697  
698  
699  
700  
701  
702  
703  
704  
705  
706  
707  
708  
709  
710  
711  
712  
713  
714  
715  
716  
717  
718

1  
2  
3  
4 the Bohaiwan and Songliao basins and along the boundary between the Yangtze Craton  
5  
6 and the South China Fold Belt. At longer periods (e.g., 30 sec), anisotropy is weaker than  
7  
8 at shorter periods, although it remains strong in the Tibetan Plateau and increases in  
9  
10 Japan. Unlike amplitude, the direction of anisotropy is generally consistent between the  
11  
12 three periods. This includes NW-SE fast directions across northern Tibet, nearly N-S  
13  
14 directions in southeastern Tibet, and NW-SE directions in Japan, which are perpendicular  
15  
16 to the Japan-Ryukyu subduction system. The purpose of this paper is to produce an  
17  
18 isotropic reference model, and further discussion on anisotropic structure is beyond its  
19  
20 scope.  
21  
22  
23  
24  
25  
26  
27

#### 28 **4. 3D Model**

29  
30  
31  
32 What emerges from surface wave tomography is a set of Rayleigh wave group and phase  
33  
34 speed curves with uncertainties, such as the examples shown in [Figure 7](#). For most of the  
35  
36 region of study these curves extend from 8 sec to 50 sec period, but in parts of South  
37  
38 China and Northeast China they extend up to 70 sec period. In addition, in some places  
39  
40 measurements do not extend down to 8 sec period. Considerable care has been taken with  
41  
42 data quality control and estimating realistic uncertainties. At their best, where eikonal  
43  
44 tomography works, the estimated uncertainties reflect the repeatability of the  
45  
46 measurements and allow a frequentist interpretation. Elsewhere, however, uncertainties  
47  
48 are extrapolations from regions where eikonal tomography delivers uncertainty  
49  
50 information. In these regions they represent our degree of belief in the measurements.  
51  
52  
53  
54  
55  
56  
57  
58  
59  
60

1  
2  
3  
4 The 3D model we present here is produced via a Bayesian Monte Carlo inversion so that  
5  
6  
7 a distribution of models is generated that fit the data acceptably. Within this framework,  
8  
9  
10 seismic models are conceived as random variables about which only probabilistic  
11  
12 statements are made. As described in greater detail by Shen et al. (2013a,b), the inversion  
13  
14 progresses in three steps that we briefly summarize here. (1) The starting point is the  
15  
16 generation of the prior distribution of candidate models which at each point on a  $0.5^\circ \times 0.5^\circ$   
17  
18 grid represents the range of models we wish to consider. The prior distribution is  
19  
20 governed by constraints on the range of values that model variables can take and relations  
21  
22 between the variables. In this paper we choose the allowed range of model variables to be  
23  
24 quite broad so that the posterior distribution, notably model uncertainties, will represent  
25  
26 the information found in the likelihood function, i.e, the data, much more strongly than  
27  
28 prior constraints. We believe that this is consistent with our intent to produce a reference  
29  
30 model, which is designed for use by other researchers. (2) A chain of candidate models in  
31  
32 the prior distribution is selected by a random walk in model space guided by the  
33  
34 Metropolis algorithm (Mosegaard and Tarantola, 1995), which is the “Monte Carlo”  
35  
36 aspect of this inversion. For each model selected, theoretical Rayleigh wave group and  
37  
38 phase speed curves are computed using the forward modeling code of Herrmann  
39  
40 (Herrmann, 2013) and the  $\chi^2$  misfit to the observed curves is determined. An individual  
41  
42 chain of models terminates when an equilibrium in model misfit is attained and we then  
43  
44 tabulate the models near equilibrium. A new chain is then begun at a random model from  
45  
46 the prior distribution and the process repeats. (3) The posterior distribution is determined  
47  
48  
49  
50  
51  
52  
53  
54  
55  
56  
57  
58  
59  
60

1  
2  
3  
4 by further considering the tabulated models compiled in Step 2. The best fitting model is  
5  
6 identified at each grid node and models there are accepted if their misfit is less than 50%  
7  
8 higher than that of the best fitting model. The posterior distribution is then summarized in  
9  
10 terms of the mean and standard deviation of each model variable or combination of  
11  
12 model variable (e.g., Vs at different depths, sedimentary thickness, crustal thickness, etc.).  
13  
14  
15 In addition, correlations between model variables and their combinations can be  
16  
17  
18  
19  
20 computed.  
21  
22

23  
24 In this section we present examples of aspects of this process and show the mean and  
25  
26 standard deviation of some of the principal model variables across the region of study.  
27  
28

#### 29 **4.1 Model parameterization**

30  
31  
32 The starting model around which we perturb is compiled from a combination of three  
33  
34 earlier models of Tibet (Yang et al., 2012), South China (Zhou et al., 2012), and  
35  
36 North/Northeast China extending to Japan (Zheng et al., 2011). The models in South and  
37  
38 North/Northeast China are on the same  $0.5^\circ \times 0.5^\circ$  grid we use, but we interpolate the  
39  
40 model of Tibet from  $1^\circ \times 1^\circ$  onto our grid.  
41  
42  
43  
44

45  
46 The model is primarily in Vs with Vp and density scaled to it, as discussed shortly.  
47

48  
49 Because only Rayleigh wave data are used in the inversion, formally speaking the shear  
50  
51 velocities are Vsv rather than Vs, but we refer to them as Vs throughout. In other words,  
52  
53 radial anisotropy is assumed to be zero, therefore  $V_p = V_{pv} = V_{ph}$ ,  $V_s = V_{sv} = V_{sh}$ , and  
54  
55  $\eta = 1$ . Sedimentary basins are represented with three unknowns: thickness and the top and  
56  
57  
58  
59  
60

1  
2  
3  
4 bottom  $V_s$  values that change linearly with depth in the basin. Shear wave speeds in the  
5  
6  
7 crystalline crust are represented with five cubic B-splines on the continent and four  
8  
9  
10 B-splines offshore. The thickness of the crystalline crust is also an unknown. Mantle  
11  
12 shear wave speeds from right below the Moho to 200 km depth are described by five  
13  
14  
15 cubic B-splines. Below 200 km, the model is a half-space where shear waves speed is  
16  
17  
18 constant and equal to the value at 200 km depth.  $V_p$  is computed from  $V_s$  such that  
19  
20  
21  $V_p/V_s = 2.0$  in the sediments,  $V_p/V_s = 1.79$  in the mantle following AK135 (Kennett et  
22  
23  
24 al., 1995), and in the crystalline crust the relationship between  $V_p$  and  $V_s$  is taken from  
25  
26  
27 Brocher (2005). Density ( $\rho$ ) is also computed from  $V_s$  using the relations provided by  
28  
29  
30 Brocher (2005) in the sediments and crystalline crust. In the mantle, density is  
31  
32  
33 determined based on the partial derivative of  $\rho$  with respect to  $V_s$  extracted from Hacker  
34  
35  
36 and Abers (2004) and applied relative to AK135. With these rules, we determine a  $V_p$  and  
37  
38  
39  $\rho$  model for every  $V_s$  model, and therefore for a distribution of  $V_s$  models we also have a  
40  
41  
42 distribution of models of  $V_p$  and  $\rho$ . However, because  $V_p$  and  $\rho$  are deterministically  
43  
44  
45 related to  $V_s$ , in the following we show only the  $V_s$  models.

46  
47  
48 Finally, the  $Q$  model is specified as follows. In the sediments and crust, the  $Q$  model is  
49  
50  
51 from AK135, in which  $Q_\mu$  is 600 in the crust and 80 in the sediments. These values are  
52  
53  
54 high enough that there is little physical dispersion in the crustal shear moduli. In the  
55  
56  
57 mantle, the  $Q_\mu$  model is taken from the global model of Dalton and Ekstrom (2006). The  
58  
59  
60 physical dispersion correction follows Anderson and Kanamori (1977).

## 4.2 Prior constraints and distributions

Prior constraints are of two types. First, we consider only particular ranges of perturbations to the starting model at each point, which is a combination of the three models of Yang et al. (2012), Zhou et al. (2012), and Zheng et al. (2011). In the parts of our study region not covered by these three models, we start from the global model of Shapiro et al. (2002). Consistent our intent that this is a reference model, ranges of allowed model values are broad so that the standard deviation of the posterior distribution will reflect information from data more than prior constraints. For the sediments, we allow sedimentary thickness to range from 0 km to 200% of the thickness of the starting model. If the starting model thickness is  $< 0.4$  km, we allow up to 0.8 km of sediments.  $V_s$  at the top and bottom of the sediments is allowed to changed by  $\pm 1$  km/s. If there are no sediments in the starting model at a particular location, we define the starting sedimentary model to possess 0.4 km of sediments with  $V_s$  at the top of the sediments equal to 1.5 km/s and at the bottom to 2.5 km/s. For the crystalline crust, we allow  $V_s$  to vary  $\pm 20\%$  relative to the starting model and crustal thickness to vary by  $\pm 15$  km. For the mantle, we allow  $V_s$  to change by  $\pm 20\%$  relative to the starting model. Second, in addition we place three further constraints on the model and between model variables. (1)  $V_s < 4.9$  km/s at all depths in the model. (2) The jumps in  $V_s$  from the sediments to the crystalline crust and from the crust to the mantle are positive. (3) At some places we impose the constraint that  $V_s$  in the crust increases monotonically with depth and refer to

1  
2  
3  
4 this as the “monotonicity constraint”. The use of cubic B-splines to represent seismic  
5  
6 structure between discontinuities imposes a fourth implicit constraint that vertical  
7  
8 variations between discontinuities are smooth. We see the application of these constraints  
9  
10 as a hypothesis test such that we choose to introduce further structural complexities only  
11  
12 where required by the data. As discussed shortly, the principal example of the release of a  
13  
14 constraint is that Tibet must be freed from the crustal monotonicity constraint to fit our  
15  
16 dispersion data. In particular, we release the constraint west of 110°E longitude where  
17  
18 surface elevation is higher than 2000 m.  
19

20  
21  
22  
23  
24  
25  
26 Examples of prior distributions for several model variables are shown with the white  
27  
28 histograms in [Figures 14-16](#) corresponding to the same three locations in South China,  
29  
30 Northeastern China, and Tibet for which the dispersion curves are shown in [Figure 7](#). The  
31  
32 prior distributions for sedimentary and crustal thickness (panels a and b in each figure,  
33  
34 respectively) are approximately uniform, whereas for the other variables they are not: (c)  
35  
36 velocity jump across Moho:  $V_s(4 \text{ km below Moho}) - V_s(4 \text{ km above Moho})$ , (d)  $V_s$  at 15  
37  
38 km depth, (e)  $V_s$  at 4 km above Moho, and (f)  $V_s$  at 100 km depth. The reason for the  
39  
40 non-uniformity of the other prior distributions is that the other variables are constrained  
41  
42 to co-vary with one another by the prior constraints. For example, the crustal  
43  
44 monotonicity constraint ensures that  $V_s$  at a lower level in the crust is greater than at all  
45  
46 higher levels and the prior distributions for crustal velocities appear as skew Gaussian  
47  
48 distributions.  
49  
50  
51  
52  
53  
54  
55  
56  
57  
58  
59  
60

### 4.3 Posterior distributions

Figures 14-16 superimpose the posterior distributions on the prior distributions at locations in South China, Northeast China, and Tibet. To understand the posterior distributions it is necessary to recognize that surface waves do not strongly constrain the depths to internal interfaces or velocity jumps across them. Therefore, the distributions of sedimentary (panel a) and crustal (panel b) thicknesses as well as the velocity jump across Moho (panel c) at all three locations are quite broad. The single exception is in South China where the distribution of crustal thickness peaks relatively sharply near 35 km (Fig. 14b). In this case Rayleigh wave velocities, particularly the Airy phase on the group velocity curve, impose relatively strong constraints on crustal thickness because the structure at this point is simple and there are not strong trade-offs with, for example, sedimentary thickness and velocity. Because the jump across Moho generally is not well constrained, neither will  $V_s$  near the Moho be well constrained, which accounts for the fact that the posterior distributions at all three points are broad 4 km above Moho. However, within the crust and mantle well away from internal interfaces, the posterior distributions of  $V_s$  are quite sharp.

We summarize the posterior distributions with their means and standard deviations, and maps of these quantities are presented and discussed in section 5. As we have discussed here, broad posterior distributions will produce a poorly determined mean with a large standard deviation. Generally speaking, the standard deviations of the posterior

1  
2  
3  
4 distributions in our model are relatively larger for depths near crustal than for shear  
5  
6 waves speeds within the crust and mantle. Thus, inspection of the posterior distributions  
7  
8 reveals that inversions based on surface wave dispersion data alone constrain shear wave  
9  
10 speeds relatively well within the interior of the crust and uppermost mantle and the  
11  
12 depths and nature of the interfaces are much more poorly determined. This can be seen  
13  
14 more clearly in plots of the envelope of accepted models such as those presented in  
15  
16 **Figure 17**, which are for the same three locations shown in **Figure 7** and **Figures 14-16** in  
17  
18 Tibet, South China, and Northeast China. The envelopes of these models broaden near the  
19  
20 surface and near the Moho due to trade-offs between model variables, but reduce  
21  
22 appreciably within the crust and uppermost mantle. The exception is in Tibet where the  
23  
24 envelope does not narrow in the mantle. This reflects the fact that dispersion data in Tibet  
25  
26 extend only up to 50 sec period, where there is still a strong but unresolved sensitivity to  
27  
28 both crustal thickness (given the deep Moho beneath Tibet) and mantle shear wave  
29  
30 speeds.  
31  
32

33  
34 Examples of the fit to the input dispersion curves by the mean of the posterior  
35  
36 distribution at the same three locations are presented in **Figure 7**. Misfit is defined as the  
37  
38 square root of reduced  $\chi^2$  value at each location as follows:  
39  
40  
41

$$\text{Misfit} = \left[ \frac{1}{N} \sum_{i=1}^N \frac{(d_i - p_i)^2}{S_i^2} \right]^{1/2} \quad (2)$$

42  
43  
44  
45  
46  
47  
48  
49  
50  
51  
52  
53  
54  
55 where  $d_i$  is an observed Rayleigh wave phase or group speed,  $p_i$  is the corresponding  
56  
57  
58  
59  
60

1  
2  
3  
4 model predicted value,  $\sigma_i$  is the one standard deviation uncertainty in the phase or group  
5  
6 speed,  $i$  is an index that ranges over the discrete phase and group speed measurements,  
7  
8 and  $N$  is the number of these measurements. A misfit of one standard deviation on  
9  
10 average would result in a Misfit estimate equal to about 1. For the Northeast China  
11  
12 location in [Figure 7c](#), Misfit is 0.94 consistent with a misfit of about 1 standard deviation.  
13  
14 The Misfit at the South China location ([Fig. 7b](#)), however, is 0.54, which may indicate  
15  
16 that uncertainties are too large at this point or that the model is over-parameterized  
17  
18 somewhat. [Figure 7c](#) illustrates that the Misfit at the location in Tibet depends on how we  
19  
20 parameterize the model. The dispersion curves predicted from the crustal model produced  
21  
22 with the monotonicity constraint are shown with the dashed lines in [Figure 7a](#), which  
23  
24 generates a Misfit of 2.17. With the crustal monotonicity constraint imposed in Tibet, we  
25  
26 misfit the data badly. However, if we release this constraint we are able to fit the data  
27  
28 well, generating a Misfit of 0.91 at the location in [Figure 7a](#). The reason is that Tibet  
29  
30 possesses a low velocity zone in the central crust (e.g., Yang et al., 2012; Xie et al., 2013;  
31  
32 Jiang et al., 2014; Deng et al., 2015), which is required to fit the dispersion data. Thus, as  
33  
34 mentioned above, we release the crustal monotonicity constraint in Tibet west of 110°  
35  
36 East longitude wherever surface elevation is greater than 2000 m.  
37  
38  
39  
40  
41  
42  
43  
44  
45  
46  
47  
48

49  
50 The Misfit map computed using the mean model in the posterior distribution at each  
51  
52 location is presented in [Figure 18a](#) and the distribution of Misfit is presented by the  
53  
54 histogram in [Figure 18b](#). Misfit is typically less than 1 except in far western Tibet west of  
55  
56  
57  
58  
59  
60

1  
2  
3  
4 a longitude of 95°E and in the Sea of Japan. These are the two areas where we have the  
5  
6  
7 fewest stations and the high Misfit values probably indicate that data uncertainties are  
8  
9  
10 somewhat too small in these regions. However, across most of the region of study, the  
11  
12 level of Misfit is consistent with the conclusion that data uncertainties are approximately  
13  
14  
15 correct and that the model generally possesses the right number of degrees of freedom.  
16

## 17 18 **5. Results** 19

20  
21 The model we present here (mean of the posterior distribution) together with its attendant  
22  
23 uncertainties (standard deviation of the posterior distribution) are available via the IRIS  
24  
25 Earth Model Collaboration (Trabant et al., 2012) at: <http://ds.iris.edu/ds/products/emc/>.  
26  
27  
28 At the time of publication, the model, uncertainties, and the dispersion maps are also  
29  
30  
31 available via the CU-Boulder web site at: <http://ciei.colorado.edu/Models> and  
32  
33  
34 <http://ciei.colorado.edu/DispMaps>.  
35  
36

37  
38 The means and standard deviations of the posterior distributions across the study region  
39  
40 are displayed at a variety of depths within the crust and uppermost mantle and for crustal  
41  
42 thickness in [Figures 19-21](#). Information about crustal shear wave speeds is found in  
43  
44  
45 [Figure 19](#), crustal thickness in [Figure 21](#), and mantle shear wave speeds in [Figure 20](#).  
46  
47  
48 Vertical transects through the model are identified in [Figure 22](#) and shown in [Figure 23](#).  
49  
50

### 51 52 **5.1 Crustal structure and uncertainties** 53

54  
55 In the shallow crust, the pattern of shear wave speeds between the free surface and 6 km  
56  
57 depth, presented as 3 km in [Figure 19a](#), are dominated by the existence or absence of  
58  
59  
60

1  
2  
3  
4 sediments such that the major sedimentary basins across China and offshore appear as  
5  
6 slow. These include the Junggar, Tarmin, Sichuan, Jiangnan, North China (Bohaiwan,  
7  
8 Taikang Hefei), and Songliao basins onshore along with basins offshore (East China Sea,  
9  
10 Subei Yellow Sea, Tsushima). As illustrated by [Figures 14-16](#), surface wave dispersion  
11  
12 alone does not constrain sedimentary characteristics uniquely; e.g., there is a strong  
13  
14 trade-off between the thickness and average shear wave speeds within the sedimentary  
15  
16 column as well as with the shear wave speeds in the shallow part of the underlying  
17  
18 crystalline crust. For this reason, we do not present maps of sedimentary thickness, but  
19  
20 rather show the shear wave speed averaged in the top 6 km near the surface of our model.  
21  
22  
23  
24  
25  
26  
27  
28 The average shear wave speed offshore includes the water layer in which shear wave  
29  
30 speed is zero, which is why the average is low offshore particularly in the Sea of Japan  
31  
32 where water depth is largest. Moreover, our model of the vertical variation of  $V_s$  with  
33  
34 depth within the sediments is crude, being a linear function of depth. The diagenesis and  
35  
36 metamorphism of sediments produce a more complicated depth dependence than such a  
37  
38 simple model. Our model of sediments exists for the most part, therefore, to capture the  
39  
40 effects of sedimentary basins on surface wave propagation so that deeper structures can  
41  
42 be revealed reliably.  
43  
44  
45  
46  
47  
48  
49

50 In the middle crust, shear wave speeds near 20 km depth are presented in [Figure 19c](#).

51  
52  
53 Mid-crustal  $V_s$  in Tibet is anomalously low due to the well known low velocity zone that  
54  
55 characterizes the Tibetan crust (e.g., Cotte et al., 1999; Rapine et al., 2003; Shapiro et al.,  
56  
57  
58  
59  
60

1  
2  
3  
4 2004; Guo et al., 2009; Yang et al., 2012; Xie et al., 2013;), which has been taken as  
5  
6  
7 evidence for the presence of partial melt (e.g., Kind et al., 1996; Caldwell et al., 2009;  
8  
9  
10 Chen et al., 2014; Hacker et al., 2014). The middle crust across East China is fairly  
11  
12 homogeneous, with the exception of higher Vs beneath the Sichuan basin and Ordos  
13  
14 block and lower Vs beneath the Yangtze craton south of the Sichuan basin and beneath  
15  
16 the Tianshan terrane and Outer Mongolia (e.g., Tamtsag Halar and Erlan basins).  
17  
18  
19  
20 Offshore, Vs near 20 km depth beneath the Sea of Japan is so high because this depth is  
21  
22 in the mantle due to the thin oceanic crust.  
23  
24

25  
26 In the lower crust, a strong east-west dichotomy is observed at 40 km depth in [Figure 19e](#).

27  
28 This is because the crust thins eastward beneath China and crosses 40 km near the  
29  
30 North-South gravity lineament (dashed line in [Fig. 21](#)). West of the North-South gravity  
31  
32 lineament, 40 km depth lies in the crust. In this region outside of Tibet, for example  
33  
34 beneath the Sichuan basin, the Ordos block, and the Tarim basin, 40 km lies in the very  
35  
36 deep and presumably mafic lower crust with shear wave speeds above 4.0 km/s. In  
37  
38 contrast, beneath Tibet 40 km lies in the middle crust, which has much lower shear wave  
39  
40 speeds. Much of the Songpan-Ganzi terrane at this depth has  $V_s < 3.5$  km/s. East of the  
41  
42 North-South gravity lineament, 40 km depth lies in the mantle and Vs is relatively  
43  
44 homogeneous across this region. Variations in mantle Vs can be seen more clearly in  
45  
46  
47  
48  
49  
50  
51  
52 [Figure 20](#).

53  
54  
55  
56 Crustal thickness estimates are presented in [Figure 21](#). On average, the crust thins  
57  
58  
59  
60

1  
2  
3  
4 eastward. As just discussed, the North-South gravity lineament marks the approximate  
5  
6 locus of points for 40 km thick crust. The crust is thickest in central Tibet, where we  
7  
8 estimate crustal thickness above 65 km, and is thinnest beneath the Sea of Japan with  
9  
10 crust less than 15 km thick.  
11

12  
13  
14  
15 Uncertainties in crustal shear velocities and crustal thickness, defined as the standard  
16  
17 deviation of the posterior distribution at each point, are also presented in **Figures 19** and  
18  
19 **21**. Uncertainties at shallow depths (**Fig. 19b**) are highest beneath sedimentary basins due  
20  
21 to structural trade-offs, as already discussed, and in the western parts of our model where  
22  
23 station density is lowest (e.g., longitudes west of 95°E). In the middle crust (**Fig. 19d**), on  
24  
25 the continent uncertainties are much smaller due to the separation of 20 km depth from  
26  
27 crustal interfaces, notably the sediment-crystalline crust boundary and the Moho. This is  
28  
29 mitigated somewhat in regions with thick sediments (e.g., Songliao basin, North China  
30  
31 basins). Uncertainties are also relatively large in western Tibet and beneath the Tarim  
32  
33 basin due to rarified station coverage. Offshore, however, uncertainties are much larger at  
34  
35 this depth because the crust is thinner and the Moho approaches 20 km in many locations.  
36  
37 At 40 km depth, the magnitude of the uncertainties (**Fig. 19f**) is also controlled by the  
38  
39 proximity to the Moho. East of the North-South gravity lineament uncertainties are large  
40  
41 and west of it they are smaller, except near the periphery of Tibet and beneath the Tarim  
42  
43 basins where crustal thickness approaches 40 km from above. In contrast, uncertainties  
44  
45 beneath the Sea of Japan are quite small. Uncertainties in crustal thickness (**Fig. 21b**) also  
46  
47  
48  
49  
50  
51  
52  
53  
54  
55  
56  
57  
58  
59  
60

1  
2  
3  
4 scale with crustal thickness so that they are largest beneath Tibet and smallest beneath the  
5  
6 Sea of Japan and the South China block. This is largely due to the band-limited content of  
7  
8 the data we use. Beneath Tibet, for example, the data only extend to 50 sec period, which  
9  
10 is not long enough to constrain mantle Vs well and reduce its trade-off with Moho depth.  
11  
12  
13

## 14 **5.2 Mantle structure and uncertainties**

15  
16  
17  
18 At 60 km depth (Fig. 20a), which is predominantly in the mantle except beneath parts of  
19  
20 Tibet, the highest Vs values occur beneath the major basins including part of the Songliao,  
21  
22 Sichuan, and Tarim basins and the Ordos block where  $V_s > 4.5$  km/s. Beneath Tibet, the  
23  
24 crust is so thick that it envelopes 60 km, and average lower crustal Vs is about 3.7 km/s.  
25  
26  
27  
28  
29  
30  
31  
32  
33  
34  
35  
36  
37  
38  
39  
40  
41  
42  
43  
44  
45  
46  
47  
48  
49  
50  
51  
52  
53  
54  
55  
56  
57  
58  
59  
60  
Uncertainties at this depth (Fig. 20b) also reflect the relative proximity to the nearest  
discontinuity, which is the Moho, and are higher where the crust is thicker. East of the  
North-South gravity lineament, where Moho lies above 40 km depth, uncertainties  
average about 70 m/s, which is about 1.5%. In many respects, the model is similar at  
depths of 80 km and 120 km (Figs. 20c,e), and the content of the model at these depths is  
discussed in the following paragraphs. The geographical distributions of uncertainties at  
80 km and 120 km are similar (Figs. 20d,f). However, uncertainties are larger at 120 km  
because our band-limited dispersion measurements begin to lose resolution below 100  
km. The exception to this is beneath South China and Northeast China where we have  
earthquake derived dispersion measurements, which illustrates why we have taken pains  
to introduce these measurements.

1  
2  
3  
4 A blow up of the model at 80 km depth, which is in the uppermost mantle everywhere in  
5  
6 our study region, is presented in **Figure 22**. High velocity anomalies at this depth underlie  
7  
8 that principal sedimentary basins (Tarim, Songliao, Jiangnan, Taikang Hefei, Sichuan)  
9  
10 and the Ordos block. In addition there are high velocity anomalies beneath the Lhasa  
11  
12 terrane in southern Tibet, the Greater Xing'an Range, and the Yellow Sea. The high  
13  
14 velocity anomaly beneath the Sichuan basin extends well outside the basin, and occupies  
15  
16 much of the western Yangtze craton, so we will refer to it as the western Yangtze craton.  
17  
18  
19  
20  
21  
22 The highest velocities underlie the Tarim basin, the western Yangtze craton, and the  
23  
24 Ordos block. We believe these structures reflect the ancient origin of these tectonic  
25  
26 features and contrast with the weaker positive velocity anomaly that underlies the next  
27  
28 largest basin in our study region, the Songliao basin, which is believed to have formed  
29  
30  
31  
32  
33  
34  
35  
36  
37  
38  
39  
40  
41  
42  
43  
44  
45  
46  
47  
48  
49  
50  
51  
52  
53  
54  
55  
56  
57  
58  
59  
60

Low velocity anomalies include low wave speed beneath northern Tibet that have  
reported by previous researchers (e.g., Shapiro et al., 2002; Yang et al., 2012; Xie et al.,  
2014), an anomaly related to Datong volcano merging into a “horseshoe shaped” or  
“crescent shaped” (small green dashed oval) anomaly that outlines the northern part of  
the North China Plain, and a “Y-shaped” (large green dashed oval) anomaly that  
encompasses both near coastal areas of Northeast China, North Korea, and South Korea  
as well as more seaward areas along the Ryukyu subduction zone and the eastern  
periphery of the Sea of Japan. The “horseshoe shaped” and “Y-shaped” anomalies were

1  
2  
3  
4 discussed in some detail by Zheng et al. (2011), but are now imaged more sharply due to  
5  
6  
7 the introduction of data from the Korean Seismic Network and the NECESS array.  
8

9  
10 The low velocity anomaly beneath northern Tibet has been interpreted as a remnant of a  
11  
12 gravitational instability that caused the foundering of unstable lithosphere (England et al.,  
13  
14 1988; Kosarev, 1999). The horseshoe shaped anomaly has also been interpreted to result  
15  
16 from the broadly hypothesized delamination (or some similar process) of the lithosphere  
17  
18 beneath the North China craton by Zheng et al. (2011). Zheng et al. (2011) interpret the  
19  
20 Y-shaped anomaly as deriving from upwelling fluids derived from the subducting slab  
21  
22 beneath and adjacent to the Sea of Japan. The recent P-wave tomography study of Tang et  
23  
24 al. (2014) images a similar anomaly in the mantle but interprets it as a deep seated  
25  
26 upwelling that penetrates through the slab from the lower mantle.  
27  
28  
29  
30  
31  
32

### 33 34 **5.3 Vertical transects through the model**

35  
36  
37 Upper mantle structure and perhaps to a lesser extent crustal structure can be seen in an  
38  
39 illuminating way with vertical transects such as those identified in [Figure 22](#) and  
40  
41 presented in [Figure 23](#). Transect A-A' goes through Northeast China from the Greater  
42  
43 Xing'an Range, through the Songliao basin, passing beneath Changbaishan volcano, and  
44  
45 then through the southern Sea of Japan to terminate near Japan. The uppermost mantle  
46  
47 beneath the Great Xi'an Range and the western Songliao basin is fast, as is the shallow  
48  
49 lithosphere beneath the Sea of Japan. Beneath the Changbaishan the mantle is quite slow,  
50  
51 however, and upper mantle low velocity anomalies bracket the Sea of Japan as part of the  
52  
53  
54  
55  
56  
57  
58  
59  
60

1  
2  
3  
4 so called “Y-shaped” anomaly identified by Zheng et al. (2011). The crust can be seen to  
5  
6  
7 thin sharply beneath the Sea of Japan and slightly beneath the Songliao basin.  
8

9  
10 The other vertical transects shown in **Figure 23** are much longer than transect A-A’.

11  
12 Transect B-B’ extends from Tibet, through the Ordos block, passing beneath Datong  
13  
14 volcano and the Yangshan Foldbelt, and then through the Songliao basin to terminate in  
15  
16 the Lesser Xing-An Range east of the basin. The most prominent mantle anomalies are  
17  
18 the thick, high velocity lithosphere that underlies the Ordos block and the very low  
19  
20 velocity anomaly that underlies Datong volcano. The difference between the high  
21  
22 velocity upper mantle beneath southern Tibet and the lower velocities beneath northern  
23  
24 Tibet is also apparent. This profile also captures the difference between the fast western  
25  
26 and slow eastern Songliao basin. Transect B-B’ also shows low velocity middle crust in  
27  
28 northern Tibet, very fast lower crust beneath the Ordos, crustal thickening beneath Tibet  
29  
30 and thinning beneath the Songliao basin.  
31  
32  
33  
34  
35  
36  
37  
38

39  
40 Transects C-C’ and D-D’ also start in Tibet on the West. C-C’ extends through the western  
41  
42 Yangtze craton, including the Sichuan basin, through the South China block, and  
43  
44 terminates off the coast in the South China Sea north of Taiwan. In Tibet, this transect  
45  
46 goes exclusive through the low velocity uppermost mantle of Northern Tibet. Low  
47  
48 velocities in the mantle also underlie the South China foldbelt below 60 km depth,  
49  
50 characteristic of thin lithosphere in this region. Most prominently, however, are the high  
51  
52 velocities beneath the western Yangtze craton, which is the strongest mantle high velocity  
53  
54  
55  
56  
57  
58  
59  
60

1  
2  
3  
4 anomaly in the study region. Crustal features include the mid-crustal low velocity zone in  
5  
6 Tibet, the thick sediments of the Sichuan basin, and exceptionally high velocity lower  
7  
8 crust in the western Yangtze craton. Transect D-D' emerges from Tibet and goes through  
9  
10 the Qaidam basin, the Qilianshan block, the Ordos block, and the northern reaches of the  
11  
12 North China Plain, and then extends through the Yellow Sea, the Korean Peninsula, and  
13  
14 the southernmost Sea of Japan before terminating near Japan. Many of the features seen  
15  
16 in this transect were mentioned for previously discussed transects. In addition to the  
17  
18 Ordos block, particularly prominent features in this transect include thick sediments  
19  
20 beneath the Qaidam and North China basins, thin lithosphere beneath the North China  
21  
22 Plain, and the low velocity anomalies that bracket the Sea of Japan.  
23  
24  
25  
26  
27  
28  
29  
30

## 31 **6. Conclusions**

32  
33  
34 The purpose of this study is to produce a reference model for the crust and uppermost  
35  
36 mantle beneath the study region, which encompasses all of China and extends eastward  
37  
38 into the marginal seas, through North and South Korea, to Japan. By “reference model”  
39  
40 we mean a seismic model that is designed to be used by researchers other than its authors.  
41  
42 In our view, a reference model has three necessary characteristics. (1) Uncertainties are  
43  
44 estimated for the model variables. (2) The data on which the model is based are available  
45  
46 to other researchers. (3) The model itself and uncertainties are available to other  
47  
48 researchers. In addition, it is advantageous if the reference model is based on a uniform  
49  
50 quality control procedure applied to all observables and if prior constraints are clearly  
51  
52  
53  
54  
55  
56  
57  
58  
59  
60

1  
2  
3  
4 described and also preferably broad.  
5  
6

7 Using data from more than 2000 seismic stations taken from multiple networks arrayed  
8  
9 across China (CEArray, China Array, NECESS, PASSCAL, GSN) and surrounding  
10  
11 regions (Korean Seismic Network, F-Net, KNET) we perform ambient noise Rayleigh  
12  
13 wave tomography across the entire region of study and earthquake tomography across  
14  
15 parts of South China and Northeast China. The same quality control procedures are  
16  
17 applied to all ambient noise data and all earthquake data. We produce isotropic Rayleigh  
18  
19 wave group and phase speed maps with uncertainties from 8 to 50 sec period across the  
20  
21 entire region of study, which are extended to 70 sec period where earthquake tomography  
22  
23 is performed. In producing the isotropic maps, we also generate maps of azimuthal  
24  
25 anisotropy to reduce potential anisotropic bias. These isotropic maps and the associated  
26  
27 uncertainties are the basis for the 3D model.  
28  
29  
30  
31  
32  
33  
34  
35  
36

37 The 3D model is produced using a Bayesian Monte Carlo formalism on a  $0.5^\circ \times 0.5^\circ$  grid  
38  
39 across the study area. The starting model for the inversion is compiled from the models  
40  
41 described by Yang et al. (2012) for Tibet, Zheng et al. (2011) for North/Northeast China  
42  
43 and environs, and Zhou et al. (2012) for South China and, where they do not exist, from  
44  
45 the global model of Shapiro et al. (2002). Because we seek to produce a model that will  
46  
47 be useful to other researchers, we intentionally keep prior bounds on the model broad.  
48  
49

50 Such uninformative priors result in posterior distributions that more strongly reflect  
51  
52 information in the data than prior information, about which other researchers may differ  
53  
54  
55  
56  
57  
58  
59  
60

1  
2  
3  
4 from us. The principal exception is that we attempt to fit the data with a vertically smooth  
5  
6 or simple model between interfaces at the base of the sediments and crust. We  
7  
8 acknowledge that the earth may not be vertically smooth, but believe that inference of  
9  
10 vertically rough structures, such as the introduction of more crustal interfaces, needs to be  
11  
12 compelled by the data, particularly for a reference model. The most stringent constraint  
13  
14 that we impose is the “monotonicity constraint”, which ensures that  $V_s$  increases with  
15  
16 depth in the crust. Due to the crustal low velocity zone in the Tibetan middle crust (e.g.  
17  
18 Shapiro et al., 2002; Yang et al., 2012; Xie et al., 2013), our data cannot be fit in Tibet  
19  
20 with this constraint; thus, we release it west of  $110^\circ\text{E}$  longitude where surface elevation is  
21  
22 higher than 2000 m. Elsewhere in the study region the crustal monotonicity constraint has  
23  
24 been applied.  
25  
26  
27  
28  
29  
30  
31  
32  
33

34 We define the final model as the mean and standard deviation of the posterior distribution  
35  
36 on a  $0.5^\circ \times 0.5^\circ$  grid from the surface to 150 km depth. The mean model fits the dispersion  
37  
38 data at about one data standard deviation, on average, indicating that the model is not  
39  
40 systematically over or under-parameterized relative to the size of data uncertainties.  
41  
42  
43

44 Rayleigh wave dispersion, unfortunately, does not constrain internal interfaces well.

45 Because our model is based on Rayleigh wave dispersion alone and prior information is  
46  
47 broad, sedimentary and crustal thicknesses and related variables are not precisely  
48  
49

50 determined: their posterior distributions encompass much of their prior distributions. In  
51  
52

53 contrast, shear wave speeds between discontinuities in the crystalline crust and below the  
54  
55  
56  
57  
58  
59  
60

1  
2  
3  
4 Moho in the uppermost mantle are well determined and compose most of the information  
5  
6  
7 content in our model.  
8

9  
10 The features that appear in the model display great variety and considerable richness both  
11  
12 in the crust and in the uppermost mantle. We highlight only five here. (1) The major  
13  
14 sedimentary basins dominate structures that we see in the uppermost crust, particularly  
15  
16 for the Songliao, Bohaiwan, Jiangnan, Sichuan, Qaidam, and Tarim basins. (2) An  
17  
18 anomalously low velocity channel appears in the middle crust of the Tibetan Plateau, in  
19  
20 contrast with relatively fast middle crust in eastern China. (3) The principal lower crustal  
21  
22 anomalies are exceptionally high velocities beneath the sedimentary basins, most  
23  
24 prominently beneath the Ordos Block. (4) Crustal thickness varies from less than 15 km  
25  
26 beneath the Sea of Japan to more than 60 km beneath the Tibetan Plateau, and the 40 km  
27  
28 crustal thickness boundary coincides approximately with the North-South Gravity  
29  
30 Lineament dividing continental China into two distinct zones. (5) In the uppermost  
31  
32 mantle, the most notable features are fast anomalies beneath the Sichuan basin and the  
33  
34 Ordos Block and slow anomalies comprising the “horse-shoe” shaped anomaly  
35  
36 surrounding the North China Plain and the “Y-shaped” anomaly bracketing the Sea of  
37  
38 Japan. Relatively slow anomalies are observed beneath northern Tibet. The slow  
39  
40 anomalies are related either to delamination/gravitational instability or the subduction of  
41  
42 the Pacific Plate. Each of these features deserves further detailed discussion, which is  
43  
44 beyond the scope of this paper.  
45  
46  
47  
48  
49  
50  
51  
52  
53  
54  
55  
56  
57  
58  
59  
60

1  
2  
3  
4 We present the reference model as a basis for future research and see it as representing a  
5  
6 first iterate. It is designed to be used as a basis for predicting waveform characteristics,  
7  
8 such as surface and body wave amplitudes and travel times, and with the right  
9  
10 interpretation to predict other kinds of data such as surface topography and gravity (e.g.,  
11  
12 Levandowski et al., 2014). Although the model reflects the content of an exceptionally  
13  
14 large data set of inter-station surface wave dispersion measurements, the introduction of  
15  
16 more and various types of data will bring it into closer coincidence with the earth. The  
17  
18 joint inversion performed with receiver functions (Shen et al., 2012, 2013a,b; Deng et al.,  
19  
20 2015) and Rayleigh wave ellipticity or H/V (Lin et al., 2012, 2014) is a natural candidate  
21  
22 for future refinements. For example, Deng et al. (2015) shows that the joint inversion of  
23  
24 the dispersion data we present here with receiver functions in northern Tibet requires the  
25  
26 introduction of internal interfaces within the Tibetan middle crust as well a doublet Moho,  
27  
28 and reveals a step in Moho north of the Kunlun fault. Kang et al. (2015) assimilates our  
29  
30 data and inverts together with receiver functions and Rayleigh wave H/V ratio from the  
31  
32 NECESS Array experiment and observes an asymmetric Moho depth variation, thinning  
33  
34 from the west to the east, beneath the Songliao basin, attributed recent mantle upwelling  
35  
36 beneath the Changbaishan Volcano. The continued installation and movement of China  
37  
38 Array, in particular, promise a wealth of new information on which to base future  
39  
40 refinements and improvements to the reference model at much higher resolution.  
41  
42  
43  
44  
45  
46  
47  
48  
49  
50  
51  
52  
53  
54  
55  
56  
57  
58  
59  
60

## Acknowledgments

The authors are grateful to Fan-Chin Lin for facilitating collaboration between the University of Colorado and Seoul National University. DK, JN, WW, YZ, and LZ all had extended work visits to the University of Colorado during which aspects of this work were completed, and they thank the following funding agencies for supported their visits: Chinese Geological Survey, National Science Foundation of China and China Scholarship Council. Aspects of this research were supported by NSF grant EAR-1246925 at the University of Colorado at Boulder. The facilities of IRIS Data Services, and specifically the IRIS Data Management Center, were used for access to waveforms, related metadata, and/or derived products used in this study. IRIS Data Services are funded through the Seismological Facilities for the Advancement of Geoscience and EarthScope (SAGE) Proposal of the National Science Foundation under Cooperative Agreement EAR-1261681. China Array waveform data and some of the CEA array waveform data were provided by the Data Management Center of the China National Seismic Network at the Institute of Geophysics and China Seismic Array Data Management Center at the Institute of Geophysics, China Earthquake Administration (Zheng et al., 2010a). The China Array Project was supported by China National Special Fund for Earthquake Scientific Research in Public Interest (201008011) and WW's contribution has been supported by NSFC grant 41374070. YZ's contribution has been supported by NSFC grants 41422401 and 41174086. YK acknowledges National Research Foundation of Korea Grant funded by the Korean Government (MEST) (NRF-2014S1A2A2027609), and also acknowledges NECIS website (in Korean) for the data. This work utilized the Janus supercomputer, which is supported by the National Science Foundation (award number CNS-0821794), the University of Colorado at Boulder, the University of Colorado Denver and the National Center for Atmospheric Research. The Janus supercomputer is operated by the University of Colorado at Boulder.

## References

- Acton, C.E., K. Priestley, V.K. Gaur, and S.S. Rai, 2010. Group velocity tomography of the Indo-Eurasian collision zone, *J. Geophys. Res.*, 115, B12335, doi:10.1029/2009JB007021.
- Bao, X., Song, X., & Li, J., 2015. High-resolution lithospheric structure beneath Mainland China from ambient noise and earthquake surface-wave tomography. *Earth and Planetary Science Letters*, 417, 132-141.
- Bao, X., Song, X., Xu, M., Wang, L., Sun, X., Mi, N., ... & Li, H., 2013. Crust and upper mantle structure of the North China Craton and the NE Tibetan Plateau and its tectonic implications. *Earth and Planetary Science Letters*, 369, 129-137.
- Barmin, M.P., M.H. Ritzwoller, and A.L. Levshin, 2001. A fast and reliable method for surface wave tomography, *Pure Appl. Geophys.*, 158(8), 1351 - 1375.
- Bensen, G.D., M.H. Ritzwoller, M.P. Barmin, A.L. Levshin, F. Lin, M.P. Moschetti, N.M. Shapiro, and Y. Yang, 2007. Processing seismic ambient noise data to obtain reliable broad-band surface wave dispersion measurements, *Geophys. J. Int.*, 169, 1239-1260, doi: 10.1111/j.1365-246X.2007.03374.x.
- Brocher, T. M., 2005. Empirical relations between elastic wavespeeds and density in the Earth's crust. *Bulletin of the Seismological Society of America*, 95(6), 2081-2092.
- Caldwell, W.B., S.L. Klemperer, S.S. Rai, and J.F. Lawrence, 2009. Partial melt in the the upper-mantle crust of the northwest Himalaya revealed by Rayleigh wave dispersion,

1  
2  
3  
4 *Tectonophys.*, 477, 58-65.  
5  
6

7 Chen, M., Huang, H., Yao, H., Hilst, R., & Niu, F., 2014. Low wave speed zones in the  
8 crust beneath SE Tibet revealed by ambient noise adjoint tomography. *Geophysical*  
9 *Research Letters*, 41(2), 334-340.  
10  
11

12  
13  
14  
15 Cotte, N., H. Pederson, M. Campillo, J. Mars, J.F. Ni, R. Kind, E. Sondvol, and W. Zhao,  
16  
17 1999. Determination of the crustal structure in southern Tibet by dispersion and  
18  
19 amplitude analysis of Rayleigh waves, *Geophys. J. Int.*, 138, 809-819.  
20  
21

22  
23  
24 Deng, Y., W. Shen, T. Xu, and M.H. Ritzwoller, 2015. Crustal layering in northeastern  
25  
26 Tibet: A case study based on joint inversion of receiver functions and surface wave  
27  
28 dispersion, *Geophys. J. Int.*, submitted.  
29  
30

31  
32 England, P. C., Houseman, G. A., Osmaston, M. F., & Ghosh, S. (1988). The mechanics  
33  
34 of the Tibetan Plateau [and discussion]. *Philosophical Transactions of the Royal*  
35  
36 *Society of London A: Mathematical, Physical and Engineering Sciences*, 326(1589),  
37  
38 301-320.  
39  
40

41  
42  
43 Guo, Z., X. Gao, H. Yao, J. Li, and W. Wang, 2009. Midcrustal low-velocity layer  
44  
45 beneath the central Himalaya and southern Tibet revealed by ambient noise array  
46  
47 tomography, *Geochem. Geophys. Geosys.*, 10(5), Q05007,  
48  
49 doi:10.1029/2009GC002458.  
50  
51

52  
53  
54 Guo, Z., Gao, X., Wang, W., & Yao, Z., 2012. Upper-and mid-crustal radial anisotropy  
55  
56 beneath the central Himalaya and southern Tibet from seismic ambient noise  
57  
58  
59  
60

1  
2  
3  
4 tomography. *Geophysical Journal International*, 189(2), 1169-1182.

5  
6  
7 Guo, Z., Chen, Y. J., Ning, J., Feng, Y., Grand, S. P., Niu, F., ... & Ni, J., 2015. High  
8  
9 resolution 3-D crustal structure beneath NE China from joint inversion of ambient  
10  
11 noise and receiver functions using NECESSArray data. *Earth and Planetary Science*  
12  
13 *Letters*, 416, 1-11.

14  
15  
16 Hacker, B.R. and G.A. Abers, Subduction Factory 3, 2004. An Excel worksheet and  
17  
18  
19 macro for calculating the densities, seismic wave speeds, and H<sub>2</sub>O contents of  
20  
21  
22 minerals and rocks at pressure and temperature. *Geochem. Geophys. Geodyn.* 5,  
23  
24  
25 Q01005, doi:10.1029/2003GC000614.

26  
27  
28 Hacker, B.R., Ritzwoller, M.H., Xie, J., 2014. Partially melted, mica-bearing crust in  
29  
30  
31 Central Tibet. *Tectonics*, 33, 2014TC003545.

32  
33  
34 Herrmann, R. B., Computer programs in seismology: An evolving tool for instruction and  
35  
36  
37 research, 2013. *Seism. Res. Lettr.* 84, 1081-1088, doi:10.1785/0220110096

38  
39  
40 Huang, H., Yao, H., & van der Hilst, R. D., 2010. Radial anisotropy in the crust of SE  
41  
42  
43 Tibet and SW China from ambient noise interferometry. *Geophysical Research*  
44  
45  
46 *Letters*, 37(21).

47  
48 Huang, Z., Su, W., Peng, Y., Zheng, Y., & Li, H., 2003. Rayleigh wave tomography of  
49  
50  
51 China and adjacent regions. *Journal of Geophysical Research: Solid Earth*  
52  
53  
54 (1978–2012), 108(B2).

55  
56 Huang, Z., Li, H., Zheng, Y., & Peng, Y., 2009. The lithosphere of North China Craton  
57  
58  
59  
60

1  
2  
3  
4 from surface wave tomography. *Earth and Planetary Science Letters*, 288(1),  
5  
6 164-173.  
7

8  
9 Jiang, C., Y. Yang, and Y. Zheng, 2014. Penetration of mid-crustal low velocity zone  
10  
11 across the Kunlun Fault in the NE Tibetan Plateau revealed by ambient noise  
12  
13 tomography. *Earth and Planetary Science Letters*, 406, 1-92.  
14  
15

16  
17 Jiang, M., S. Zhou, E. Sandvol, X. Chen, X. Liang, Y. John Chen, and W. Fan, 2011. 3-D  
18  
19 lithospheric structure beneath southern Tibet from Rayleigh-wave tomography with a  
20  
21 2-D seismic array, *Geophys. J. Int.*, 185, 593-608.  
22  
23  
24

25  
26 Kanamori, H., & Anderson, D. L., 1977. Importance of physical dispersion in surface  
27  
28 wave and free oscillation problems: Review. *Reviews of Geophysics*, 15(1), 105-112.  
29  
30

31  
32 Kang, D., W. Shen, J. Ning, and M.H. Ritzwoller, 2015. Crustal and uppermost mantle  
33  
34 structure beneath northeastern China from joint inversion of receiver functions,  
35  
36 Rayleigh wave dispersion, and Rayleigh wave ellipticity, in preparation.  
37  
38

39  
40 Karplus, M. S., S. L. Klemperer, J. F. Lawrence, W. Zhao, J. Mechie, F. Tilmann, E.  
41  
42 Sandvol, and J. Ni, 2013. Ambient-noise tomography of north Tibet limits geological  
43  
44 terrane signature to upper-middle crust, *Geophysical Research Letters*, 40(5),  
45  
46 808-813.  
47  
48

49  
50  
51 Kawakatsu, H., M. Yamamoto, S. Kaneshima, and T. Ohkura, 2011. Comment on “A  
52  
53 persistent localized microseismic source near the Kyushu Island, Japan” by  
54  
55 Xiangfang Zeng and Sidao Ni, *Geophys. Res. Lett.*, 38, L17307,  
56  
57  
58  
59  
60

1  
2  
3  
4 doi:10.1029/2011GL048584 .  
5  
6

7 Kennett, B.L.N. Engdahl, E.R. & Buland R., 1995. Constraints on seismic velocities in  
8 the Earth from travel times, *Geophys J. Int.*, 122, 108-124  
9

10  
11  
12  
13 Kind, R., Ni, J., Zhao, W., Wu, J., Yuan, X., Zhao, L., ... & Hearn, T., 1996. Evidence  
14 from earthquake data for a partially molten crustal layer in southern  
15 Tibet. *Science*, 274(5293), 1692-1694.  
16  
17  
18  
19

20  
21  
22 Kosarev, G., Kind, R., Sobolev, S. V., Yuan, X., Hanka, W., & Oreshin, S., 1999.  
23 Seismic evidence for a detached Indian lithospheric mantle beneath  
24 Tibet. *Science*, 283(5406), 1306-1309.  
25  
26  
27  
28  
29

30  
31 Legendre, C. P., Deschamps, F., Zhao, L., Lebedev, S., & Chen, Q. F., 2014. Anisotropic  
32 Rayleigh wave phase velocity maps of eastern China. *Journal of Geophysical*  
33 *Research: Solid Earth*, 119(6), 4802-4820.  
34  
35  
36  
37  
38

39 Li, H., W. Su, C.-Y. Wang, Z. Huang, 2009. Ambient noise Rayleigh wave tomography in  
40 western Sichuan and eastern Tibet, *Earth Planet. Sci. Lett.*, 282, 201-211.  
41  
42  
43  
44

45 Li, L., Li, A., Shen, Y., Sandvol, E. A., Shi, D., Li, H., & Li, X., 2013a. Shear wave  
46 structure in the northeastern Tibetan Plateau from Rayleigh wave  
47 tomography. *Journal of Geophysical Research: Solid Earth*, 118(8), 4170-4183.  
48  
49  
50  
51  
52

53 Li, Y., Wu, Q., Zhang, R., Tian, X., & Zeng, R., 2008. The crust and upper mantle  
54 structure beneath Yunnan from joint inversion of receiver functions and Rayleigh  
55  
56  
57  
58  
59  
60

1  
2  
3  
4 wave dispersion data. *Physics of the Earth and Planetary Interiors*, 170(1), 134-146.

5  
6  
7 Li, Y., Wu, Q., Pan, J., Zhang, F., & Yu, D., 2013b. An upper-mantle S-wave velocity  
8  
9 model for East Asia from Rayleigh wave tomography. *Earth and Planetary Science*  
10  
11 *Letters*, 377, 367-377.

12  
13  
14  
15  
16 Lin, F.-C., M.P. Moschetti, and M.H. Ritzwoller, Surface wave tomography of the  
17  
18 western United States from ambient seismic noise: Rayleigh and Love wave phase  
19  
20 velocity maps, *Geophys. J. Int.*, doi:10.1111/j1365-246X.2008.03720.x, 2008.

21  
22  
23  
24 Lin, F.-C., M.H. Ritzwoller, and R. Snieder, Eikonal Tomography: Surface wave  
25  
26 tomography by phase-front tracking across a regional broad-band seismic array,  
27  
28 *Geophys. J. Int.*, 177(3), 1091-1110, 2009.

29  
30  
31  
32  
33 Lin, F.-C., & Ritzwoller, M. H., 2011. Helmholtz surface wave tomography for isotropic  
34  
35 and azimuthally anisotropic structure. *Geophysical Journal International*, 186(3),  
36  
37 1104-1120.

38  
39  
40  
41 Lin, F.-C., Schmandt, B., & Tsai, V. C., 2012. Joint inversion of Rayleigh wave phase  
42  
43 velocity and ellipticity using USArray: Constraining velocity and density structure in  
44  
45 the upper crust. *Geophysical Research Letters*, 39(12).

46  
47  
48  
49 Lin, F.-C., Tsai, V. C., & Schmandt, B., 2014. 3-D crustal structure of the western United  
50  
51 States: application of Rayleigh-wave ellipticity extracted from noise  
52  
53 cross-correlations. *Geophysical Journal International*, ggu160.

1  
2  
3  
4 Liu, J., Han, J., & Fyfe, W. S., 2001. Cenozoic episodic volcanism and continental rifting  
5  
6 in northeast China and possible link to Japan Sea development as revealed from  
7  
8 K–Ar geochronology. *Tectonophysics*, 339(3), 385-401.  
9  
10

11  
12 Luo, Y., Xu, Y., Yang, Y., 2012. Crustal structure beneath the Dabie orogenic belt from  
13  
14 ambient noise tomography. *Earth and Planetary Science Letters*, 313–314, 12-22.  
15  
16

17  
18 Moschetti, M.P., M.H. Ritzwoller, F.C. Lin, and Y. Yang, 2010. Crustal shear velocity  
19  
20 structure of the western US inferred from ambient noise and earthquake data, *J.*  
21  
22 *Geophys. Res.*, 115, B10306, doi:10.1029/2010JB007448.  
23  
24

25  
26 Mosegaard, K., & Tarantola, A., 1995. Monte Carlo sampling of solutions to inverse  
27  
28 problems. *Journal of Geophysical Research: Solid Earth* (1978–2012),100(B7),  
29  
30 12431-12447.  
31  
32

33  
34 Niu, F., Li, J., 2011. Component azimuths of the CEArray stations estimated from P-wave  
35  
36 particle motion. *Earthquake Science*, 24(1), 3-13.  
37  
38

39  
40 Obrebski, Mathias, Richard M. Allen, Fengxue Zhang, Jiatie Pan, Qingju Wu, and  
41  
42 Shu-Huei Hung, 2012. Shear wave tomography of China using joint inversion of  
43  
44 body and surface wave constraints. *Journal of Geophysical Research: Solid Earth* 117,  
45  
46 no. B1.  
47  
48

49  
50 Rapine, R., F. Tilmann, M. West, J. Ni., and A. Rodgers, 2003. Crustal structure of  
51  
52 northern and southern Tibet from surface wave dispersion analysis, *J. Geophys. Res.*,  
53  
54 108, B2, doi:10.1029/2001JB000445.  
55  
56  
57  
58  
59  
60

- 1  
2  
3  
4 Ritzwoller, M.H. and A.L. Levshin, 1998. Eurasian surface wave tomography: Group  
5  
6 velocities, *J. Geophys. Res.*, 103, 4839 - 4878.  
7  
8  
9  
10 Ritzwoller, M.H., A.L. Levshin, L.I. Ratnikova, and A.A. Egorkin, 1998. Intermediate  
11  
12 period group velocity maps across Central Asia, Western China, and parts of the  
13  
14 Middle East, *Geophys. J. Int.*, 134, 315-328.  
15  
16  
17  
18 Ritzwoller, M.H., F.C. Lin, and W. Shen, Ambient noise tomography with a large seismic  
19  
20 array, *Compte Rendus Geoscience*, 13 pages, doi:10.1016/j.crte.2011.03.007, 2011.  
21  
22  
23  
24 Shapiro, N., Ritzwoller, M., 2002. Monte-Carlo inversion for a global shear-velocity  
25  
26 model of the crust and upper mantle. *Geophysical Journal International*, 151(1),  
27  
28 88-105.  
29  
30  
31  
32 Shapiro, N.M., M.H. Ritzwoller, P. Molnar, and V. Levin, 2004. Thinning and flow of  
33  
34 Tibetan crust constrained by seismic anisotropy, *Science*, 305, 233-236.  
35  
36  
37  
38 Shen, W., Ritzwoller, M.H., Schulte-Pelkum, V., Lin, F.-C., 2013a. Joint inversion of  
39  
40 surface wave dispersion and receiver functions: a Bayesian Monte-Carlo approach.  
41  
42 *Geophysical Journal International*, 192(2), 807-836.  
43  
44  
45  
46 Shen, W., Ritzwoller, M.H., Schulte-Pelkum, V., 2013b. A 3-D model of the crust and  
47  
48 uppermost mantle beneath the Central and Western US by joint inversion of receiver  
49  
50 functions and surface wave dispersion. *Journal of Geophysical Research - Solid*  
51  
52 *Earth*, 118(1), 262-276.  
53  
54  
55  
56 Sun, X., X. Song, S. Zheng, Y. Yang, M. Ritzwoller, 2013. Three dimensional shear  
57  
58  
59  
60

1  
2  
3  
4 velocity structure of the crust and upper mantle beneath China from ambient noise  
5  
6 surface wave tomography, *Earthquake Science*, 23, 449-463,  
7  
8  
9 doi:10.1007/s11589-010-0744-3.  
10

11  
12 Tang, Y., Chen, Y. J., Zhou, S., Ning, J., & Ding, Z., 2013. Lithosphere structure and  
13  
14 thickness beneath the North China Craton from joint inversion of ambient noise and  
15  
16 surface wave tomography. *Journal of Geophysical Research: Solid Earth*, 118(5),  
17  
18 2333-2346.  
19  
20

21  
22 Tang, Y., Obayashi, M., Niu, F., Grand, S. P., Chen, Y. J., Kawakatsu, H., ... & Ni, J. F.,  
23  
24 2014. Changbaishan volcanism in northeast China linked to subduction-induced  
25  
26 mantle upwelling. *Nature Geoscience*, 7(6), 470-475.  
27  
28

29  
30 Trabant, C., A. R. Hutko, M. Bahavar, R. Karstens, T. Ahern and R. Aster, 2012. Data  
31  
32 products at the IRIS DMC: stepping-stones for research and other application,  
33  
34  
35 Seismological Research Letters, 83(6), 846:854. doi:10.1785/0220120032.  
36  
37

38  
39 Villasenor, A., M.H. Ritzwoller, A.L. Levshin, M.P. Barmin, E.R. Engdahl, W. Spakman,  
40  
41 and J. Trampert, 2001. Shear velocity structure of Central Eurasia from inversion of  
42  
43 surface wave velocities, *Phys. Earth Planet. Int.*, 123(2-4), 169 - 184.  
44  
45

46  
47 Wang, W., Wu, J., Fang, L., Lai, G., Yang, T., & Cai, Y., 2014. S wave velocity structure  
48  
49 in southwest China from surface wave tomography and receiver functions. *Journal of*  
50  
51 *Geophysical Research: Solid Earth*, 119(2), 1061-1078  
52  
53

54  
55 Xie, J., Ritzwoller, M.H., Shen, W., Yang, Y., Zheng, Y., Zhou, L., 2013. Crustal radial  
56  
57 anisotropy across Eastern Tibet and the Western Yangtze Craton. *Journal of*  
58  
59

1  
2  
3  
4 *Geophysical Research: - Solid Earth*, 118(8), 4226-4252.

5  
6  
7 Yang, Y., et al., 2010. Rayleigh wave phase velocity maps of Tibet and the surrounding  
8  
9 regions from ambient seismic noise tomography, *Geochem., Geophys., Geosys.*,  
10  
11 11(8), Q08010, doi:10.1029/2010GC003119.

12  
13  
14 Yang, Y., Ritzwoller, M.H., Zheng, Y., Shen, W., Levshin, A.L., Xie, Z., 2012. A synoptic  
15  
16 view of the distribution and connectivity of the mid-crustal low velocity zone beneath  
17  
18 Tibet. *Journal of Geophysical Research - Solid Earth*, 117(B4), B04303.

19  
20  
21 Yao, H., van Der Hilst, R. D., & Maarten, V., 2006. Surface-wave array tomography in  
22  
23 SE Tibet from ambient seismic noise and two-station analysis—I. Phase velocity  
24  
25 maps. *Geophysical Journal International*, 166(2), 732-744.

26  
27  
28 Yao, H., C. Beghein, and R. D. van der Hist, 2008. Surface wave array tomography in SE  
29  
30 Tibet from ambient seismic noise and two-station analysis: II. Crustal and  
31  
32 upper-mantle structure, *Geophys. J. Int.*, 163, 205–219,  
33  
34 doi:10.1111/j.1365-246X.2007.03696.x.

35  
36  
37 Yao, H., R.D. van der Hilst, and J.-P. Montagner, 2010. Heterogeneity and anisotropy of  
38  
39 the lithosphere of SE Tibet from surface wave array tomography, *J. Geophys. Res.*,  
40  
41 115, B12307, doi:10.1029/2009JB007142.

42  
43  
44 Zeng, X, and S. Ni, 2010. A persistent localized microseismic source near the Kyushu  
45  
46 Island, Japan, *Geophys. Res. Lett.*, 37, L24307, doi:10.1029/2010GL045774.

47  
48  
49 Zeng, X, and S. Ni, 2011. Correction to “A persistent localized microseismic source near  
50  
51  
52  
53  
54  
55  
56  
57  
58  
59  
60

1  
2  
3  
4 the Kyushu Island, Japan". *Geophys. Res. Lett.*, 38, L16320,  
5  
6  
7 doi:10.1029/2011GL048822.  
8

9  
10 Zhang, X., Teng, J., Sun, R., Romanelli, F., Zhang, Z., & Panza, G. F., 2014. Structural  
11  
12 model of the lithosphere–asthenosphere system beneath the Qinghai–Tibet Plateau  
13  
14 and its adjacent areas. *Tectonophysics*, 634, 208-226.  
15  
16

17  
18 Zheng, S., X. Sun, X. Song, Y. Yang, and M. H. Ritzwoller, 2008. Surface wave  
19  
20 tomography of China from ambient seismic noise correlation, *Geochem. Geophys.*  
21  
22 *Geosyst.*, 9, Q0502, doi:10.1029/2008GC001981.  
23  
24  
25

26  
27 Zheng, X.F., Yao Z. X., Liang J. H. and Zheng J., 2010a. The role played and  
28  
29 opportunities provided by IGP DMC of China National Seismic Network in  
30  
31 Wenchuan earthquake disaster relief and researches. *Bull. Seismol. Soc. Am.*,  
32  
33 100(5B): 2866-2872, doi 10.1785/0120090257.  
34  
35  
36

37  
38 Zheng, Y., Yang, Y., Ritzwoller, M. H., Zheng, X., Xiong, X., & Li, Z., 2010b. Crustal  
39  
40 structure of the northeastern Tibetan plateau, the Ordos block and the Sichuan basin  
41  
42 from ambient noise tomography. *Earthquake Science*, 23(5), 465-476.  
43  
44  
45

46  
47 Zheng, Y., W. Shen, L. Zhou, Y. Yang, Z. Xie, and M.H. Ritzwoller, 2011. Crust and  
48  
49 uppermost mantle beneath the North China Craton, northeastern China, and the Sea of  
50  
51 Japan from ambient noise tomography, *J. Geophys. Res.*, 116, B12312,  
52  
53  
54 doi:10.1029/2011JB008637.  
55  
56

57  
58 Zhou, L., J. Xie, W. Shen, Y. Zheng, Y. Yang. H. Shi, and M.H. Ritzwoller, 2012. The  
59  
60

1  
2  
3  
4 structure of the crust and uppermost mantle beneath South China from ambient noise  
5  
6  
7 and earthquake tomography, *Geophys. J. Int.*, doi:  
8  
9  
10 10.1111/j.1365-246X.2012.05423.x.  
11  
12  
13  
14  
15  
16  
17  
18  
19  
20  
21  
22  
23  
24  
25  
26  
27  
28  
29  
30  
31  
32  
33  
34  
35  
36  
37  
38  
39  
40  
41  
42  
43  
44  
45  
46  
47  
48  
49  
50  
51  
52  
53  
54  
55  
56  
57  
58  
59  
60

## Tables

**Table 1.** Tectonic Zonation, Blocks, and Major Basins in the Region of Study. Letters and numbers are found in Fig. 1b.

Zones	Tectonic Blocks	Major Basins
<b>Xiyu (Northwestern China)</b>	Junggar Basin Block (A) Tianshan (B) Tarim Basin Block (C) Sayan Block (D) Altay Block (E) Alxa Block (F)	Junggar Basin (1) Tarim Basin (2) Turpan Basin (3)
<b>Tibetan Plateau and Nearby Areas</b>	Qilianshan Block (G) Qaidam Block (H) Songpan-Ganzi Terrane (I) Qiangtang Block (J) Lhasa Terrane (K) Chuandian Terrane (L)	Qaidam Basin (4) Qiangtang Tanggula Basin (5) Cuoqing Lunpola Basin (6) Qabdu Basin (7) Chuxiong Basin (8)
<b>Southeastern Tibet</b>	S. Yunnan Block (M) W. Yunnan Block (N)	Lanping-Simao Basin (9)
<b>South China</b>	Yangtze Craton (O) South China Block (P)	Sichuan Basin (10) Nanyang Basin (11) Jianghan Basin (12) East China Sea Basin (13) Pearl River Mouth Basin (14) Beibuwan Basin (15)
<b>North China Craton and nearby seas</b>	Ordos Block (Q) North China Plain (R) E. Shandong/Yellow Sea Block (S)	Jiuquan Minle Wuwei Basin (16) Ordos Basin (17) Bohaiwan Basin (18) Taikang Hefei Basin (19) Subei Yellow Sea Basin (20)
<b>Northeastern China, Korean Peninsula, and the Sea of Japan</b>	Yanshan Terrane (T) Xingan-East Mongolia Block (U) Northeast Asia (V) Ryuku Subduction Zone (W) G X g' A R g X) Lesser Xing'An Range (Y)	Songliao Basin (21) Temtsag Hailar Basin (22) Erlian Basin (23) Sea of Japan Backarc Basin (24) Tsushima Basin (25)

**Table 2.** Final Number of Unique Paths as a Function of Period for Ambient Noise

Period (s)	Core	Augmented <i>CEARRAY</i>	Augmented <i>NECESS, KSN,</i> <i>China Array</i>	After QC1	After QC2	After QC3	
						Group	Phase
8	92315	91941	65331	224094	122406	99929	114499
10	127245	112472	81066	287548	184928	152555	172225
12	156869	123942	86484	319786	216548	185235	204790
14	156869	130558	89208	336805	231378	204102	221233
16	161135	134248	89391	343788	235425	212290	227940
18	161967	135323	85868	342364	230270	219614	227007
20	163044	133706	81699	338802	221454	212329	218990
22	98561	179137	79429	320230	179442	174309	177860
24	96695	174961	72917	309201	159397	154435	157861
26	93388	169767	68914	298591	143236	138559	141719
28	88578	164688	66414	287980	130348	125423	128770
30	131409	124759	60631	286003	138505	129618	134885
32	82132	153480	54007	261458	98294	92793	96666
35	112923	119426	50316	256174	105888	96337	102213
40	94619	115613	39413	226512	73882	64766	70182
45	74622	113628	33868	201003	50919	43247	47379
50	52829	107542	23227	165167	27439	22574	25504

**Table 3.** Misfit as a Function of Period for Ambient Noise

Period (s)	Misfit (s)	
	Group	Phase
8	2.55	0.856
10	2.53	0.845
12	2.55	0.775
14	2.47	0.751
16	2.54	0.757
18	3.11	0.809
20	3.22	0.819
22	3.20	0.800
24	2.29	0.871
26	3.40	0.947
28	3.59	1.029
30	3.84	1.180
32	3.81	1.182
35	4.11	1.340
40	4.38	1.455
45	4.59	1.556
50	4.73	1.662

## Figure Captions

**Figure 1.** (a) Locations of the 2073 stations used in the current study: (black triangles) PASSCAL stations, KNET stations or F-Net stations in Japan, (red triangles) CEArray stations, (yellow triangles) China Array or Korean National Seismic Network stations, (blue triangles) NECESS array stations, and (white triangles) GSN or CDSN stations. The grey stars identify the three locations where we present data (Fig. 7), prior and posterior distributions (Figs. 14-16), and model envelopes (Fig. 17). (b) Tectonic features and major basins identified in Table 1. The north-south directed dashed line is the North-South Gravity Lineament and the large red triangles are the locations of Datong and Changbaishan volcanoes.

**Figure 2.** Locations of stations identified as problematic: (red triangles) mislocation error, (blue triangles)  $\pi$  phase error presumably a polarity error, (white triangles) locations differ from different data sources, and (black triangles) unknown perhaps time variable problem with instrument responses.

**Figure 3.** Examples of misfit histograms for the final data set: observed Rayleigh wave phase or group time minus predicted group or phase time (in sec) computed using straight ray theory from the estimated phase or group speed map. The standard deviation of each misfit distribution is presented in each panel. Top Row: phase speed measurements; Bottom Row: group speed measurements.

**Figure 4.** Comparison between the 20 sec Rayleigh wave isotropic phase speed maps

1  
2  
3  
4 constructed from ambient noise measurements using (a) eikonal tomography and (b) the  
5  
6 traditional ray theoretic tomography method of Barmin et al. (2001) in the region where  
7  
8 eikonal tomography performs well, presented as percent deviations from 3.42 km/s. (c)  
9  
10 The difference between these two maps: Barmin's method minus eikonal. (d) Histogram  
11  
12 of the differences between the maps, with the mean and standard deviation indicated.  
13  
14  
15  
16  
17

18 **Figure 5.** (a) and (b) Like **Figure 4**, but this is a comparison between eikonal tomography  
19  
20 and the method of Barmin et al. (2001) for azimuthal anisotropy, which is plotted so that  
21  
22 the length of each bar is proportional to the amplitude of azimuthal anisotropy (see inset  
23  
24 in each panel showing the length scale) and the direction of each bar points in the  
25  
26 fast-axis directions. (c) and (d) Histograms of the differences in the amplitude and  
27  
28 fast-axis direction between the two tomographic methods: Barmin's method minus  
29  
30 eikonal.  
31  
32  
33  
34  
35  
36

37 **Figure 6.** Comparison between the 40 sec Rayleigh wave isotropic phase speed maps  
38  
39 constructed from (a) earthquake based measurements interpreted through Helmholtz  
40  
41 tomography and (b) ambient noise measurements interpreted through the tomographic  
42  
43 method of Barmin et al. (2001). The earthquake results are based on NECESS data and  
44  
45 the location of the array is outlined in (a) and (b). (c) Difference between the results of  
46  
47 these two data sets and tomographic methods: earthquake minus ambient noise results.  
48  
49  
50  
51 (d) Histogram of the differences in (c), with statistics presented.  
52  
53  
54  
55

56 **Figure 7.** Examples of Rayleigh wave group and phase speed measurements presented as  
57  
58  
59  
60

1  
2  
3  
4 one standard deviation error bars for the three locations (a – Tibet, b – South China, c –  
5  
6  
7 Northeast China) identified by stars in Fig. 1. Solid curves are computed from the mean  
8  
9  
10 of each posterior distribution at each location (red lines – phase speed, blue lines – group  
11  
12 speeds), which is shown in Fig. 17. For the location in Tibet, two curves are plotted:  
13  
14 dashed line, Model A – crustal monotonicity constraint; solid line, Model B – no  
15  
16 monotonicity constraint. Misfits, defined by eqn. (2), are labeled in each panel. The larger  
17  
18 Misfit on the Tibet panel is for the model with the crustal monotonicity constraint and the  
19  
20 other is for the model without this constraint.  
21  
22  
23  
24  
25

26 **Figure 8.** Examples of path density and resolution maps. (a) Path density estimated for  
27  
28 the 20 sec Rayleigh wave phase speed map in units of the number of paths contained in  
29  
30 each  $2^\circ$  square cell ( $\sim 50,000 \text{ km}^2$ ). (b) Estimated resolution for the 20 sec Rayleigh wave  
31  
32 phase speed map, where resolution is defined as twice the standard deviation of the 2D  
33  
34 Gaussian fit to the resolution surface at each grid node.  
35  
36  
37  
38  
39

40 **Figure 9.** Estimated one standard deviations uncertainties of Rayleigh wave phase speed  
41  
42 at periods of (a) 10 sec, (2) 30 sec, (3) 40 sec, and (4) 60 sec. At 60 sec period,  
43  
44 measurements are from earthquakes alone and the map identifies the area where  
45  
46 earthquake measurements exist. At 10 and 30 sec period, uncertainties derive from  
47  
48 ambient noise data alone and at 40 sec period uncertainties equally weight contributions  
49  
50 from ambient noise and earthquake data.  
51  
52  
53  
54  
55

56 **Figure 10.** (a) and (b) Similar to Fig. 9, but uncertainties here are for Rayleigh wave  
57  
58  
59  
60

1  
2  
3  
4 group speeds at 10 sec and 30 sec period, from ambient noise tomography (ANT) alone.

5  
6  
7 (c) Rayleigh wave group and phase speed uncertainties averaged across the study region  
8  
9 are presented as a function of period. Above 30 sec period, phase speed uncertainties are  
10  
11 for ambient noise and earthquake (ET) tomography are presented separately, where  
12  
13 ambient noise uncertainties are averaged across the entire region of study and earthquake  
14  
15 uncertainties are averaged only where such measurements exist (cf. [Fig. 9d](#)).  
16  
17  
18  
19

20  
21 **Figure 11.** Estimated Rayleigh wave phase speed maps at a selection of periods  
22  
23 presented as percent perturbations relative to the mean labeled on each map. At 30 sec  
24  
25 period and below, maps derive from ambient noise data alone, at 70 sec period the map  
26  
27 derives from earthquake data alone, at 50 sec period the map derives from earthquake  
28  
29 data where they exist and ambient noise elsewhere, and at 40 sec period the map derives  
30  
31 from both ambient noise and earthquake data weighted equally where both data sets exist.  
32  
33  
34  
35  
36  
37 The over-plotted tectonic features and basins are identified in [Fig. 1b](#) and [Table 1](#).  
38  
39

40  
41 **Figure 12.** Similar to Fig. 11, but Rayleigh wave group speed maps are presented at the  
42  
43 indicated periods and all maps are derived from ambient noise.  
44

45  
46 **Figure 13.** Estimates of azimuthal anisotropy for Rayleigh wave phase speeds at 10, 20,  
47  
48 and 30 sec period, determined using ambient noise data. The regions where azimuthal  
49  
50 anisotropy estimates are considered reliable are outlined with the black lines where path  
51  
52 density is greater than 1000 paths per 2° square cell (cf. [Fig. 8a](#)).  
53  
54  
55

56  
57 **Figure 14.** Examples of the prior and posterior distributions for several model variables  
58  
59  
60

1  
2  
3  
4 at the location in South China identified by a star in Fig. 1a, where the prior is shown  
5  
6 with the white histogram and the posterior by the red histogram. (a) Sedimentary  
7  
8 thickness, in km. (b) Crustal thickness, in km. (c) Jump across Moho: Vs (4 km below  
9  
10 Moho) – Vs (4 km above Moho), in km/s. (d) Vs at 15 km, in km/s. (e) Vs 4 km above  
11  
12 Moho, in km/s. (f) vs at 100 km, in km/s. The mean and standard deviation of both prior  
13  
14 and posterior distributions are labeled on each panel, where the standard deviation  
15  
16 appears in parentheses.  
17  
18  
19  
20  
21

22  
23 **Figure 15.** Similar to Fig. 13, but for the location in Northeast China identified by a star  
24  
25 in Fig. 1a.  
26  
27

28  
29 **Figure 16.** Similar to Figs. 13 and 14, but for the location in Tibet identified by a star in  
30  
31 Fig. 1a.  
32  
33

34  
35 **Figure 17.** Vertical envelope (grey shaded region) formed by the full set of accepted  
36  
37 models in the posterior distribution for the same three locations for which dispersion  
38  
39 measurements are shown in Fig. 7, identified by stars in Fig. 1a. The black lines identify  
40  
41 the mean of each distribution (from which the solid curves in Fig. 7 are computed) and  
42  
43 the red lines identify the one standard deviation perturbations in the posterior  
44  
45 distributions.  
46  
47  
48  
49

50  
51 **Figure 18.** (a) Total Misfit, defined by eqn. (2), to the observed Rayleigh wave phase and  
52  
53 group speed curves by the curves computed from the mean of the posterior distribution at  
54  
55 each point. (Misfit is defined as the square root of the reduced  $\chi^2$  value.) (b) Histogram of  
56  
57  
58  
59  
60

1  
2  
3  
4 Total Misfit. Average Misfit is about 0.9.  
5  
6

7 **Figure 19.** The estimated Vs model and uncertainties at three depths: (a,b) 3 km, (c,d) 20  
8 km, and (e,f) 40 km. The model and its uncertainty are the mean and standard deviation,  
9 respectively, of the posterior distribution averaged within  $\pm 3$  km of each depth. The  
10 model and its standard deviation are presented in km/s.  
11  
12  
13  
14  
15  
16

17  
18 **Figure 20.** Similar to [Fig. 19](#), but at three different depths: 60 km, 80 km, and 120 km.  
19  
20

21 **Figure 21.** Estimated (a) crustal thickness and (b) its uncertainty, where crustal thickness  
22 is the mean of the posterior distribution at each location and uncertainty is its standard  
23 deviation, both presented in km.  
24  
25  
26  
27  
28

29  
30 **Figure 22.** Blow up of the Vs model at 80 km depth ([Fig. 21c](#)), showing locations of the  
31 vertical transects displayed in [Fig. 23](#) and highlighting two anomalies: the so-called  
32 horseshoe-shaped anomaly (small green oval) and the Y-shaped anomaly (large green  
33 oval).  
34  
35  
36  
37  
38  
39

40  
41 **Figure 23.** Vertical transects running along the four profiles (A-A', B-B', C-C', D-D')  
42 identified in [Fig. 22](#). Crustal velocities are presented in km/s and mantle velocities are  
43 expressed as the perturbation to 4.4 km/s presented in percent. The locations of  
44 geological and tectonic features are identified above each transect along with surface  
45 topography. Transects are vertically exaggerated but horizontal distances are the same  
46 between them.  
47  
48  
49  
50  
51  
52  
53  
54  
55  
56  
57  
58  
59  
60

Figure 1

1  
2  
3  
4  
5  
6  
7  
8  
9  
10  
11  
12  
13  
14  
15  
16  
17  
18  
19  
20  
21  
22  
23  
24  
25  
26  
27  
28  
29  
30  
31  
32  
33  
34  
35  
36  
37  
38  
39  
40  
41  
42  
43  
44  
45  
46  
47  
48  
49  
50  
51  
52  
53  
54  
55  
56  
57  
58  
59  
60

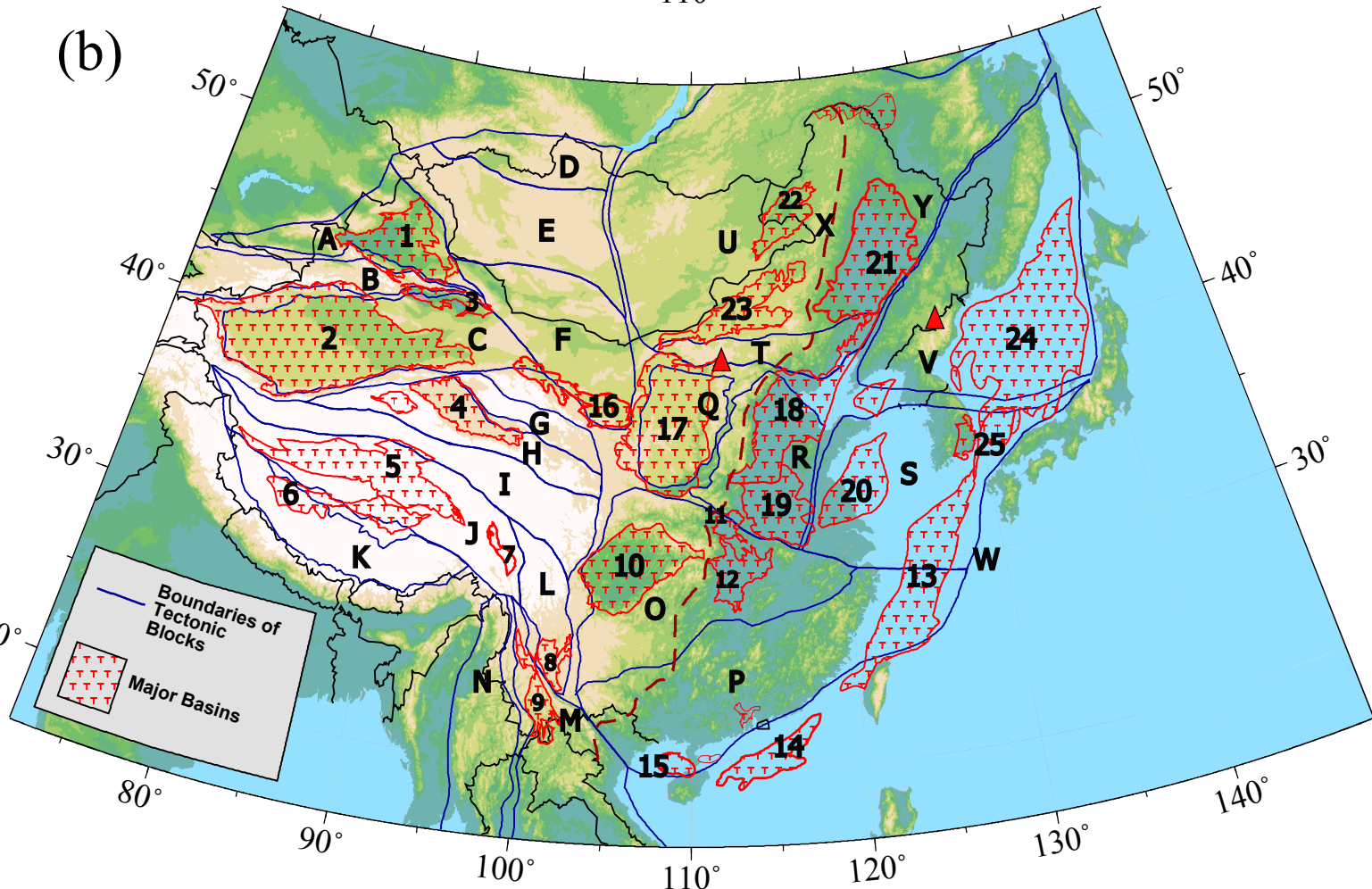
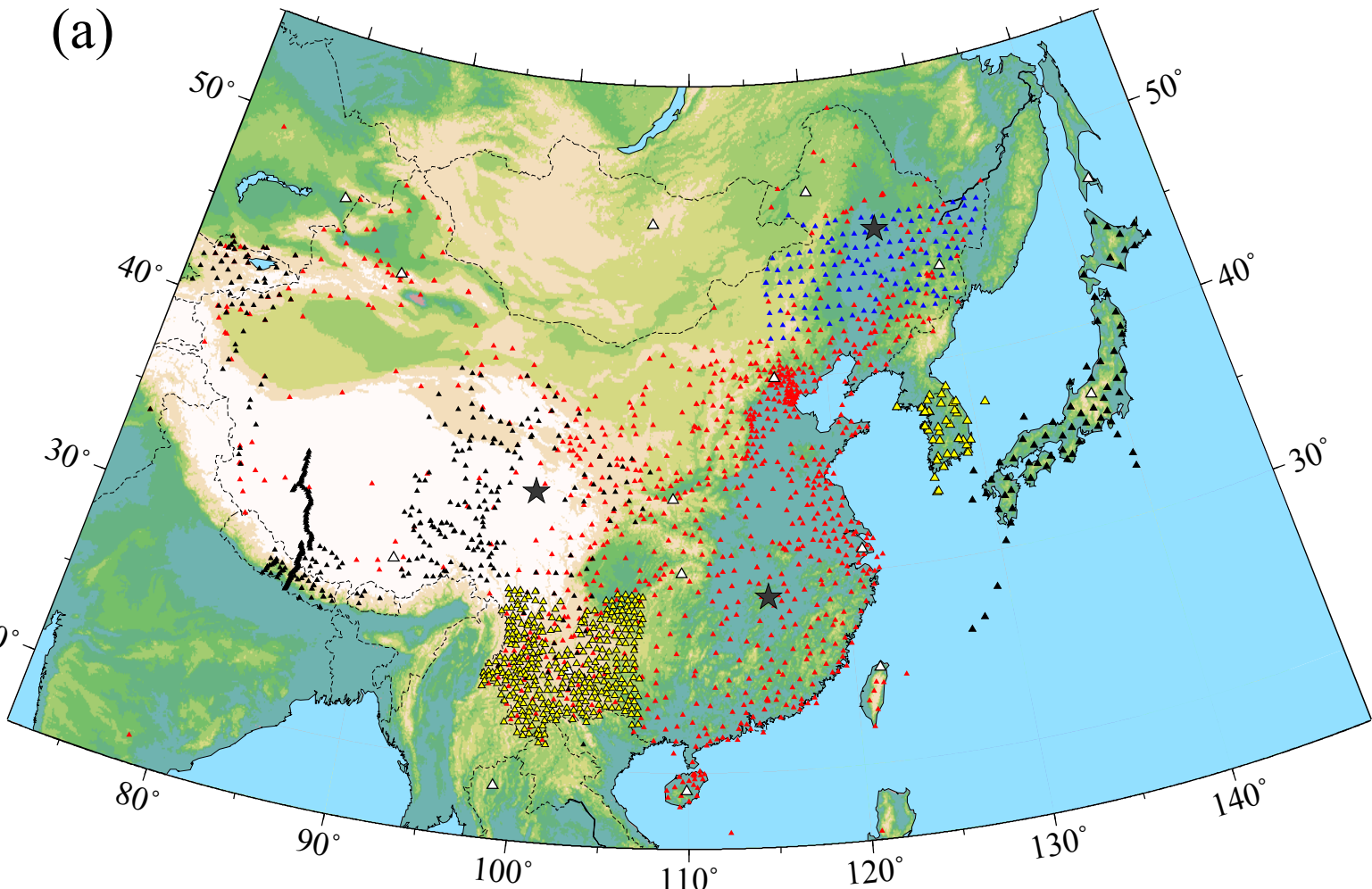
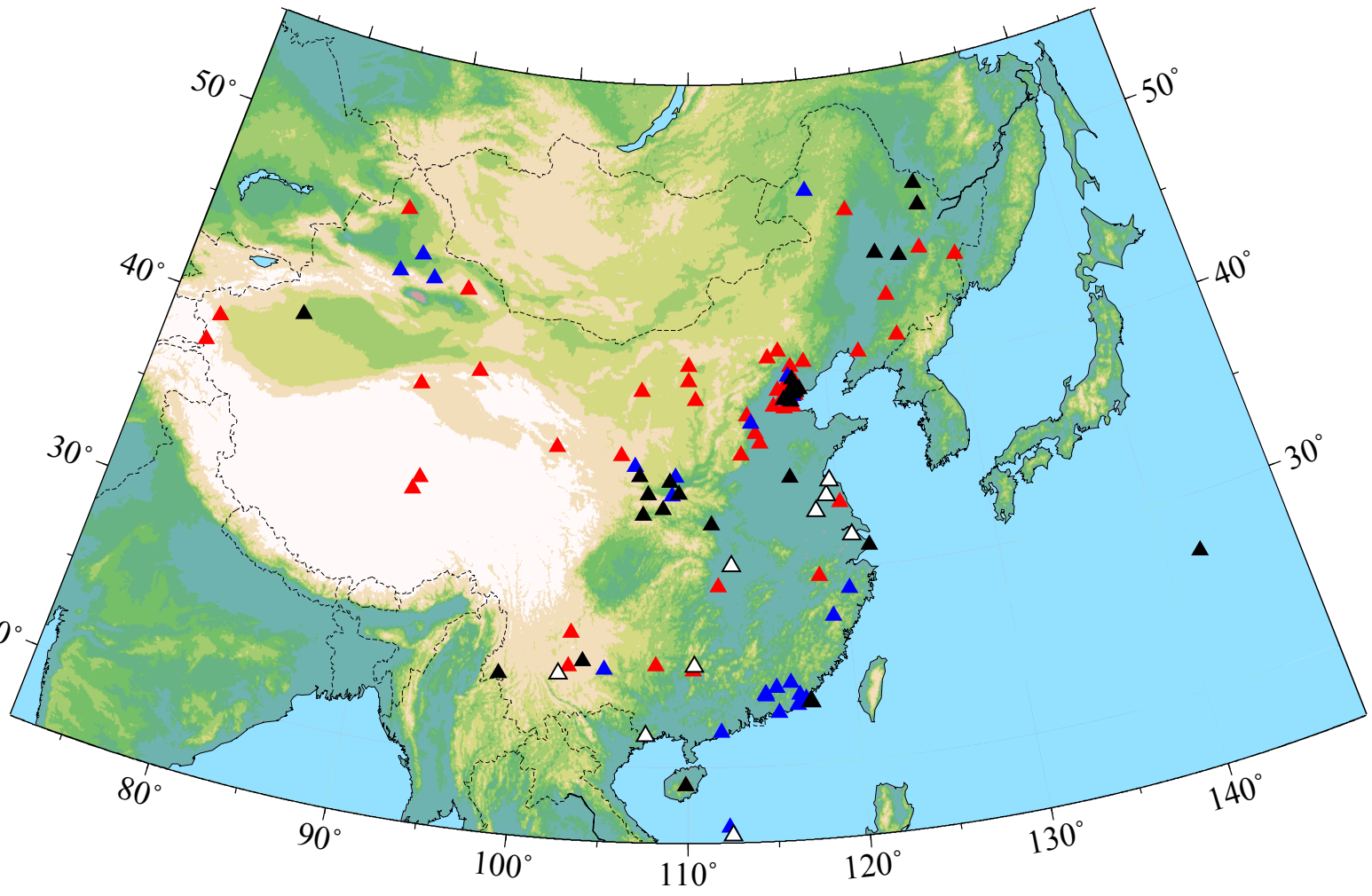
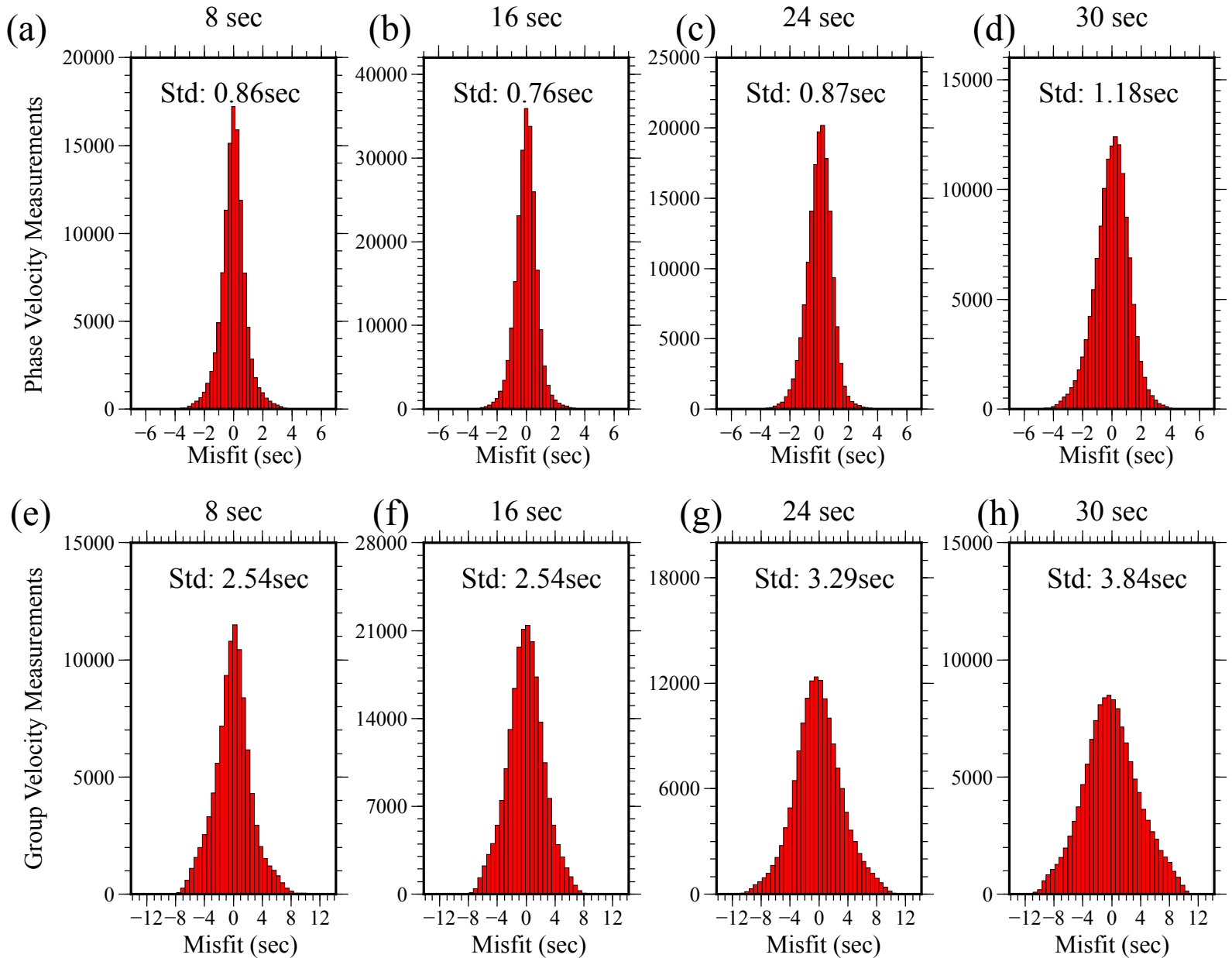


Figure 2

1  
2  
3  
4  
5  
6  
7  
8  
9  
10  
11  
12  
13  
14  
15  
16  
17  
18  
19  
20  
21  
22  
23  
24  
25  
26  
27  
28  
29  
30  
31  
32  
33  
34  
35  
36





1  
2  
3  
4  
5  
6  
7  
8  
9  
10  
11  
12  
13  
14  
15  
16  
17  
18  
19  
20  
21  
22  
23  
24  
25  
26  
27  
28  
29  
30  
31  
32  
33  
34  
35  
36  
37  
38  
39  
40

1  
2  
3  
4  
5  
6  
7  
8  
9  
10  
11  
12  
13  
14  
15  
16  
17  
18  
19  
20  
21  
22  
23  
24  
25  
26  
27  
28  
29  
30  
31  
32  
33  
34  
35  
36  
37  
38  
39  
40  
41  
42  
43  
44  
45  
46

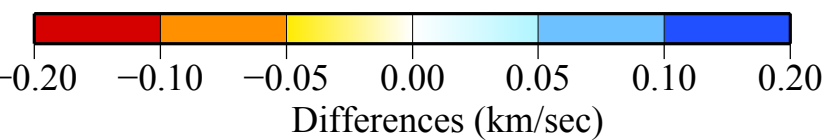
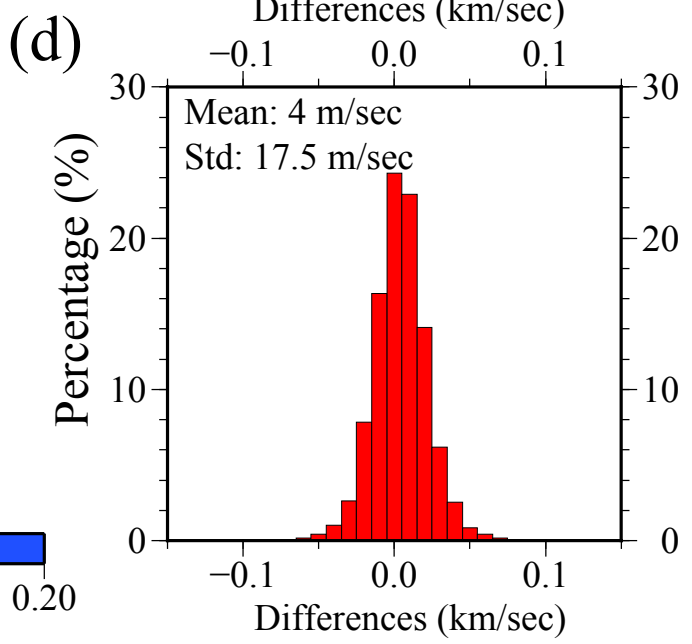
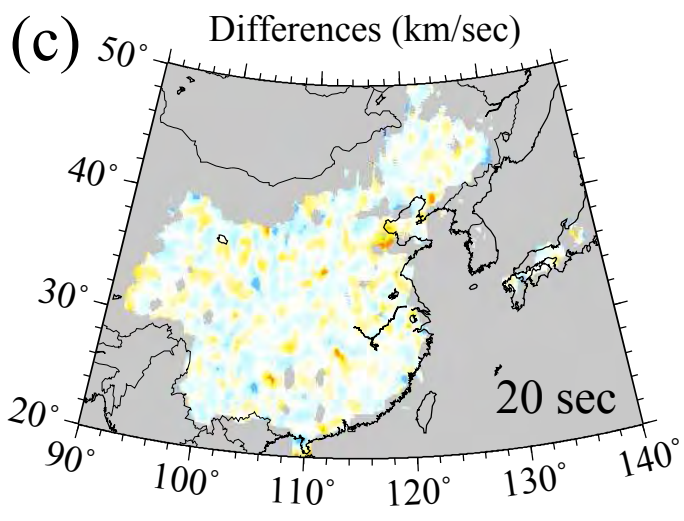
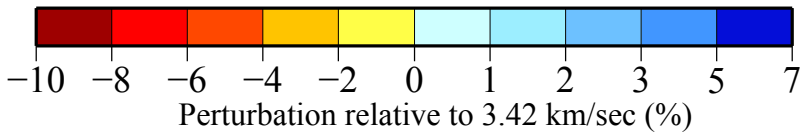
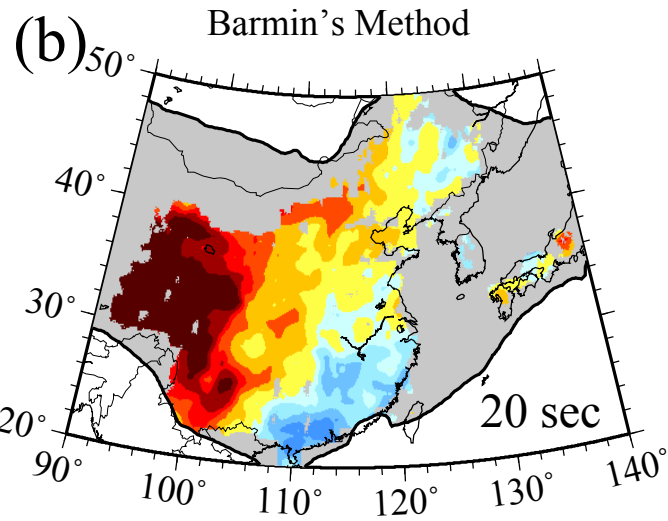
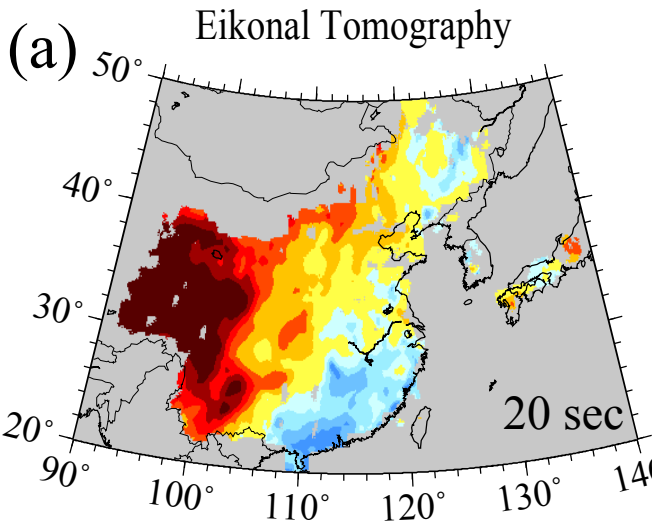
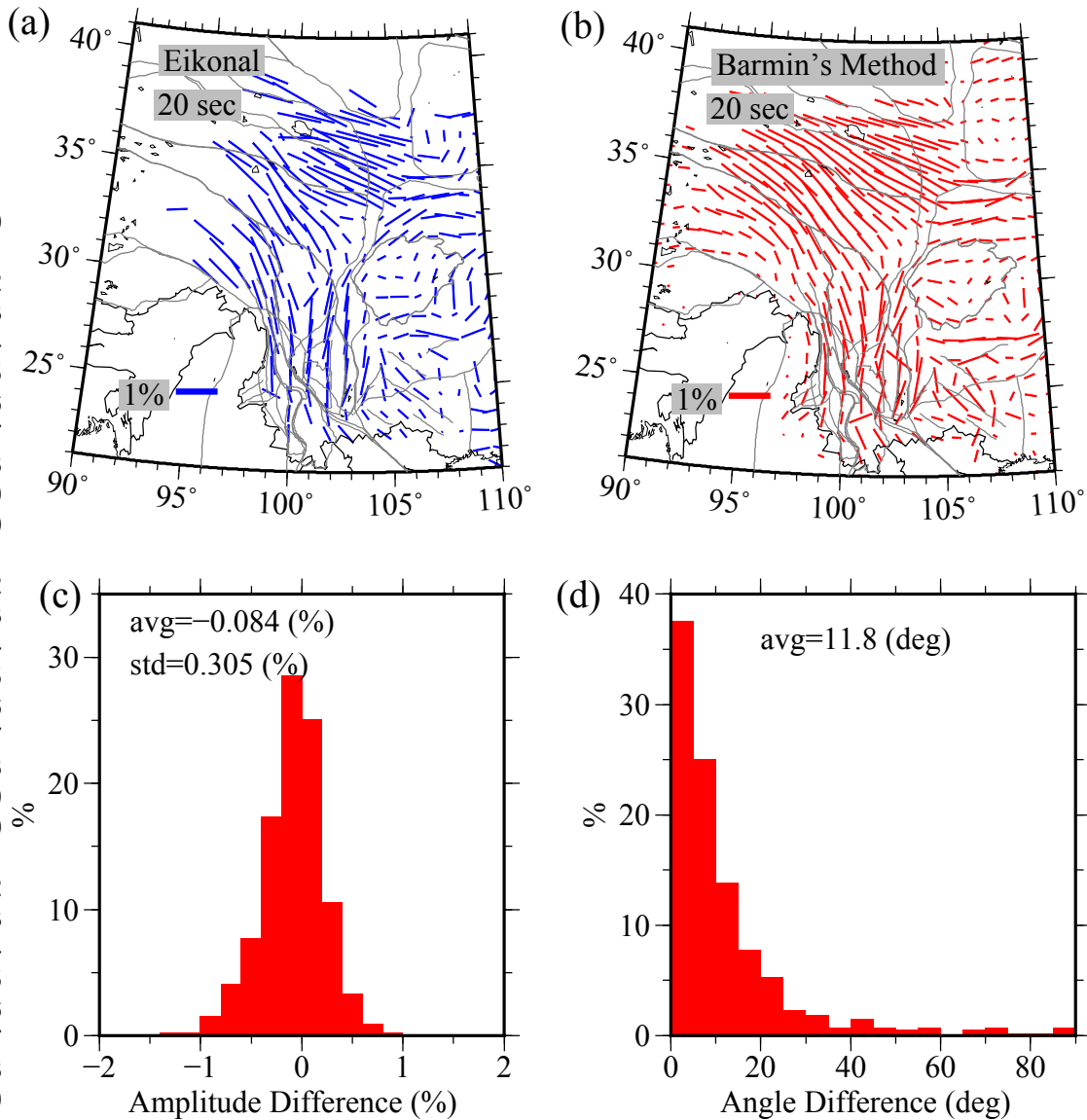


Figure 5



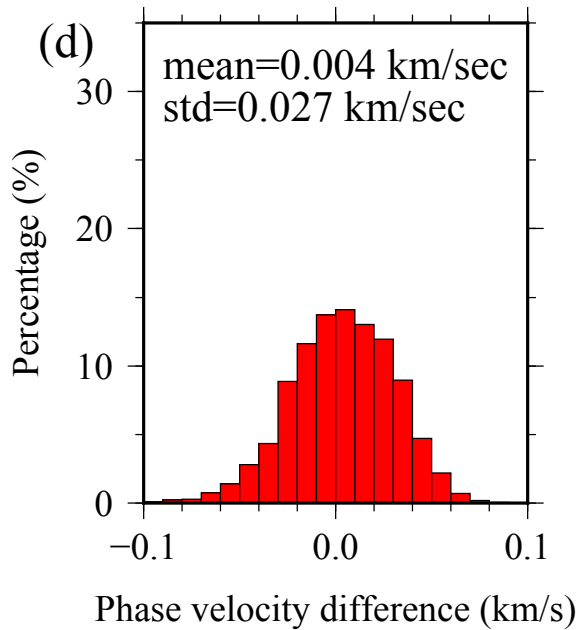
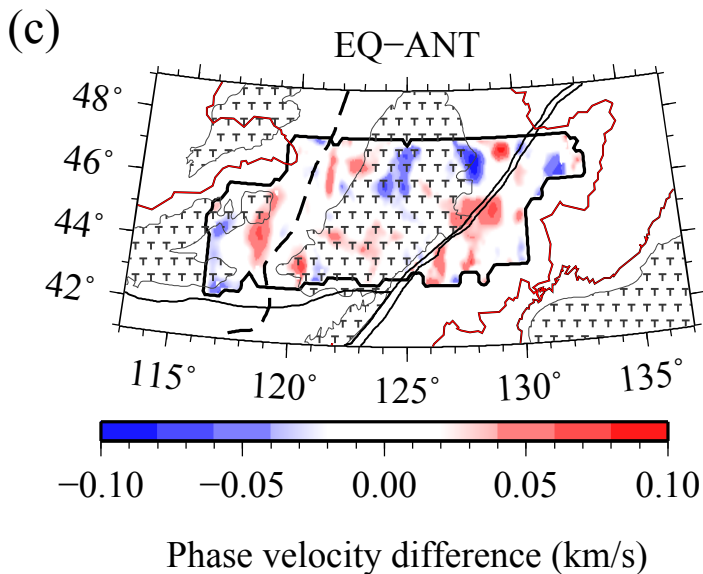
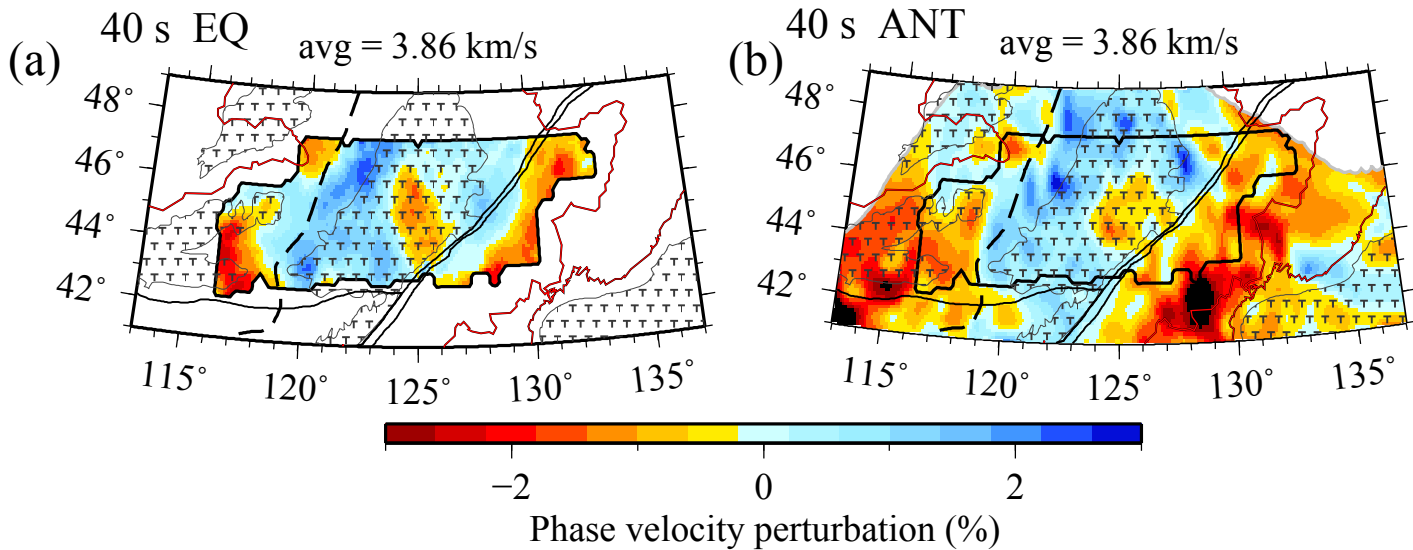


Figure 7

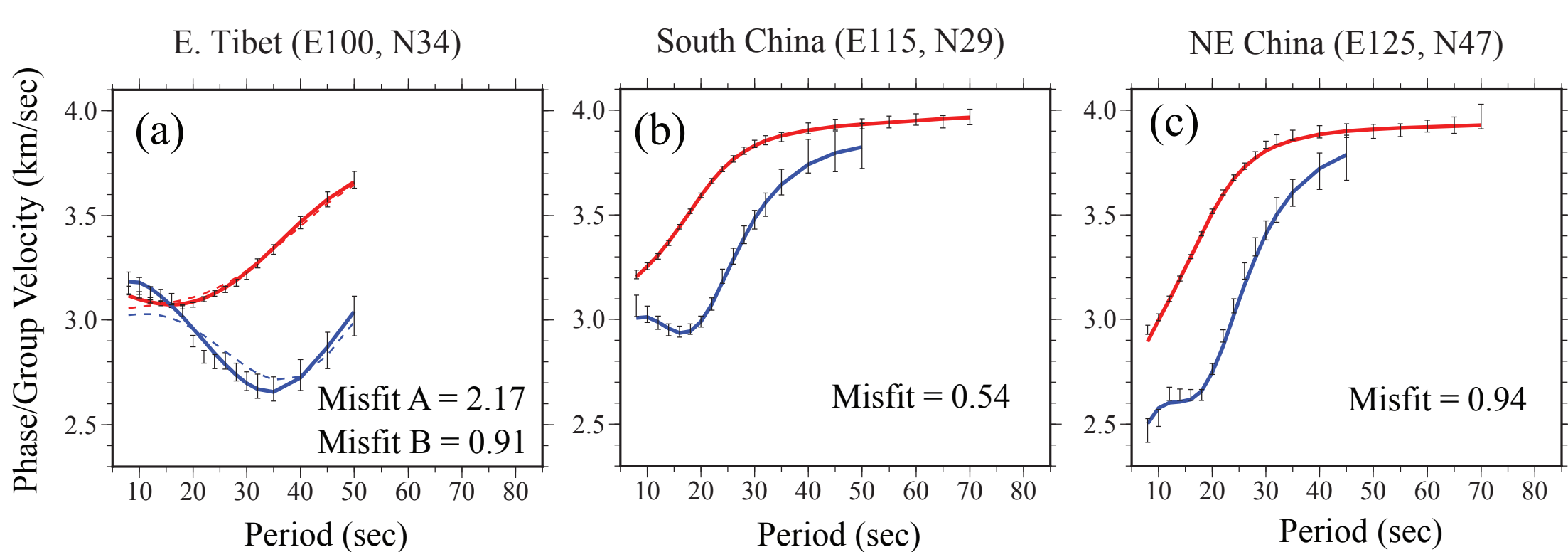


Figure 8

1  
2  
3  
4  
5  
6  
7  
8  
9  
10  
11  
12  
13  
14  
15  
16  
17  
18  
19  
20  
21  
22  
23  
24  
25  
26  
27  
28  
29  
30  
31  
32  
33  
34  
35  
36  
37  
38  
39

### Path Density

### Resolution

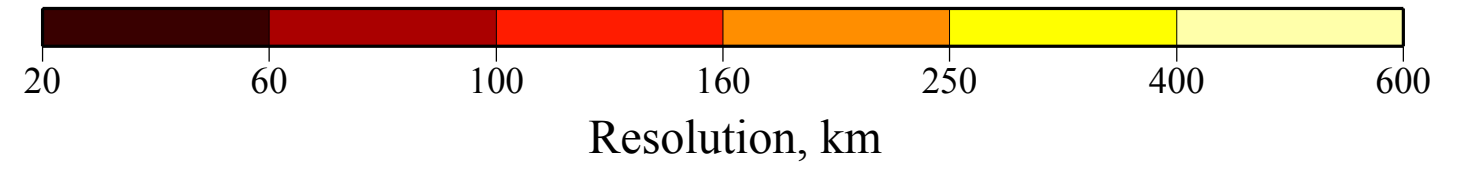
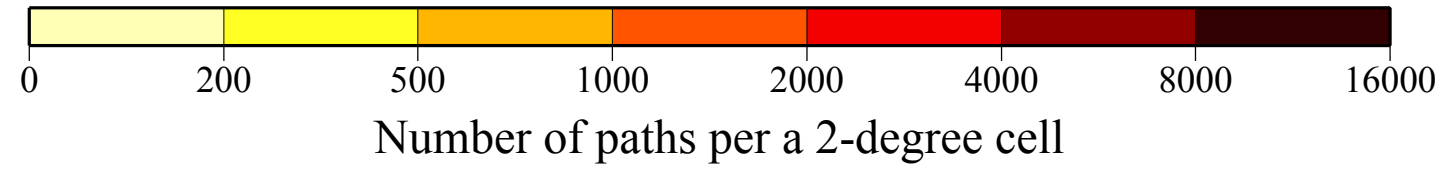
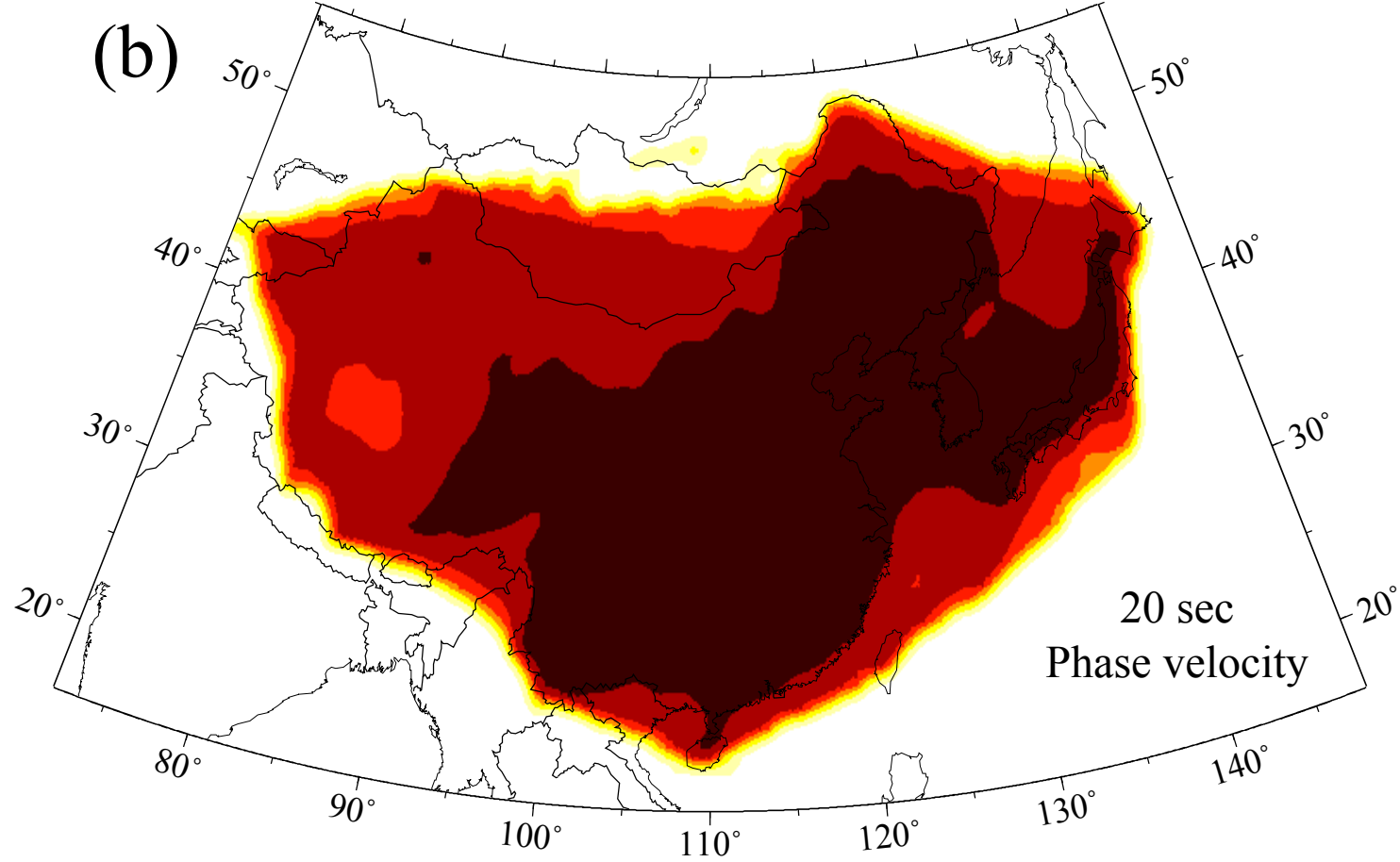
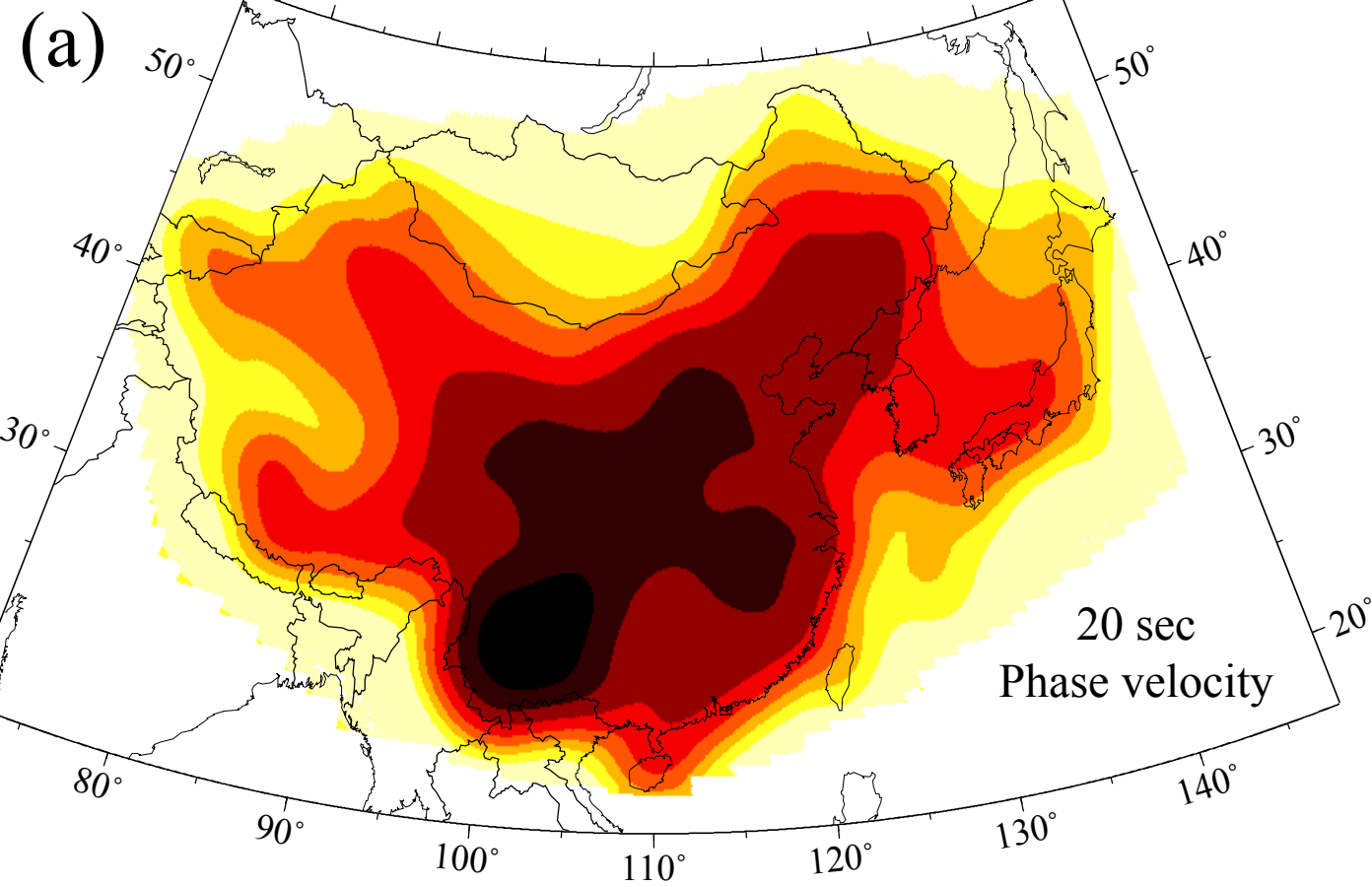
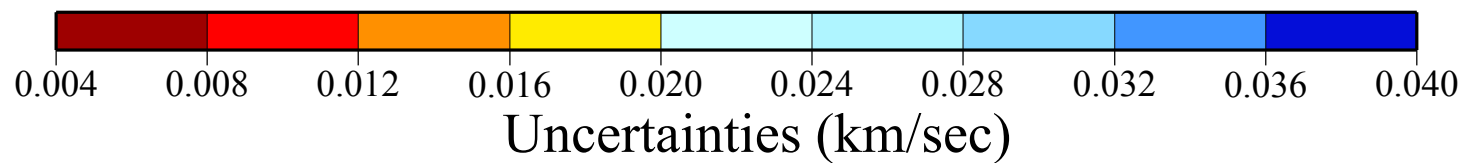
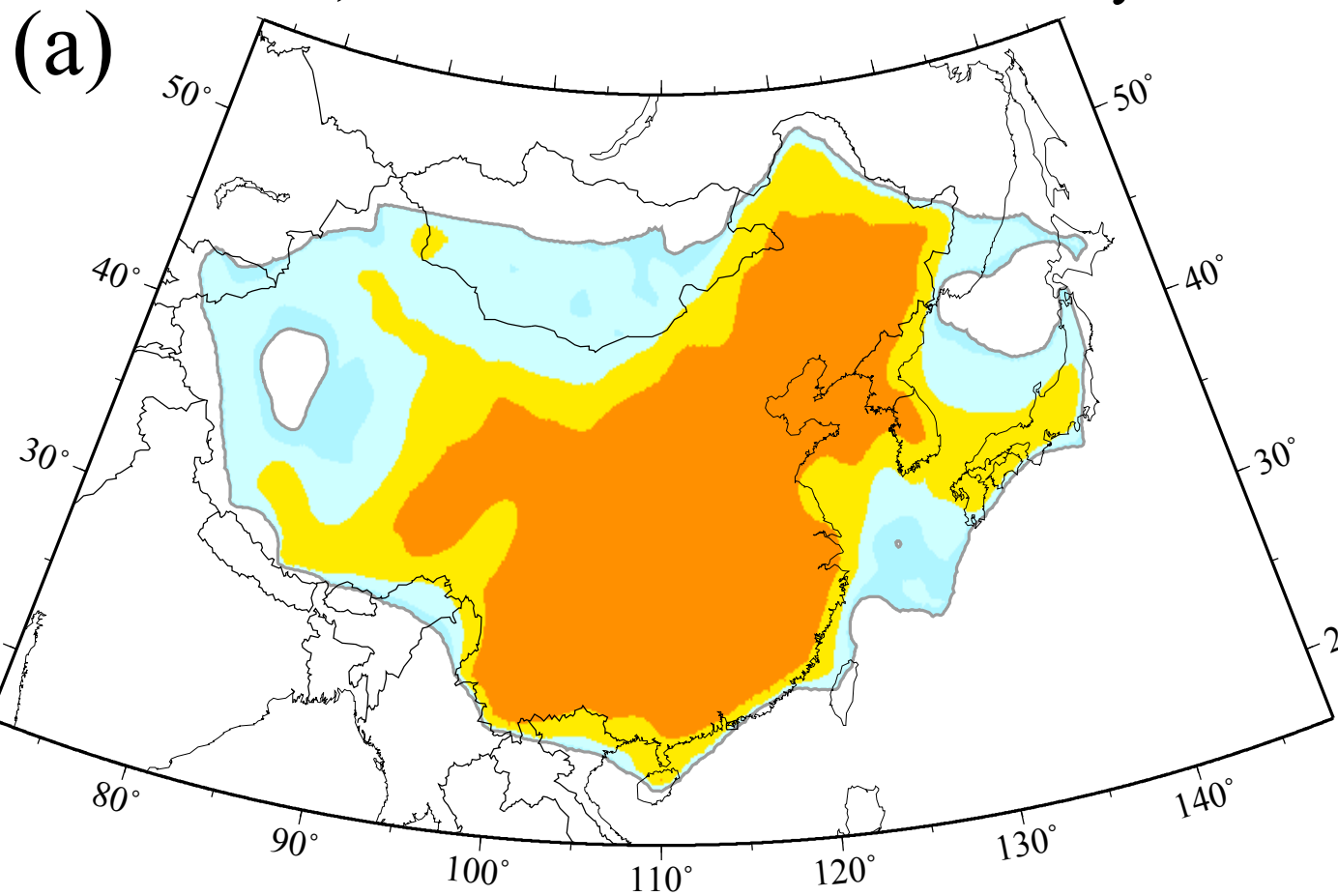


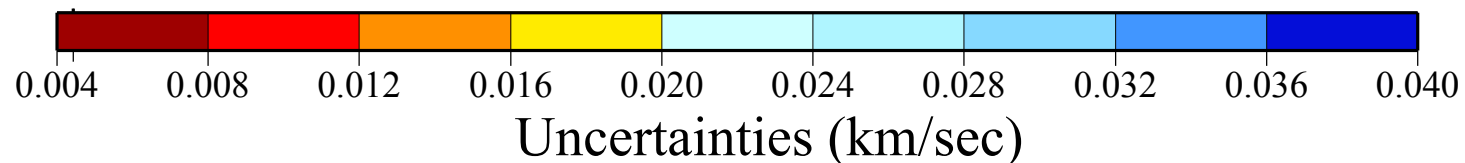
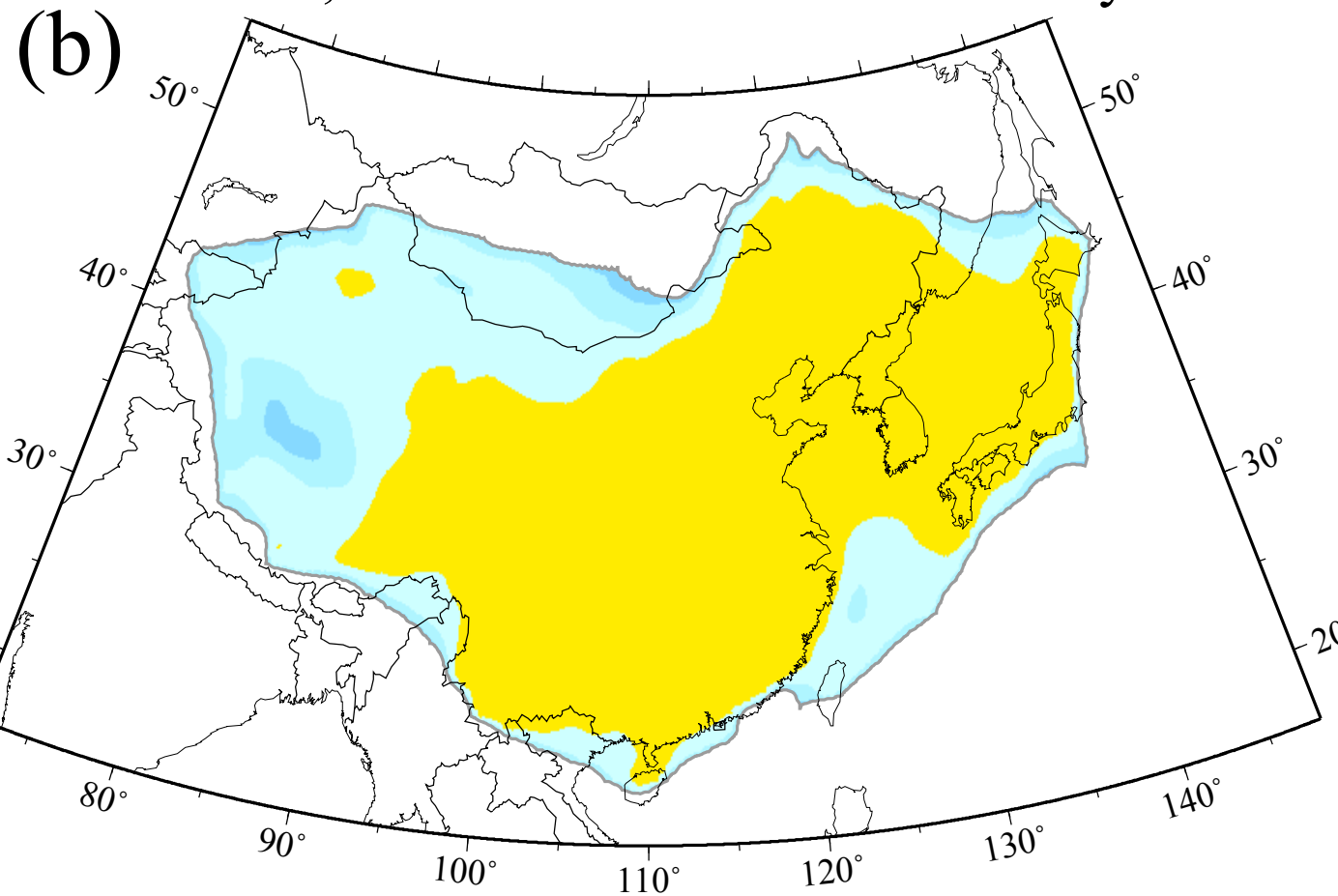
Figure 9

1  
2  
3  
4  
5  
6  
7  
8  
9  
10  
11  
12  
13  
14  
15  
16  
17  
18  
19  
20  
21  
22  
23  
24  
25  
26  
27  
28  
29  
30  
31  
32  
33  
34  
35  
36  
37  
38  
39  
40  
41  
42  
43  
44  
45  
46  
47  
48  
49  
50  
51  
52  
53  
54  
55  
56  
57  
58  
59  
60

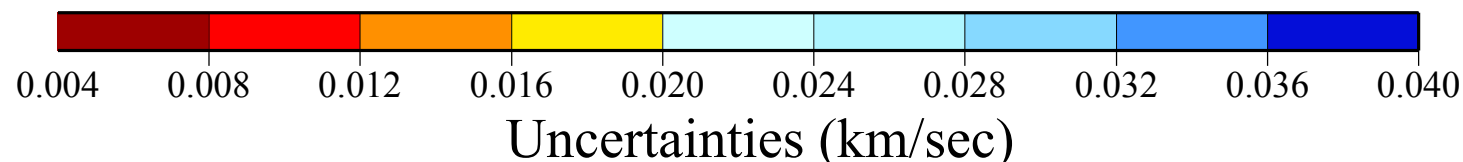
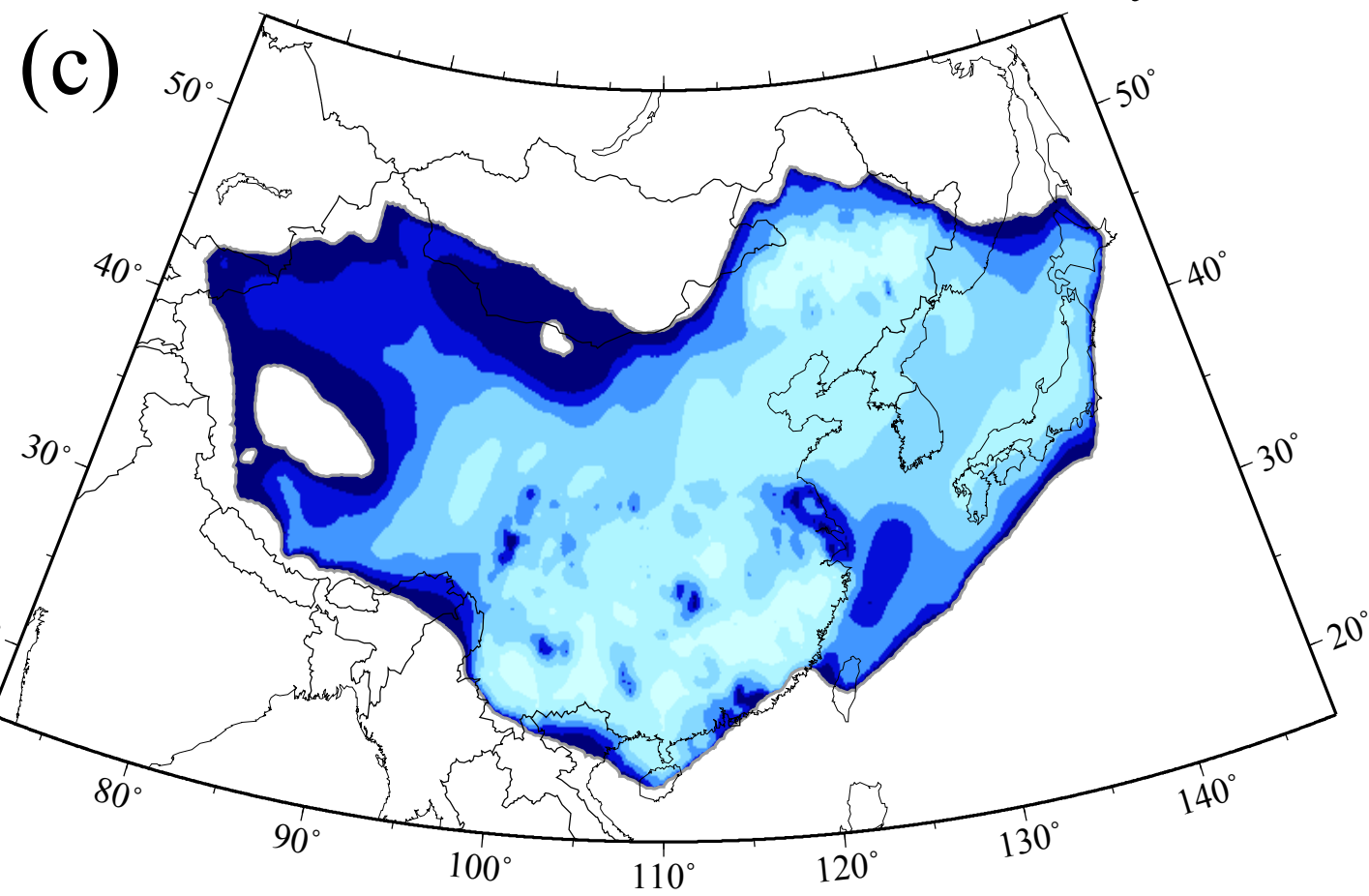
10 sec, Uncertainties of Phase Velocity



30 sec, Uncertainties of Phase Velocity



40 sec, Uncertainties of Phase Velocity



60 sec, Uncertainties of Phase Velocity

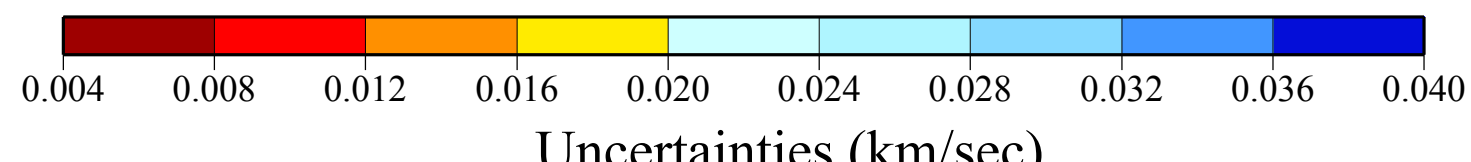
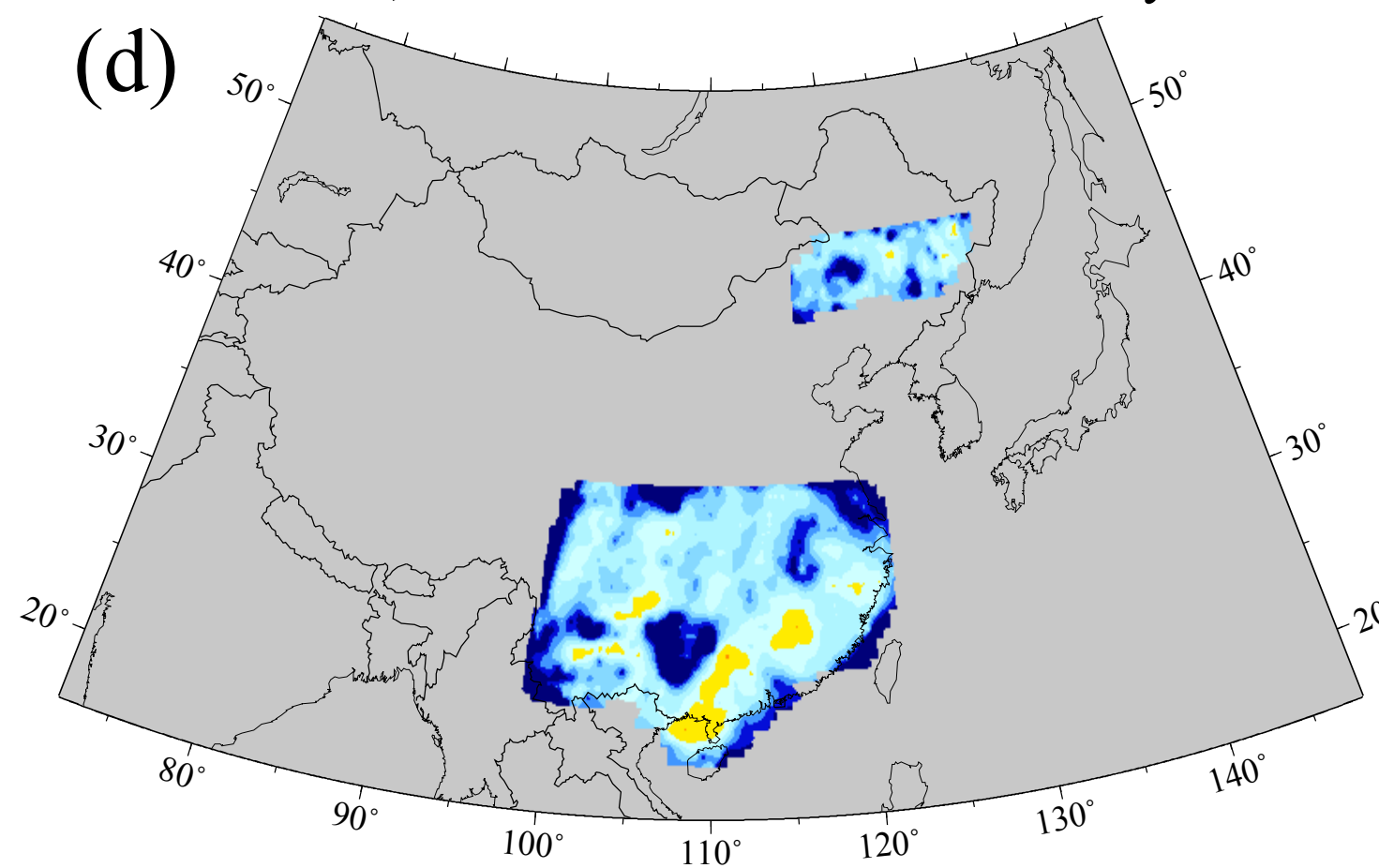


# Figure 10

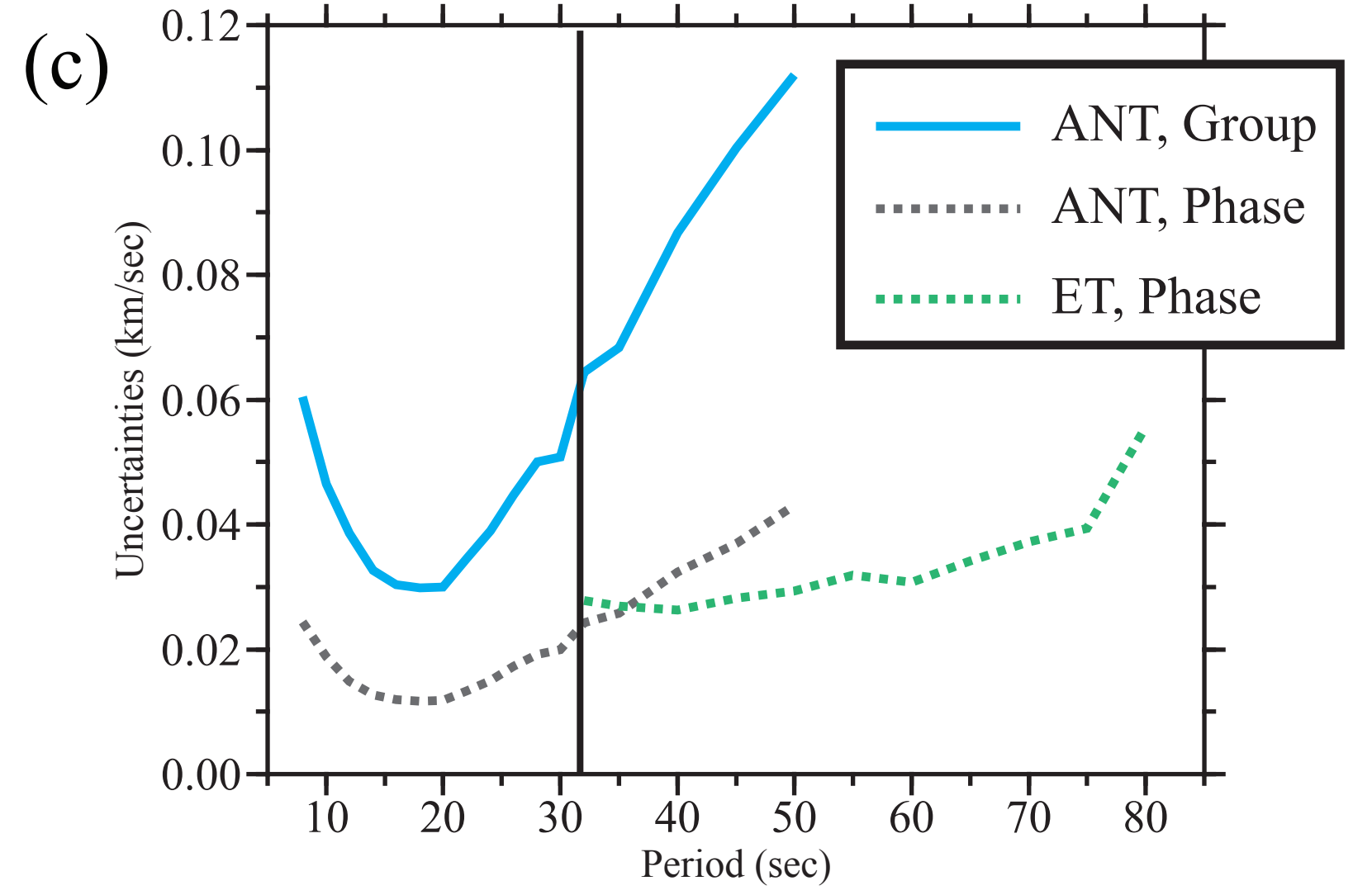
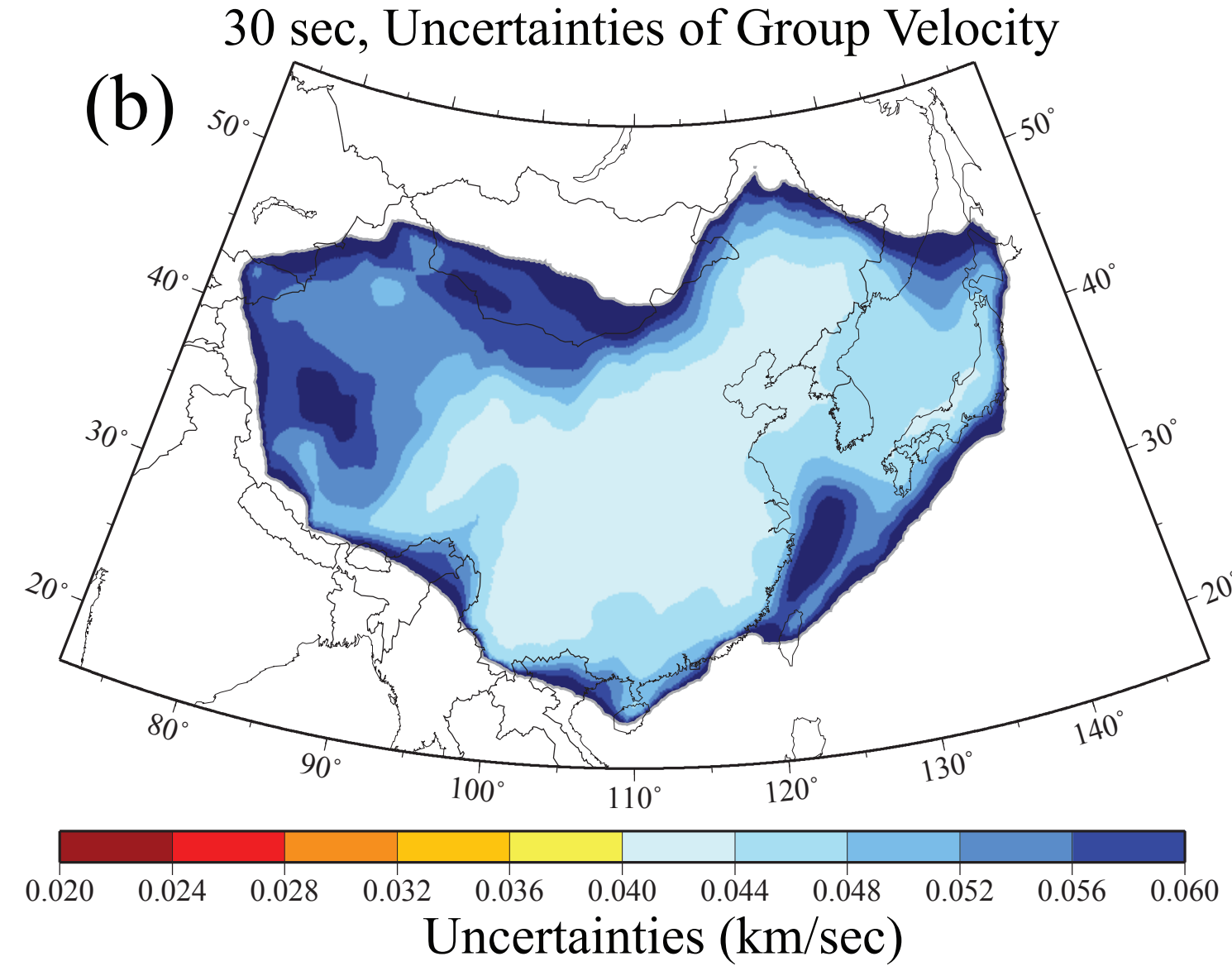
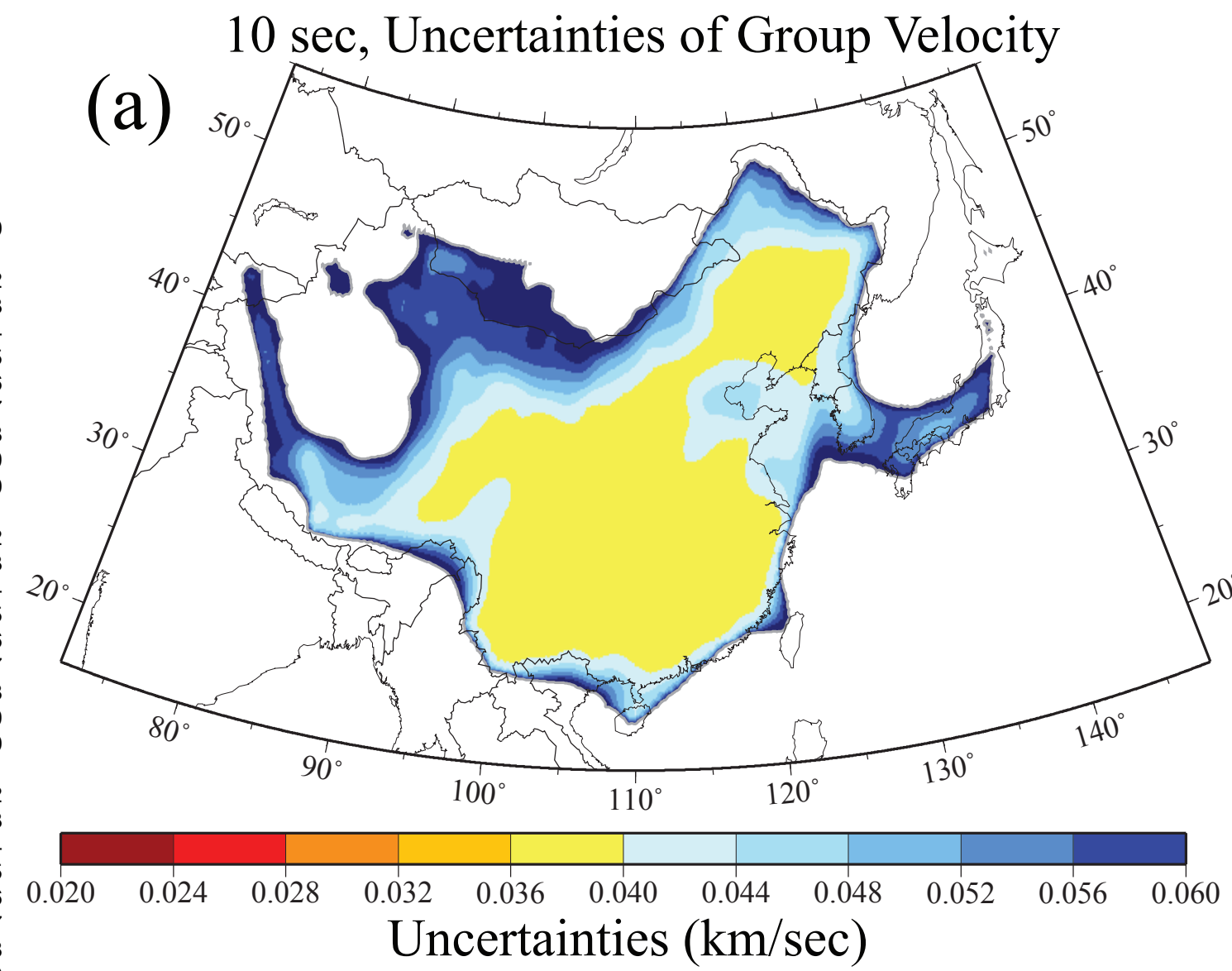
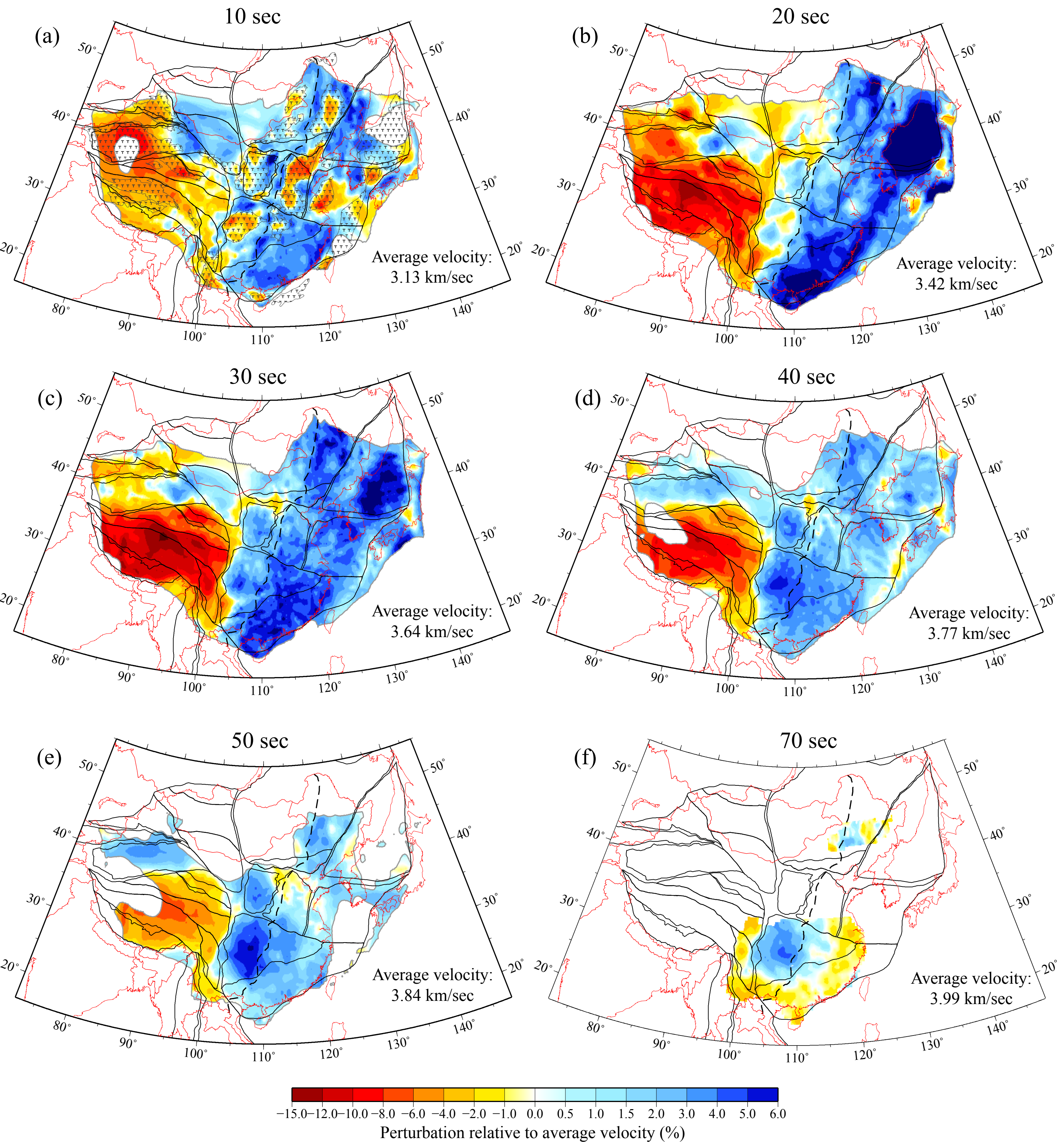


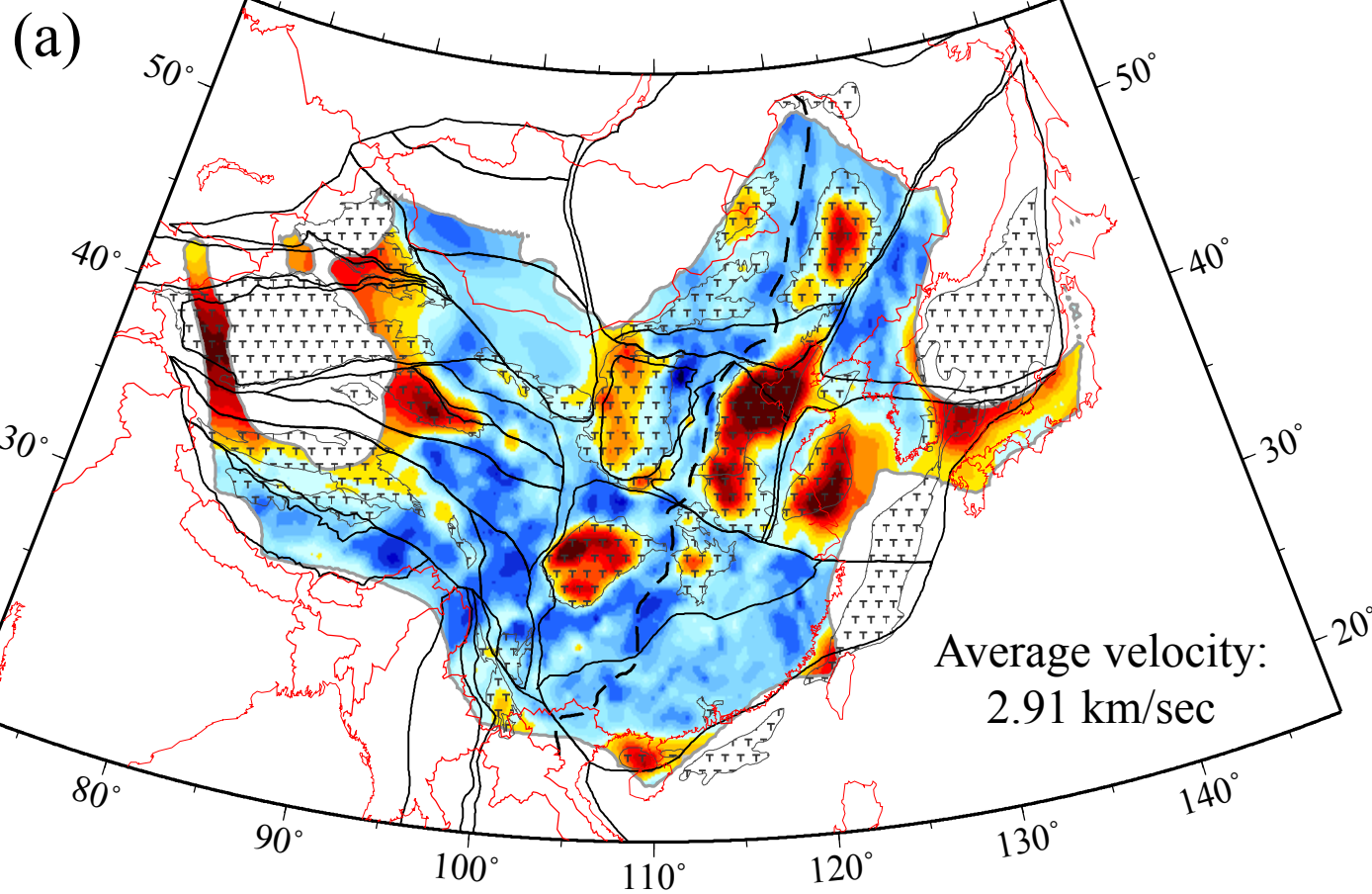
Figure 11

1  
2  
3  
4  
5  
6  
7  
8  
9  
10  
11  
12  
13  
14  
15  
16  
17  
18  
19  
20  
21  
22  
23  
24  
25  
26  
27  
28  
29  
30  
31  
32  
33  
34  
35  
36  
37  
38  
39  
40  
41  
42  
43  
44  
45  
46  
47  
48  
49  
50  
51  
52  
53  
54  
55  
56  
57  
58  
59  
60

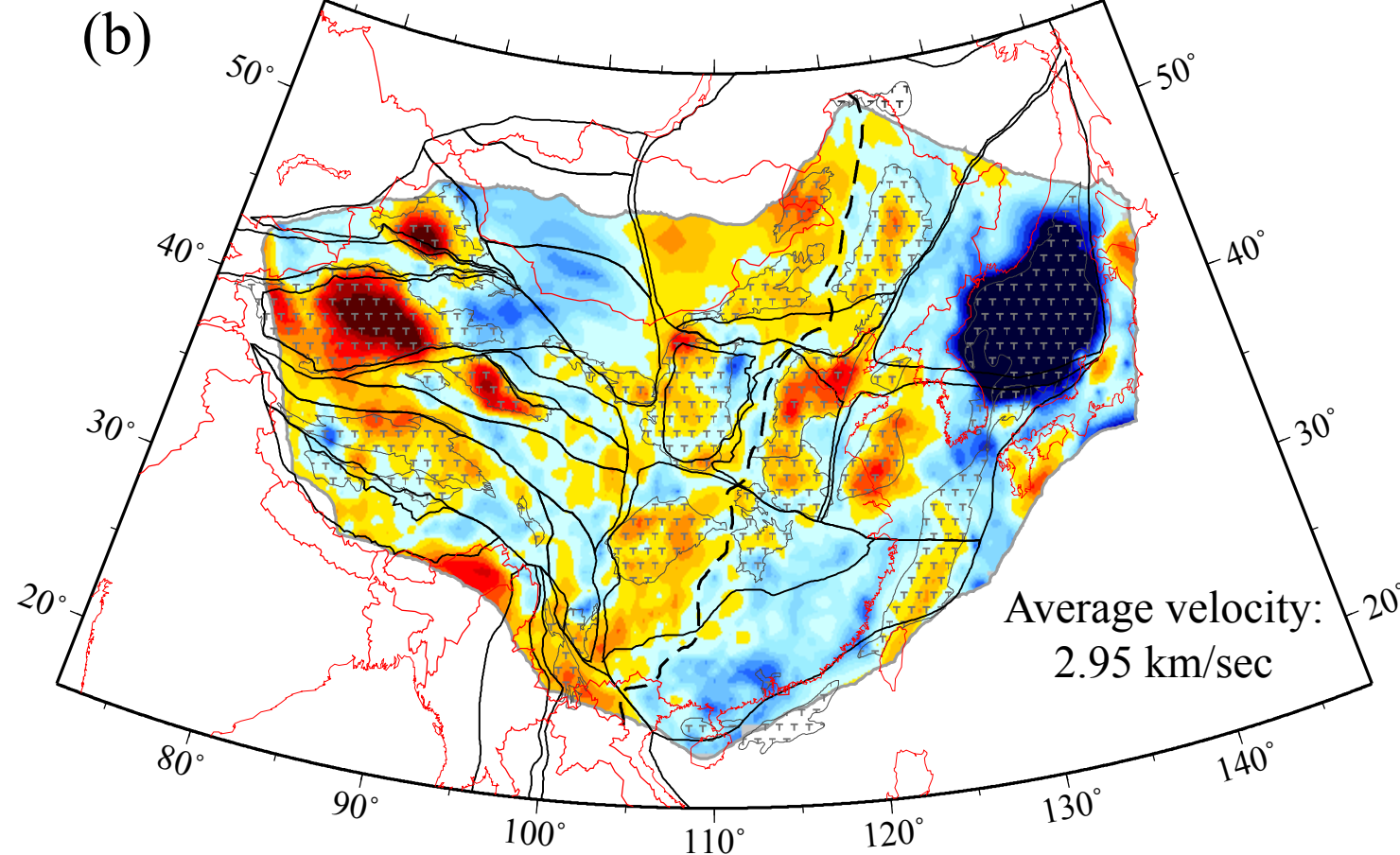


# Figure 12

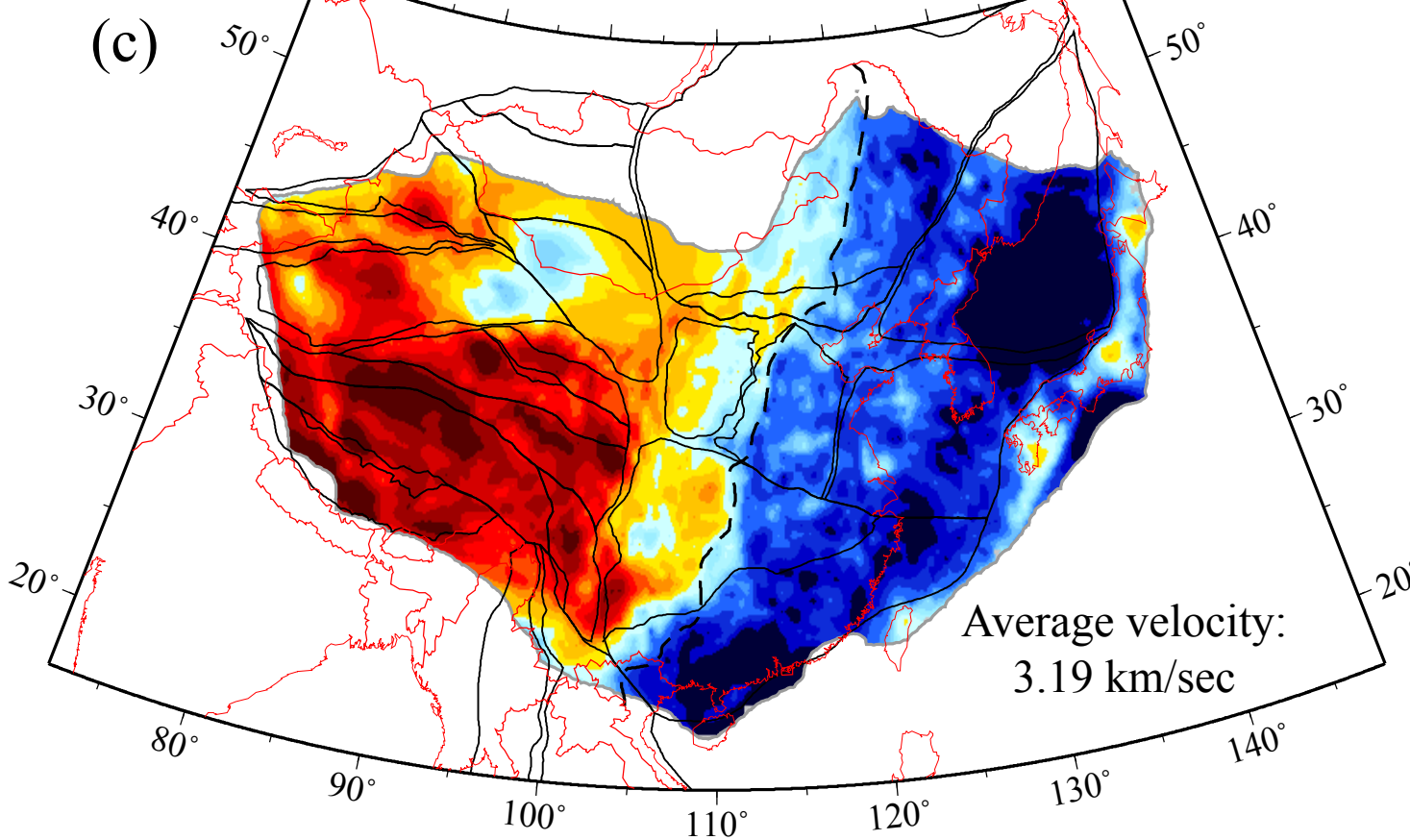
10 sec



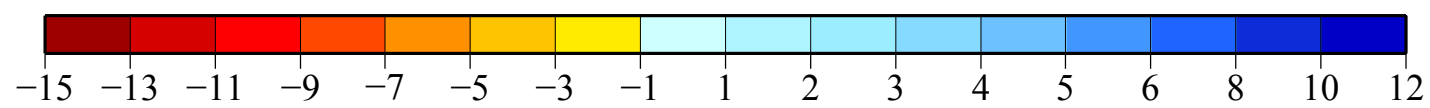
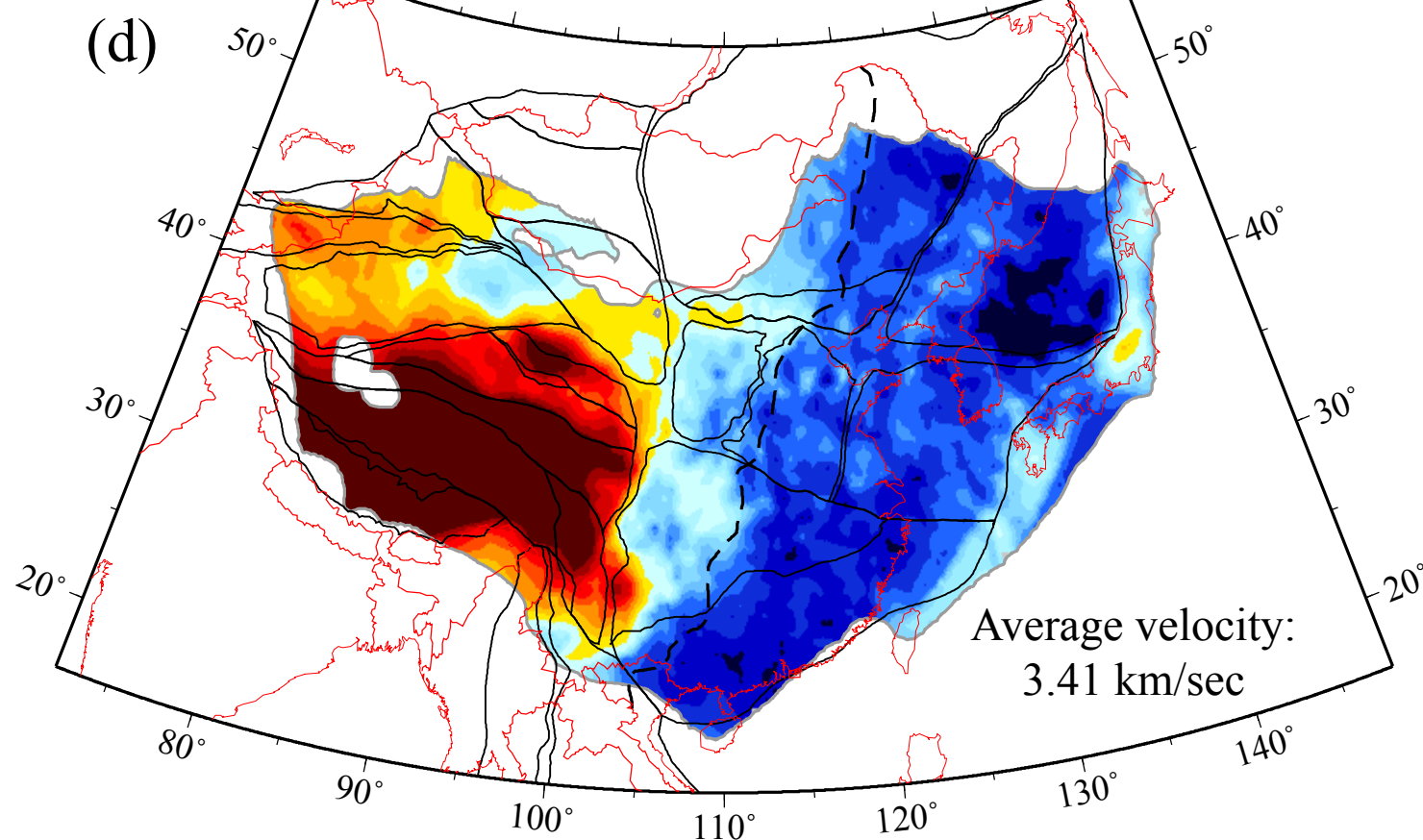
20 sec



30 sec

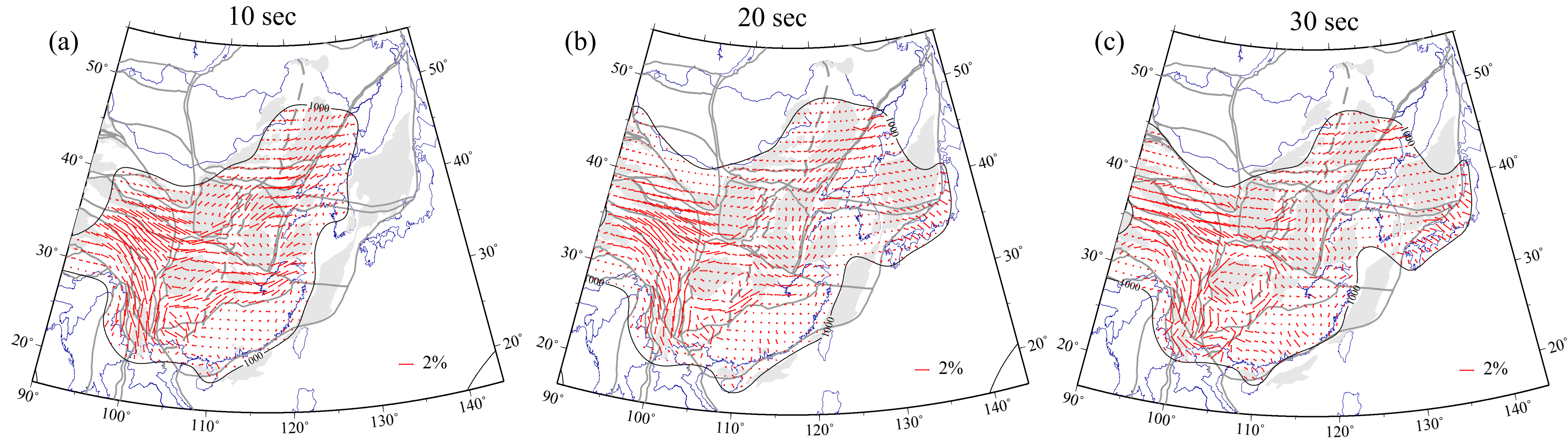


40 sec

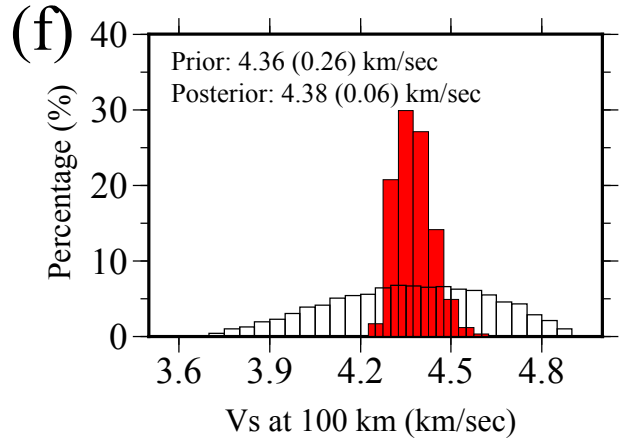
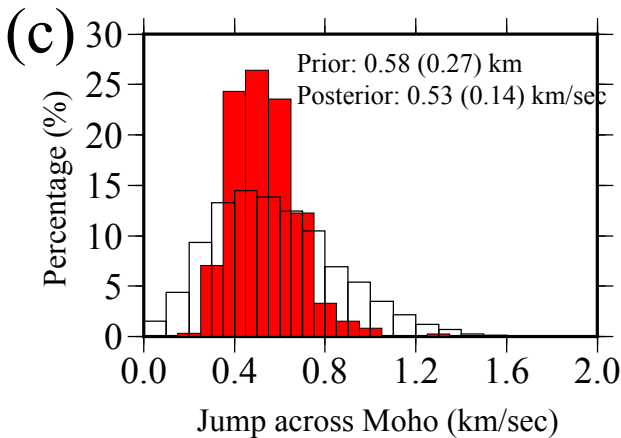
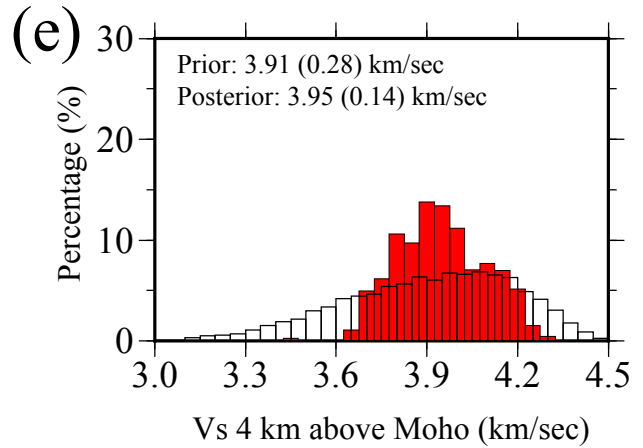
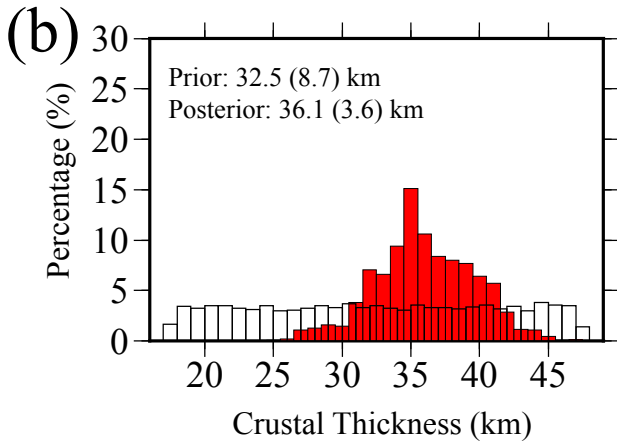
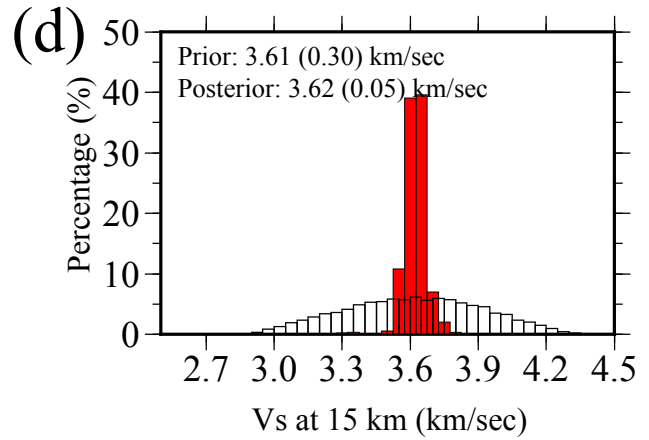
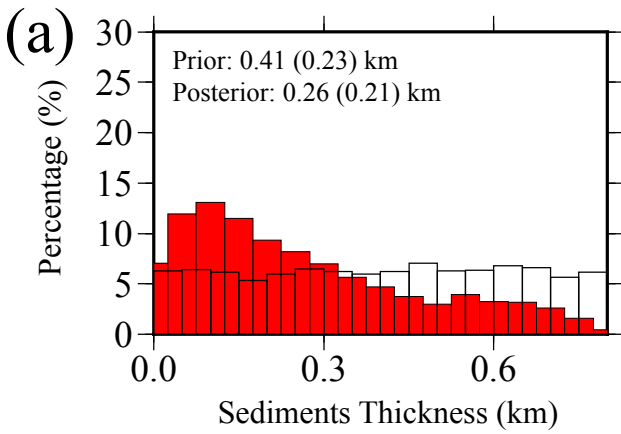


Perturbation relative to average velocity (%)

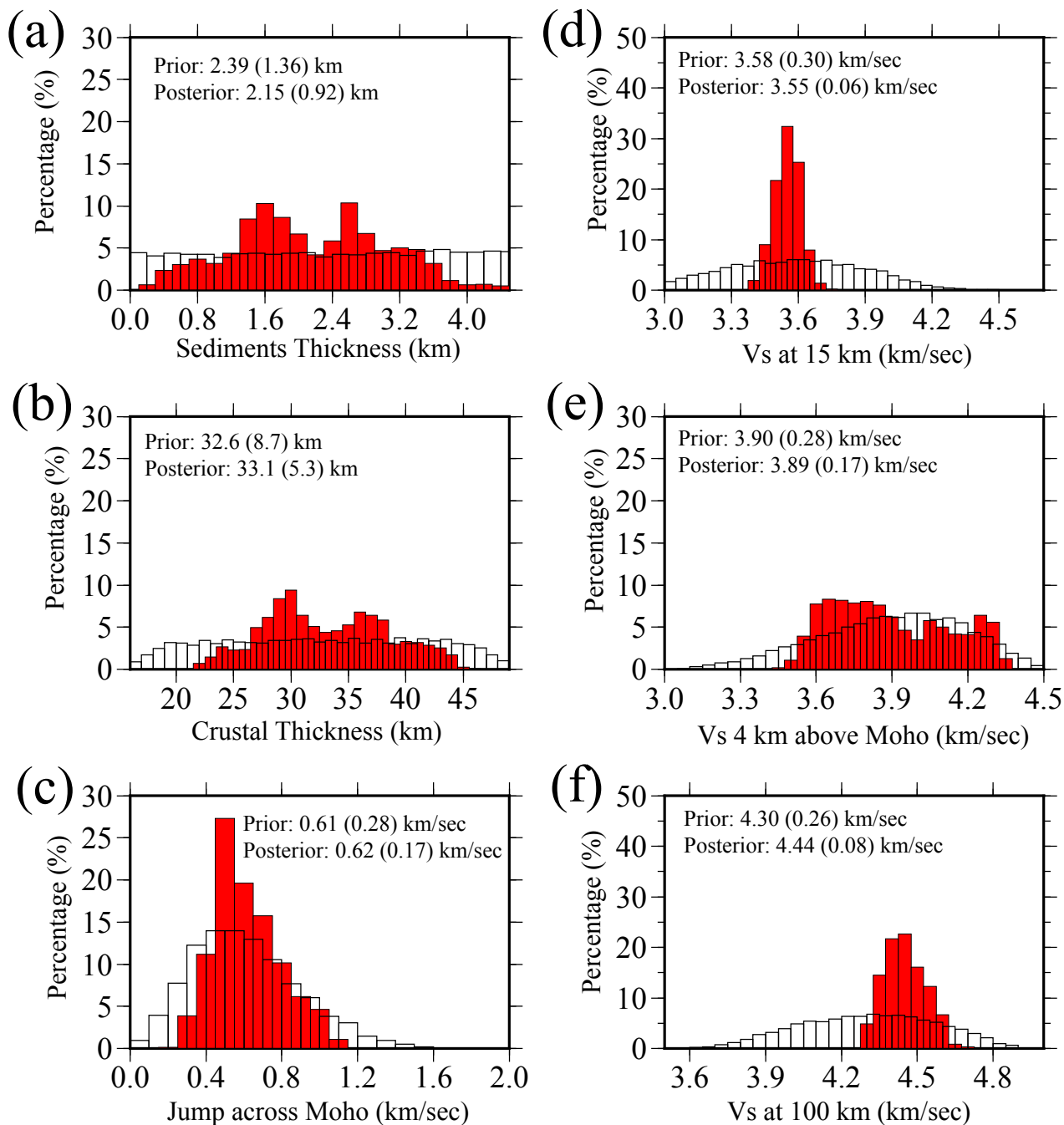
Figure 13



South China (E115, N29)

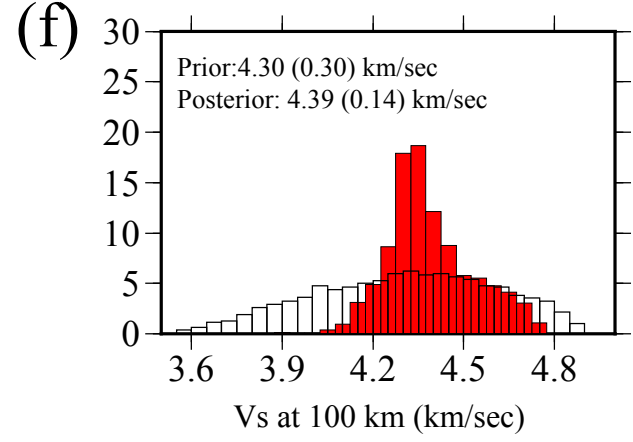
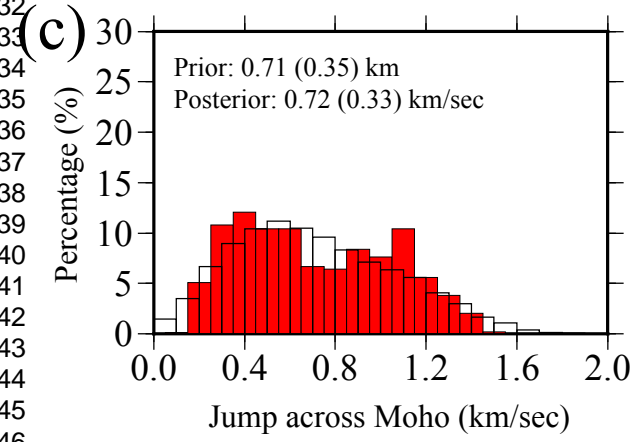
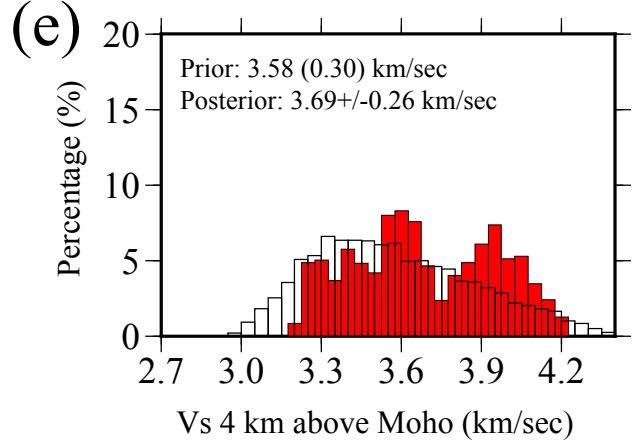
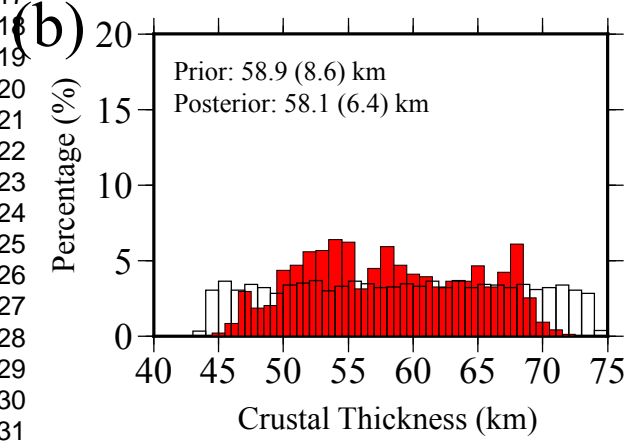
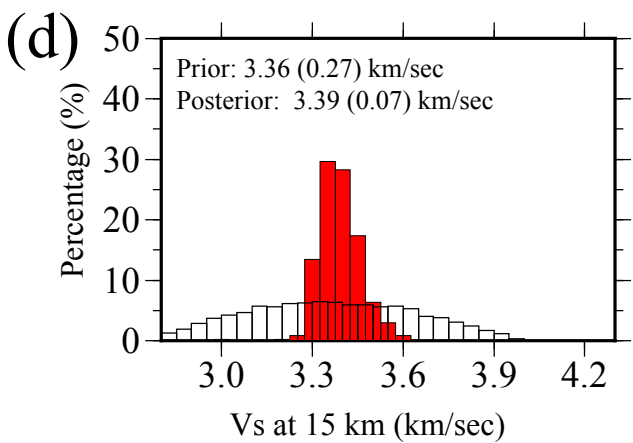
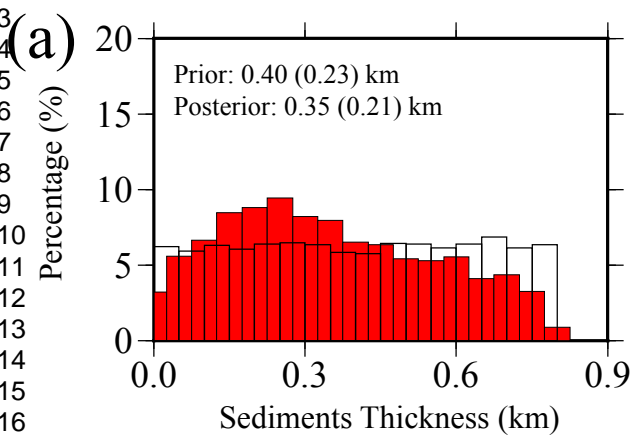


## NE China (E125, N47)



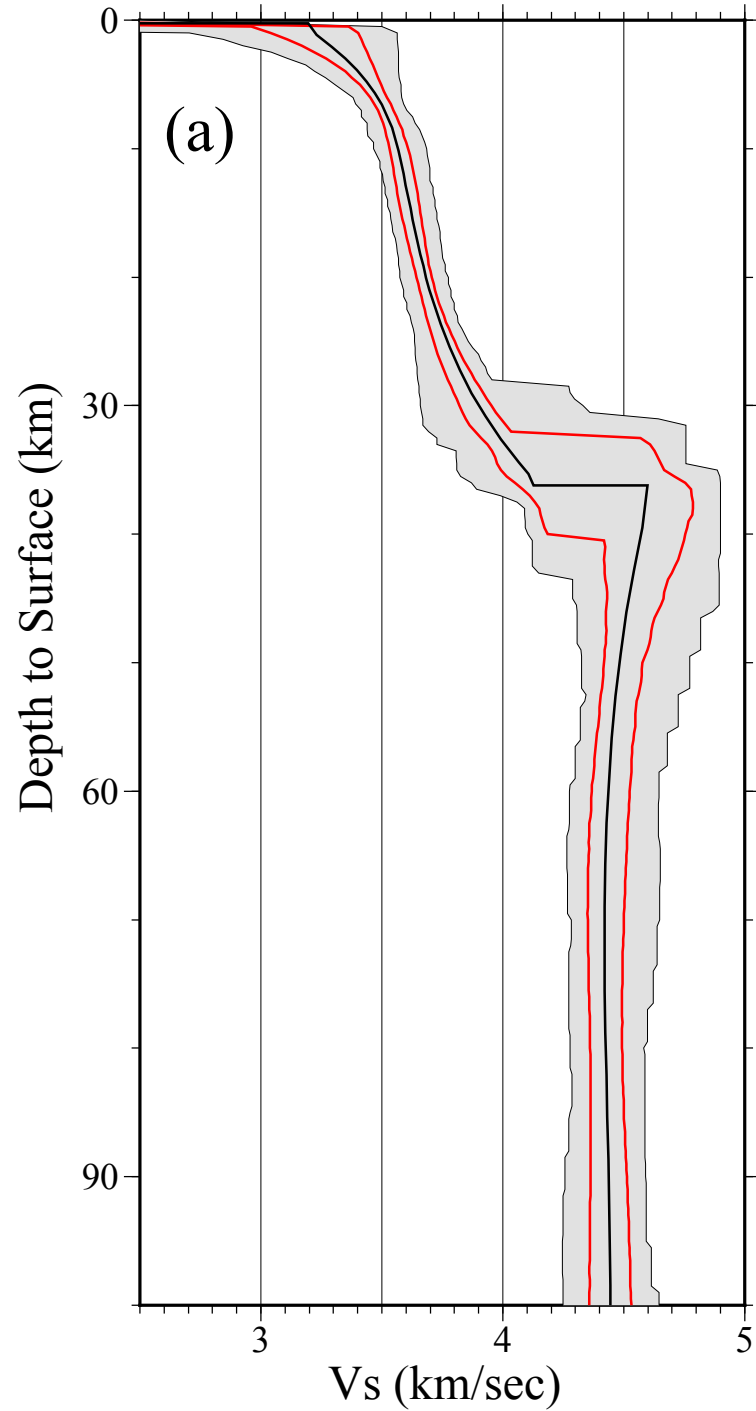
E. Tibet (E100, N34)

1  
2  
3  
4  
5  
6  
7  
8  
9  
10  
11  
12  
13  
14  
15  
16  
17  
18  
19  
20  
21  
22  
23  
24  
25  
26  
27  
28  
29  
30  
31  
32  
33  
34  
35  
36  
37  
38  
39  
40  
41  
42  
43  
44  
45  
46  
47

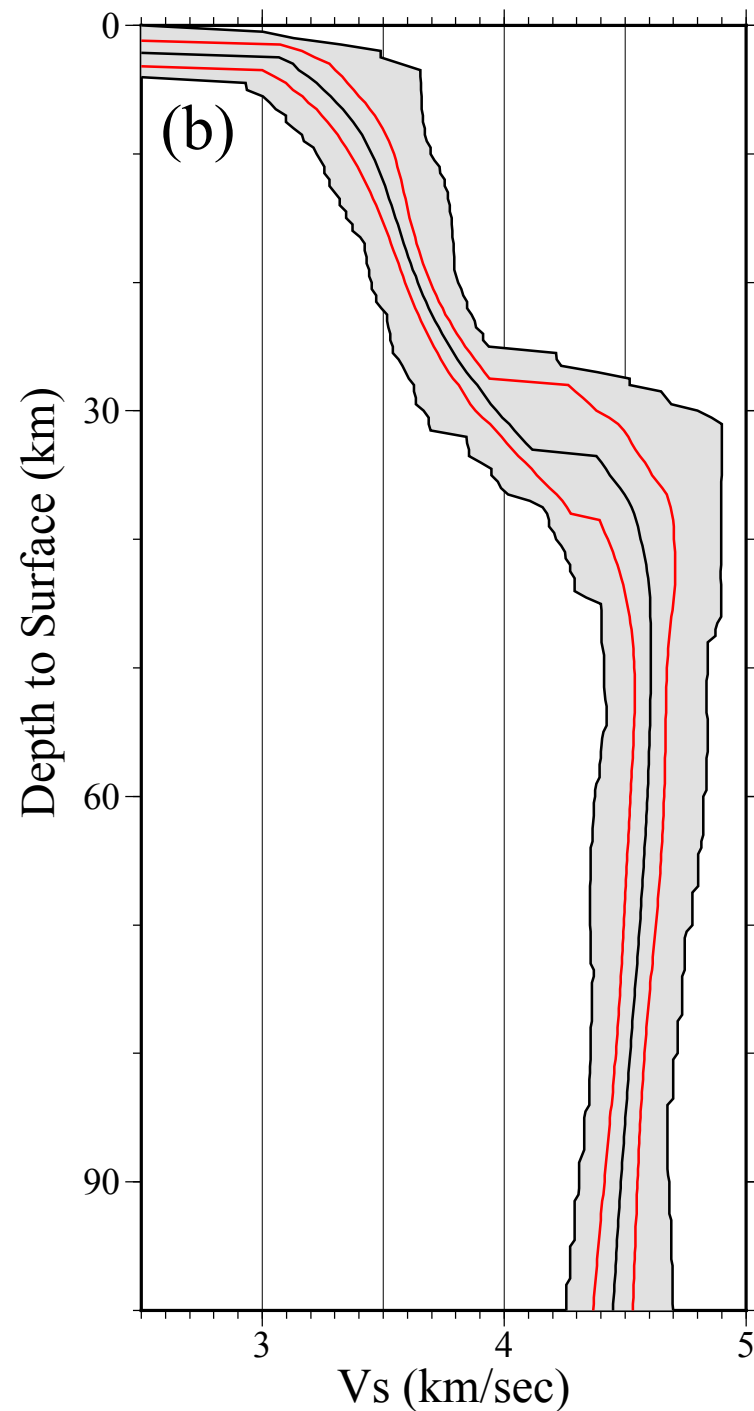


1  
2  
3  
4  
5  
6  
7  
8  
9  
10  
11  
12  
13  
14  
15  
16  
17  
18  
19  
20  
21  
22  
23  
24  
25  
26  
27  
28  
29  
30  
31  
32  
33  
34  
35  
36  
37  
38  
39  
40  
41  
42  
43  
44  
45  
46  
47  
48  
49  
50  
51  
52

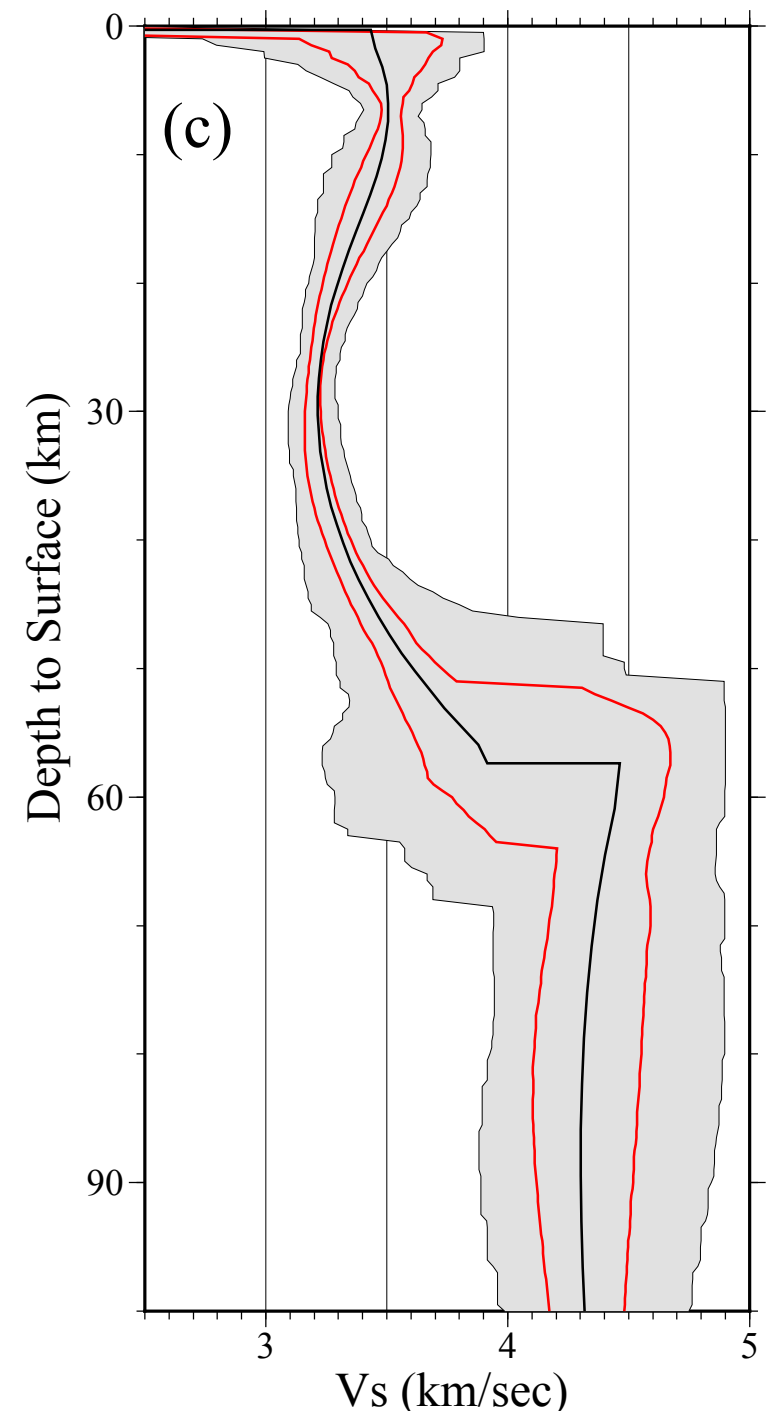
South China (E115, N29)



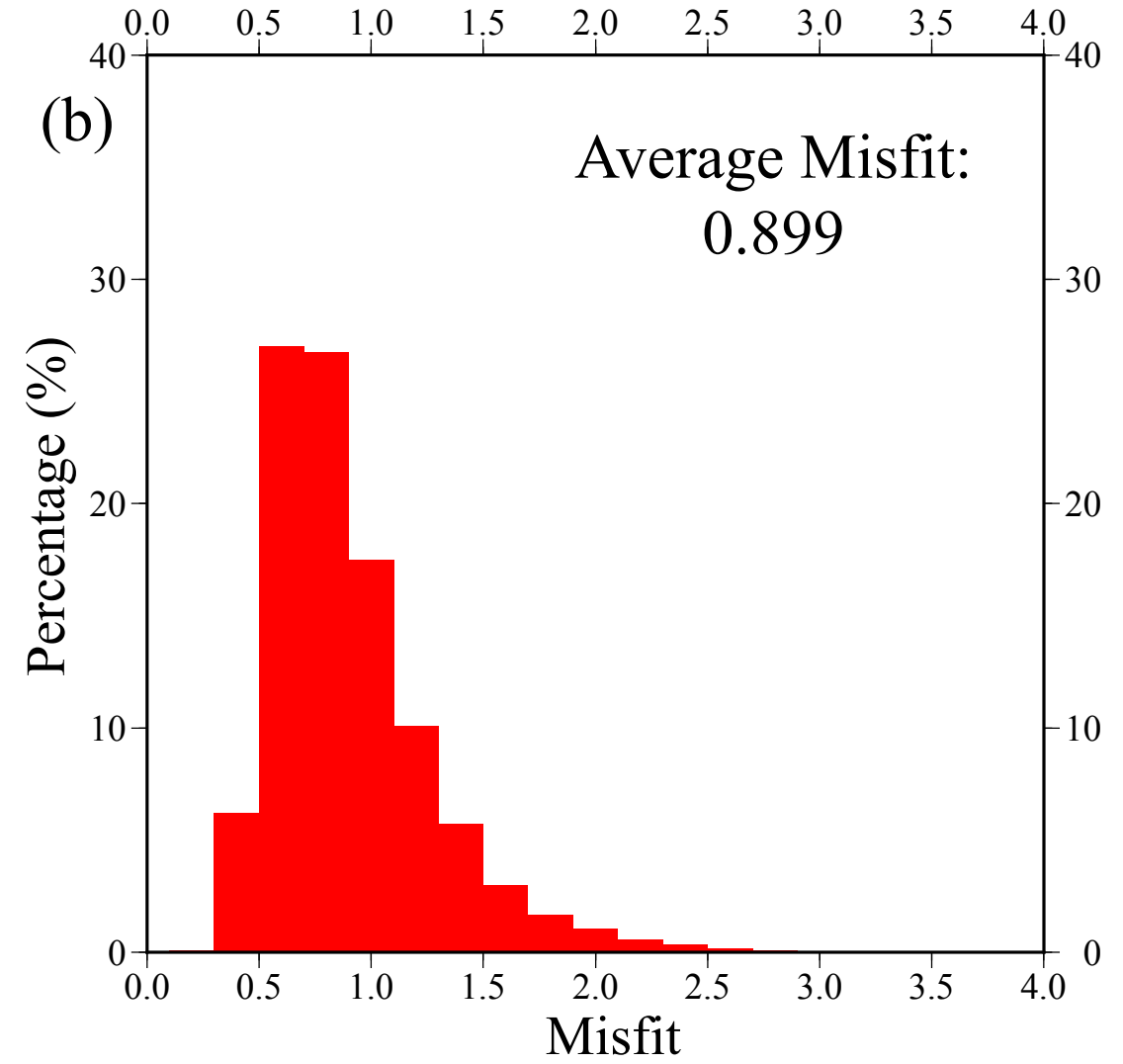
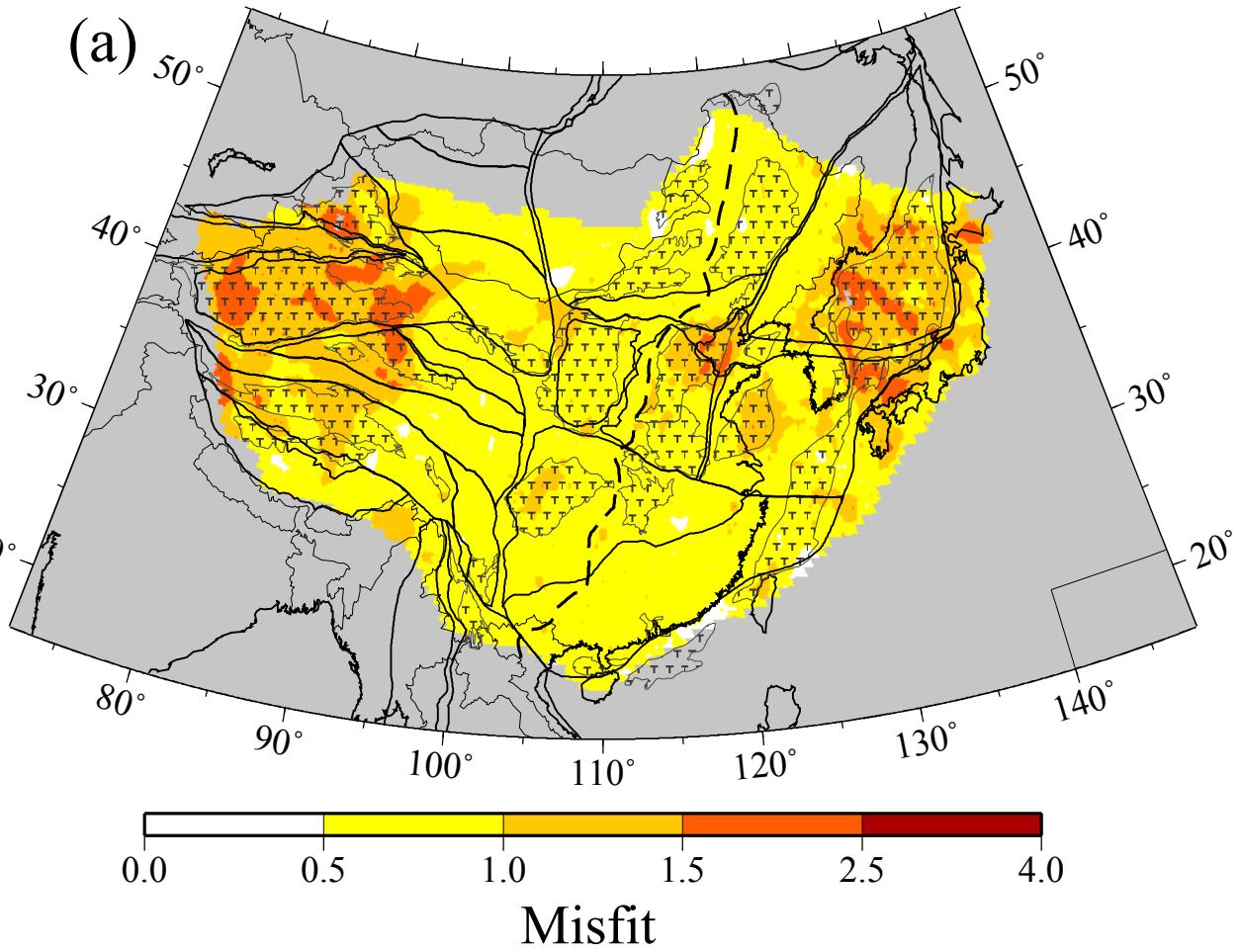
NE China (E125, N47)

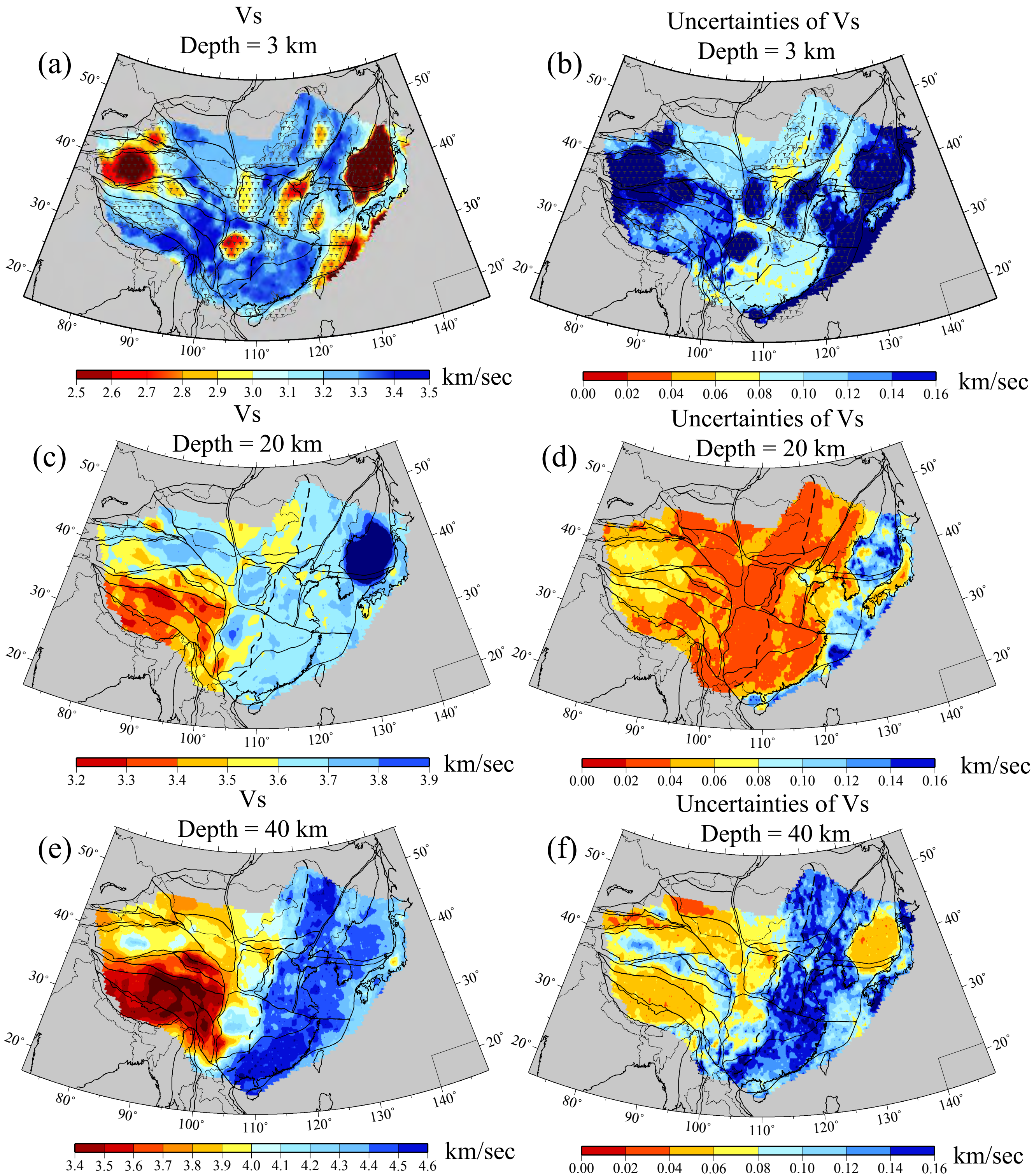


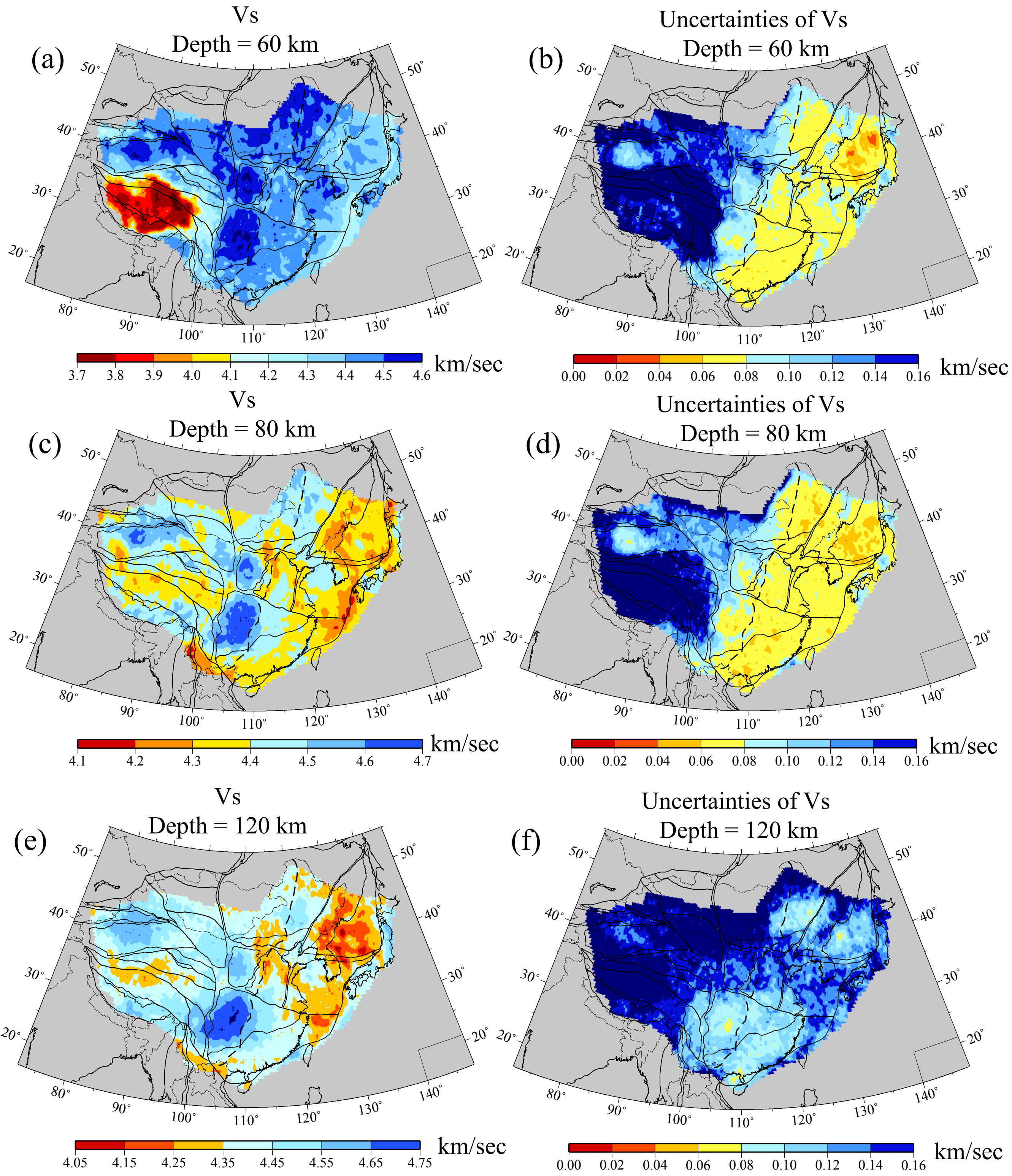
E. Tibet (E100, N34)

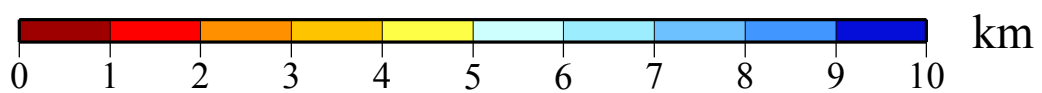
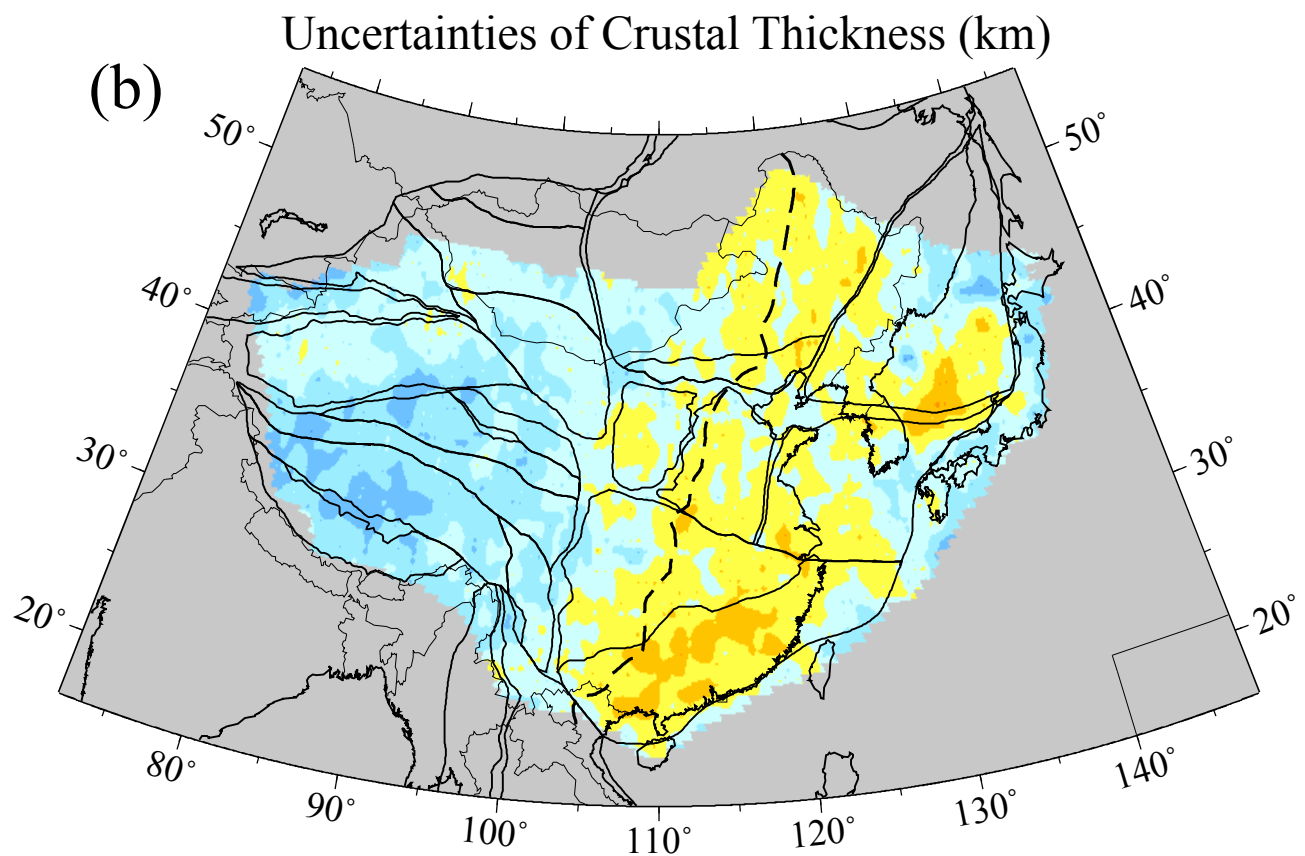
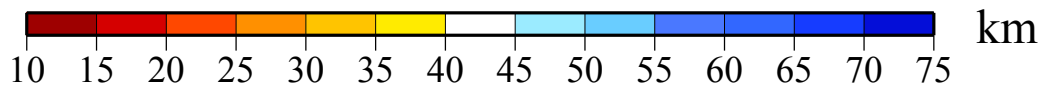
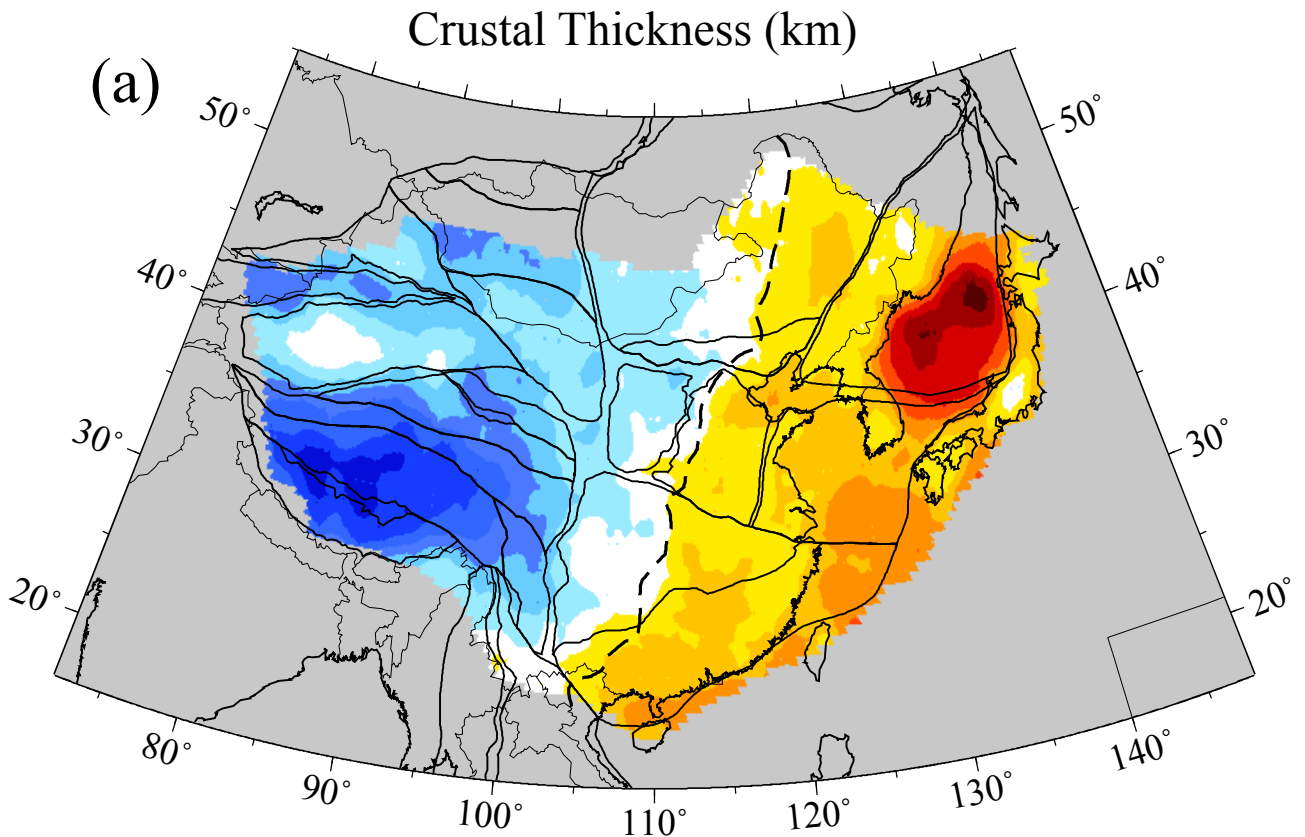


1  
2  
3  
4  
5  
6  
7  
8  
9  
10  
11  
12  
13  
14  
15  
16  
17  
18  
19  
20  
21  
22  
23  
24  
25  
26  
27  
28  
29  
30  
31  
32  
33  
34  
35









1  
2  
3  
4  
5  
6  
7  
8  
9  
10  
11  
12  
13  
14  
15  
16  
17  
18  
19  
20  
21  
22  
23  
24  
25  
26  
27  
28  
29  
30  
31  
32  
33  
34  
35  
36  
37  
38  
39  
40  
41  
42  
43  
44  
45  
46  
47  
48  
49  
50  
51  
52  
53  
54  
55  
56  
57  
58  
59  
60

1  
2  
3  
4  
5  
6  
7  
8  
9  
10  
11  
12  
13  
14  
15  
16  
17  
18  
19  
20  
21  
22  
23  
24  
25  
26  
27  
28  
29  
30  
31  
32  
33  
34  
35

### Vs at 80 km Depth

